Charles University in Prague
Faculty of Mathematics and Physics

PhD Thesis

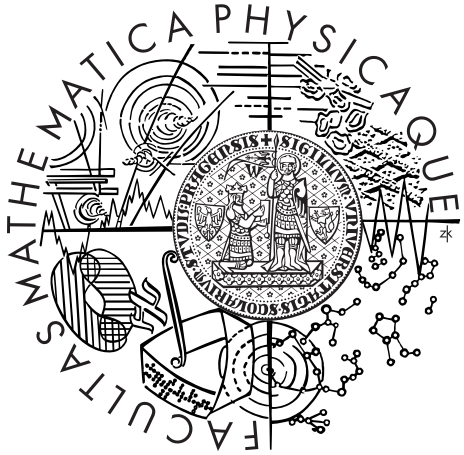

Mykhailo Barchuk

Diffuse x-ray scattering from GaN epitaxial layers

Department of Condensed Matter Physics

Supervisor: prof. RNDr. Václav Holý, CSc.
Study programme: F3 Physics of Condensed Matter and Materials Research
Department: Department of Condensed Matter Physics

Prague 2012

Acknowledgements.

I would like kindly acknowledge the following persons:

- my supervisor V. Holý for help and assistance during the whole period of my PhD study;
- my colleges from Charles University in Prague Z. Matěj, V. Valeš, L. Horák, M. Mixa, X. Marti,S. Daniš, R. Kužel for useful scientific discussions and support in software applications and x-ray measurements;
- my colleges from Institute for Synchrotron Radiation in Karlsruhe B. Miljević, B. Krause, S. Lazarev, S. Bauer, D. Grigoriev, A. Minkevich, T. Baumbach for successful international collaboration and scientific discussions;
- group of growers from University of Ulm J. Hertkorn, S. Schwaiger, K. Forghani and F. Scholz for providing samples to carry out our investigations and participation in scientific publications;
- my colleges from Johannes Kepler University in Linz D. Kriegner, J. Stangl and G. Bauer for measurements on x-ray machine equipped with rotating anode and scientific collaboration in a-plane GaN investigations;
- my colleges from Juri Fedkovich National University in Chernovtsy M. Borcha and I. Fodchuk for useful discussions;
- beamline scientists G. Buth (ANKA, Karlsruhe) and T. Cornelius (ESRF, Grenoble) for assistance in synchrotron measurements;
- my colleges from Institute of Physics AS CR in Prague O. Pacherová, J. Kub, and Z. Šourek for preliminary x-ray diffraction measurements of a-plane GaN films;
- another people who contributed to my PhD work but were not mentioned above.

Prohlašuji, že jsem tuto disertační práci vypracoval samostatně a výhradně s použitím citovaných pramenů, literatury a dalších odborných zdrojů.

Beru na vědomí, že se na moji práci vztahujou práva a povinnosti vyplývající ze zákona č. 121/2000 Sb., autorského zákona v platném znění, zejména skutečnost, že Univerzita Karlova v Praze má právo na uzavření licenční smlouvy o užití této práce jako školního díla podle č. 60 odst. 1 autorského zákona.

V Praze dne 28.8.2012 Podpis autora

Název práce: Difúzní rozptyl rentgenového záření na GaN epitaxních vrstvách

Autor: Mykhailo Barchuk

Katedra: Katedra fyziky kondenzovaných látek

Vedoucí disertační práce: prof. RNDr. Václav Holý, CSc.

Abstrakt: Reálná struktura heteroepitaxních vrstev GaN a AlGaN je studována pomocí difúzního rozptylu rtg záření. Nově vyvinutá metoda založená na Monte Carlo simulaci umožňuje určovat hustotu threading dislokací ve vrstvách c-GaN a vrstevných chyb ve vrstvách a-GaN. Hustoty defektů ze simulací Monte Carlo jsou srovnány s hodnotami získanými standardními metodami (transmisní elektronová mikroskopie, metalografie leptových důlků). Výhody a omezení našeho postupu jsou podrobně diskutovány; přesnost metody je stanovena jako ±15%. Ukázali jsme, že naše metoda je spolehlivý nástroj pro určení hustot threading dislokací a vrstevných chyb ve vrstvách GaN.

Klíčová slova: Gallium Nitrid (GaN), difrakce rtg záření, Monte Carlo simulace, threading dislokace, vrstevné chyby

Title: Diffuse x-ray scattering from GaN epitaxial layers

Author: Mykhailo Barchuk

Department: Department of Condensed Matter Research

Supervisor: prof. RNDr. Václav Holý, CSc.

Abstract: Real structure of heteroepitaxial GaN and AlGaN layers is studied by diffuse x-ray scattering. A new developed method based on Monte Carlo simulation enabling to determine densities of threading dislocations in c-plane GaN and stacking faults in a-plane GaN is presented. The results of Monte Carlo simulations are compared with ones obtained by use of another conventional techniques. The advantages and limitations of the new method are discussed in detail. The methods accuracy is estimated as about 15%. We have shown that our method is a reliable tool for threading dislocations and stacking faults densities determination.

Keywords: Gallium Nitride, x-ray diffraction, Monte Carlo simulation, threading dislocations, stacking faults

Contents

Introduction

Group III-V nitrides are the most promising materials for production of photonic devices as well as high-temperature/high-power electronic devices. The recent years they became extremely popular due their unique properties such as a direct bandgap varying from 0.7 eV for InN to 6.2 eV for AlN, piezoelectricity, high chemical and thermal stability etc [1]. In our investigations, we focus mainly on wurtzite Gallium Nitride (GaN) heteroepitaxial layers and additionally consider Aluminium Gallium Nitride (AlGaN) alloy. The main physical properties and applications of GaN are briefly discussed in Sec. 1.

GaN epitaxial layers have a lot of structural defects especially threading dislocations, which cross the entire GaN layer and come out perpendicularly on its surface. Depending on the dislocation densities GaN can be used for various applications. Exceeding the maximum acceptable value of dislocation densities (about 10^9 cm^{-2}) the grown material becomes unsuitable for particular industrial uses. Stacking faults are another type of defects in GaN that occur mostly in films with non-polar orientation. The general description of structural defects in crystalline material as well as the characterization of the most typical defects for GaN layers are given in Sec. 2.

In our work, we study several series of samples of GaN and AlGaN with different crystallographical orientations grown on foreign substrates by our partners from University of Ulm. The growing technique used to produce these samples is known as metal-organic vapour phase epitaxy. This method consists in epitaxial deposition from gases on the hot substrate surface. In Sec. 3 one can find the review of various growth techniques and specification of the samples with different orientations under study. The connection between the growth process and desired structure on a nanoscale is often non-obvious. One of the most important criterion to estimate the quality of the certain growth technique is to determine the density of defects in the layers. Therefore a reliable method for the determination of the dislocation and stacking faults density is of a crucial importance.

In order to solve the problem mentioned above, a large number of methods based on different techniques has been already developed. They can be divided on direct and indirect depending on data, which we analyse to obtain final information about the dislocation densities. The detailed overview of the most widely used methods, their advantages and disadvantages can be found in Sec. 5. One of the most common methods to determine the density of threading dislocations in thin films is to use non-destructive x-ray technique (see Sec. 4).

The analysis of diffuse x-ray scattering from imperfect crystals is usually based on the assumption that the diffracted wave is averaged over the statistical ensemble of all defect configurations. In this case the calculation can be done manually by means of well-known Krivoglaz theory [2]. However very often we deal with the objects, which do not obey the averaging principles and require a specific approach for their description. Thin films of GaN or AlGaN are good examples of such kind of materials. Therefore we applied a numerical Monte Carlo method within the kinematical approximation and the far-field limit in the scattering theory. The result of our simulation is a set of reciprocal-space maps calculated in coplanar and grazing-incidence diffractions. The results of

calculations are compared with experimental data obtained at laboratory x-ray diffractometer as well as by use of synchrotron radiation sources.

Our Monte Carlo technique enables to determine the density of edge and screw threading dislocations in polar GaN layers and the density of basal stacking faults in case of non-polar films. We succeeded to achieve high enough accuracy in our simulation (the error is estimated less than 15 %) comparable to advanced method developed by V. Kaganer et al. [3] and results of transmission electron microscopy. A detailed description of our experimental technique and theoretical approach can be found in Sec. 6-9. The resulting densities are compared to ones obtained with another methods and the advantages and weaknesses of uor approach are discussed in 10

Our theory is expounded to characterization of AlGaN bilayer system. We perform simulations taking into account two layers of AlGaN material with different thicknesses and densities of threading dislocations and obtain independently the density of screw dislocations in both layers. We demonstrate a good agreement between our simulations and experimental data in case of more complicated heteroepitaxial N-based compounds.

1. Description of Gallium Nitride Material

1.1 Basic parameters of GaN

Gallium nitride is nowadays the most important semiconductor material since Silicon (Si). Its wide band gap of 3.4 eV along with the latest advancements in GaN substrate manufacturing technology makes it useful for a variety of applications described in detail in Sec. 1.2. GaN based devices and products offer a wide variety of compelling advantages and superior performance characteristics over the incumbent options [1, 4, 5].

Gallium nitride is a very hard, mechanically stable material with high thermal capacity. In its pure form it is able to resist cracking and can be stored as a thin film on sapphire or silicon carbide wafers, despite the mismatch in their lattice constants. GaN can be alloyed with silicon or oxygen forming the N-type and magnesium forming the P-type conductivity. However, the atoms of silicon and magnesium alter the path of GaN crystal growth giving rise the static tension, which makes them brittle. As a rule, compounds of GaN have large number of crystallographic defects.

A favourable combination of many chemical and physical properties opens up broad prospects for gallium nitride application in various fields of electronics. High chemical, thermal and radiation resistance of GaN makes it suitable for the manufacture of devices operating in adverse conditions. Good thermal conductivity removes many problems of cooling of the working area, and a combination of high saturation velocity of electrons and a large breakdown field makes it suitable for the construction of high-power, high-frequency and high-temperature transistors. The interest in gallium nitride has increased significantly because of the success in obtaining high quality epitaxial layers and their implementation on the basis of efficient light-emitting diodes for the blue and blue-green spectral region, as well as the blue laser diode operating in continuous mode at a temperature of 20 ^{o}C.

Gallium nitride can exist in either in wurtzite or in zinc-blende crystallographic modifications. The primitive GaN unit cell contains 4 atoms, in the case of the wurtzite structure (space group $P6_3mc$), and 2 atoms, in the case of the zinc-blende structure (space group $F\bar{4}3m$). For wurzite GaN the unit cell parameters in lateral and vertical directions at room temperature are $a = 0.3186$ nm and $c = 5.178$ nm respectively. For zinc-blende GaN $a = 0.452$ nm. In our work, we focus on wurzite GaN and its compounds.

There are several equivalent ways to define the unit cell. For the purposes of our investigation we will define the structures as follows. The shape of the wurtzite cell is a vertically oriented prism, with the base defined by the primitive lattice vectors $\boldsymbol{a}$ and $\boldsymbol{b}$, which are of equal lengths and are separated by an angle of 60^o. The height of the cell is defined by the vector $\boldsymbol{c}$, which is oriented vertically at 90 ^{o} to both $\boldsymbol{a}$ and $\boldsymbol{b}$. In the "ideal" wurtzite structure $\boldsymbol{a} = \boldsymbol{b}$, and $\boldsymbol{c}$ is related

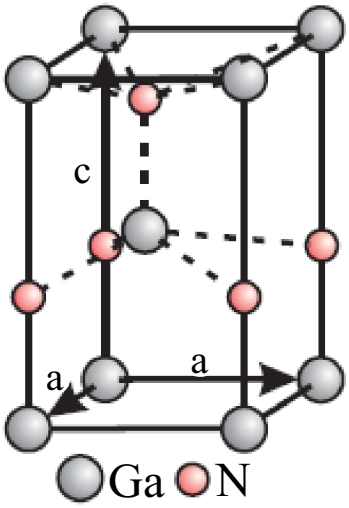

Figure 1.1: The unit cell of wurtzite GaN.

to $\boldsymbol{a}$ as

$$\boldsymbol{c} = 2\sqrt{\frac{2}{3}}\boldsymbol{a}. \tag{1.1}$$

To specify the positions of atoms within the cell the fractional coordinates are usually used for convenience. If a point $\boldsymbol{r}$ has Cartesian coordinates (x, y, z), then its fractional coordinates $[x', y', z']$ are defined as

$$\boldsymbol{r} = x'a + y'b + z'c \tag{1.2}$$

The Ga atoms are positioned that one is at the origin $[0, 0, 0]$ and another is at $[\frac{1}{3}, \frac{1}{3}, \frac{1}{2}]$. The N atoms are placed directly above the Ga atoms, namely at $[0, 0, \frac{3}{8}]$ and $[\frac{1}{3}, \frac{1}{3}, \frac{7}{8}]$. A graphical representation of the wurtzite cell is shown in Figure 1.1.

The shape of the primitive two-atom zinc blende cell is an equal-sided parallelepiped that can be most easily visualised by a larger 8-atom cubic cell. This cubic cell has Ga-atoms at the origin and in the centre of each of the three faces that touch the origin. Each N-atom is shifted with respect to Ga-atom at a displacement of $[\frac{1}{4}, \frac{1}{4}, \frac{1}{4}]$. The lattice vectors defining the primitive cell are the three vectors going from the origin to the centre of the three faces where the Ga-atoms are located. These vectors are of equal length and are separated from each other by angles of 60^o. The three Ga-atoms on the faces of the cube are not in the primitive cell as they are simply the periodic repetitions of the atom at the origin. . The primitive cell thus contains a Ga-atom at $[0, 0, 0]$ and N-atom at $[\frac{1}{4}, \frac{1}{4}, \frac{1}{4}]$.

1.2 Technical applications of GaN

1.2.1 Light emitting diodes

The III-V nitride material system, which includes AlN, GaN, InN, and their alloys, has been extensively investigated due to their applications in light-emitting

diodes (LED), laser diodes, and photodetectors [6]. LEDs are used in various lighting applications, including flash lights, automotive lighting, traffic signals, TVs and very large displays, and they are now widely commercially available.

The band gap of the InGaN material system now ranges from the infrared to the ultraviolet region. In addition to the wide band gap range, the nitrides also demonstrate favourable photovoltaic properties such as low effective mass of carriers, high mobilities, high peak and saturation velocities, high absorption coefficients, and radiation tolerance. The III-V nitride technology has demonstrated the ability to grow high-quality crystalline structures and fabricate optoelectronic devices, which confirms its potential in high-efficiency photovoltaic. While the commercially available violet and blue LEDs use high-band gap InGaN as the active material, the relevant material for photovoltaics is the lower band gap InGaN employed in recently emerging blue-green LEDs. However, due to the present technological challenges in the epitaxy of low band gap optoelectronic quality InGaN and additional requirements posed during solar cell fabrication, III-V nitride photovoltaics still remain a promising but a largely unexplored application.

1.2.2 Solar cells

The direct and wide band gap range makes the InGaN material system useful for photovoltaic applications due to the possibility of fabricating not only high-efficiency multijunction solar cells but also third-generation devices such as intermediate-band solar cells based solely on the nitride material system. The schematic of a typically fabricated solar cell is the following. Undoped lower band gap test InGaN is sandwiched between the top p- and the supporting n-type GaN junctions to ensure fabrication due to the ease of growth and maturity of fabrication technology for GaN compared to InGaN [7].

Initial spectrometry of the grown GaN and high-band gap InGaN samples concur with literature values measuring absorption coefficients of the order of 10^5 cm^{-1} at the band edge at 3.2 eV. These high values indicate that more than 99% of the incident light with energy greater than the band gap is absorbed within the first 500 nm of the material, limiting the thickness requirement of the solar cell to this value. The thickness of the InGaN region is typically limited to 200 nm.

The primary challenge at the epitaxial growth III-V nitride photovoltaics is the reduction of phase separation, since the lower band gap phase-separated material enhances recombination decreasing the photogenerated current. The quantum efficiency can be further enhanced by optimizing grid contacts for low resistance and be brought close to unity as confirmed by simulations. The efficiency of the GaN/InGaN solar cells can generally be increased by lowering their band gaps and enhancing absorption for practical applications. However, phenomenon such as polarization, which tends to substantially influence the performance of III-V nitride devices, and advance contacting schemes such as short-period superlattices are currently investigated for the next step of enhancement.

1.2.3 Power amplifiers

Challenged with the demand to engineer higher-performing, more-efficient and lower-cost systems in a shorter time-to-market, many designers have focused on power amplifiers. Power amplifiers are a primary performance and cost factor in designing next-generation communication systems, and an advanced transistor can enable designers to meet their design goals.

Improving the efficiency of a power amplifier can significantly enhance a design. In amplifying high peak- to average-power radio frequency signals, as much as 90% of the power consumed is lost to heat. This heat results in high thermal management demands, increasing heat sink costs (capital expenses) as well as node size and air-conditioning costs (operating expenses). This double penalty for power-transistor efficiency translates into a double benefit when performance is improved.

With the trend toward increasing data consumption among mobile terminal subscribers has come the need for increased channel and carrier bandwidth. As engineers are asked to provide wider-bandwidth power amplifiers up to 200 MHz, traditional technologies such as Si laterally diffused metal oxide semiconductors (LDMOS) suffer significant efficiency penalties. The adoption of GaN on Si allows the use of traditional packaging technologies common to Si LDMOS, eliminating concerns associated with new package engineering.

The relatively high input and output impedances of gallium nitride devices allow these bandwidths to be achieved while maintaining higher efficiency than traditional technologies. This allows high-efficiency architectures to provide substantial improvements while increasing amplifier bandwidth.

The primary problem with foreign sapphire or SiC substrates for GaN has been achieving low enough defect density on large enough wafers to make large-area transistors cost-effective. As a result, commercial success for GaN has been largely limited to LED applications, which have a high tolerance for these defects. More recently, GaN has been successfully grown on traditional Si wafer substrates using well understood processing techniques and equipment for III-V semiconductors. With high-quality Si wafers being commonly available at very low costs, defects and substrate costs are no longer an issue. Furthermore the ability to scale to high-volume manufacturing is straightforward.

Until recently, market acceptance of GaN technology has also been hindered by the lack of comprehensive reliability data. Process and product qualification documents are now published that show reliability meeting or exceeding industry standards.

2. Structural Defects in Crystals

2.1 General description of crystallographic defects

Crystalline solids are characterized by periodic crystal structure. In ideal crystals, their atoms, ions or molecules (later only atoms) form the periodic crystal lattice with the fixed unit cell parameters. However, real crystals contain imperfections called crystallographic defects. They locally disturb the regular arrangement of atoms that breaks the perfect translational symmetry in the crystal. These imperfections can be classified according to their dimensional extension as point, line, planar or surface and bulk or volume defects. The presence of defects strongly affects the properties of crystalline solids.

2.1.1 Line defects

Linear or one-dimensional defects are defects in crystals, which sizes in one direction are much larger than the lattice parameter and in the other two are comparable to it. Dislocations are linear defects around which some of the atoms of the crystal lattice are misaligned. They represent the border areas of unfinished shift in the crystal. Dislocations occur during crystal growth, with its plastic deformation, and in many other cases. The dislocation theory was originally developed by Vito Volterra in 1905 but the term 'dislocation' was introduced later by Professor Sir Frederick Charles Frank [8, 9].

In materials science, dislocations are crystallographic defects or irregularities, within a crystal structure. Their presence, distribution and behaviour of external influences determine the most important mechanical properties of the material. A detailed study of linear lattice defects is coupled with their strong influence on the strength and plasticity of practically all construction of crystalline materials. Theory of strength of crystals, which do not recognize this type of defects, could not even approximately explain the observed mechanical properties of both mono- and polycrystalline materials. The quantitative description of the dislocation is given by Burgers vector. Its atomistic definition is derived from the Burgers loop in the deformed and ideal crystal lattices. This is an arbitrary closed clockwise circulation around a dislocation as a vector chain of the basis vectors of the lattice. The second Burgers loop, plotted in the similar crystal lattice without any dislocation, is compared with the first loop. The difference between the starting and ending points in the intact crystal is called the Burgers vector $\boldsymbol{b}$ that describes the magnitude and direction of lattice distortion. A graphical determination of the Burgers vector of the edge dislocation is presented in Fig. 2.1.

Except the Burgers vector, every dislocation is characterized by the dislocation line and the angle ϕ between the dislocation line and the Burgers vector. When $\phi = 0$ this type of defect is called a screw dislocation, with $\phi = 90^o$ we speak about an edge dislocation. A simple schematic diagram of an edge and a screw dislocation is illustrated in Fig. 2.2. In case of other ϕ values the dislocation is called mixed and it can be decomposed into pure screw and pure edge components. The dislocations found in real materials typically are mixed, meaning that they

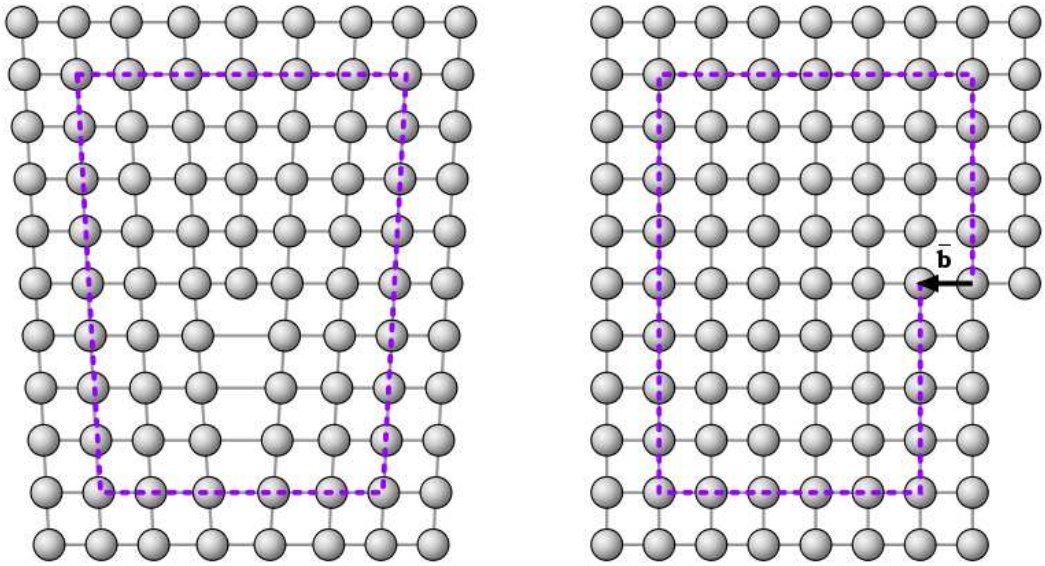

Figure 2.1: The definition of the Burgers vector of edge dislocation. The Burgers loop is depicted with light violet dashed lines. The picture is taken from Wikipedia.

have characteristics of both [10].

An edge dislocation is a defect where an extra half-plane of atoms is introduced inside the crystal, distorting nearby planes of atoms. When enough force is applied from one side of the crystal structure, this extra plane passes through planes of atoms breaking and joining bonds with them until it reaches the grain boundary. An edge dislocation can be visualized as being caused by the termination of a plane of atoms in the middle of a crystal. In such a case, the surrounding planes are not straight, but instead bend around the edge of the terminating plane so that the crystal structure is perfectly ordered on either side.

Edge dislocations are conventionally divided into positive and negative. Positive dislocations correspond to the case when the top is an extra atomic half-plane.

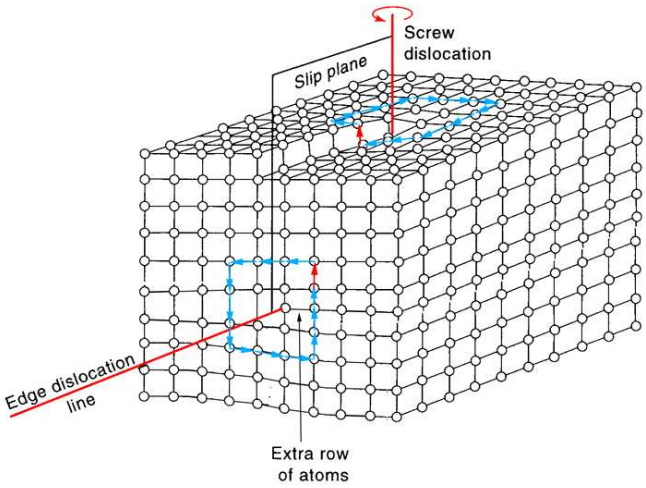

Figure 2.2: The scheme of edge and screw dislcations with their dislocation lines.

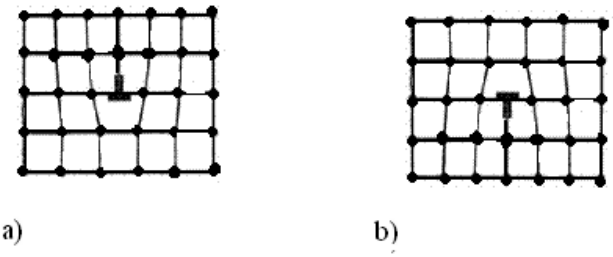

Figure 2.3: The schematic representations of a) positive-edge and b) negative-egde dislocation.

The atoms above the dislocation line are squeezed together due to the extra half-plane that results in a compressive stress field. Below the dislocation line the extra plane imposes a tensile stress on the lattice. It is easy to see that these two dislocations are distinguished only by turning by 180^o as it is shown in Fig 2.3. The forces of the elastic interaction between dislocations depend on the sign of the dislocation. Depending on circumstances they may cancel each other out, attract, repel or become entangled. When two dislocations with the same sign on the same slip plane meet the interaction of their compressive stress fields will cause them to repel each other. If they have opposite signs however their tensile and compressive fields will attract. When they meet the two half-planes of atoms will join to become one whole plane and the dislocations will cancel each other out.

A screw dislocation is much harder to be visualized. Let us consider a cut of a crystal along a plane and a slip of one half across the other by a lattice vector, when the halves are fitted back together without leaving a defect. If the cut only goes part way through the crystal, and then slipped, the boundary of the cut is a screw dislocation. It comprises a structure in which a helical path is traced around the linear defect (dislocation line) by the atomic planes in the crystal lattice as it is depicted in Fig. 2.2. Screw dislocations can be right-handed and left-handed, the direction of rotation plays the same role as the sign of the edge dislocation. Two right- or two left-handed screw dislocations repel each other, right and left - are compensated. Thus, the screw and edge dislocation is the border between the shifted and unmoved parts of the crystal, whereas the edge dislocation is perpendicular to the shear vector, and the screw one is parallel to this vector.

The dislocation in crystalline material can start to move under an applied stress. There are two types of dislocation movements:

- Glide or conservative motion, when the dislocation moves in the plane which contains both its line and its Burgers vector. A dislocation able to move in this way is termed glissile, one which can not is termed sessile.

- Dislocation motion by climb occurs when the dislocation moves out of the glide plane, and thus normal to the Burgers vector.

Glide of many dislocations results in slip which is the most common manifestation of plastic deformation in crystalline solids. Due to the slip mechanism the plastic deformation of real crystalline materials can occur at a much lower yield stress than for a theoretical perfect crystal. The dislocation line can move through the crystal in the direction of the applied stress by breaking only one line of bonds at

a time. This requires far less energy than breaking lots of bonds simultaneously, so the material can be deformed under a much lower applied stress [11].

The energy of deformation of crystal lattice is associated with the dislocation. This energy can be calculated due to the continuum approximation for the dislocation away from the sites of the crystal and the model of interacting atoms at small distances from the dislocation.

The theory of elasticity can get approximate formulas for the line energy of a dislocation typically represented as an energy per unit length [12]. The total energy of a dislocation comes from the elastic part that is contained in the elastic field E_{el} outside the radius the extension of the dislocation core r_0 and from the energy stored in the core E_{core}, which cannot be described within the theory of elasticity.

$$E = E_{el} + E_{core} \tag{2.1}$$

The elastic energy is defined in the cylinder construction with the radius R containing the dislocation. For screw and edge types of dislocations it is slightly different:

$$E_{el}^{screw} = \frac{G \times b_s^2}{4p} \ln \frac{R}{r_0} \tag{2.2}$$

$$E_{el}^{edge} = \frac{G \times b_e^2}{4p(1-n)} \ln \frac{R}{r_0} \tag{2.3}$$

Here, G stands for the shear modulus, p is the pressure and n is the Poisson's ratio. The core energy can be approximated with the value

$$E_{core} = \frac{Gb^2}{2p} \tag{2.4}$$

From Eq. 2.1-2.4 it follows that the line energy of an edge dislocation is always larger than that of a screw dislocation. The elastic part of the energy depends logarithmically on the crystal (grain) size expressed in R. The radius of the dislocation core can be evaluated as the magnitude of the Burgers vector and the logarithm can be neglected. Then it yields very general formula for the line energy of a dislocation:

$$E \propto G \times b^2 \tag{2.5}$$

The tendency of energy to be minimal results in the smallest possible Burgers vector of an dislocation.

Another type of linear defects is a disclination being usually considered in liquid crystals. It is a defect in the orientation of director whereas a dislocation is a defect in positional order [13].

2.1.2 Planar defects

Planar or two-dimensional defects are interfaces between homogeneous regions of the material. Planar defects include stacking faults, grain boundaries, twin boundaries and external surfaces.

A stacking fault (SF) is an interruption in the regular stacking sequence of atom close-packed planes, in which the interaction between the atoms is the strongest. The close packed structures are face-centered cubic (fcc) structure with ABCABCABC stacking order and hexagonal close packed (hcp) structures

with ABABABAB stacking order. Two types of SFs referred in generally as intrinsic and extrinsic are possible in these structures. They are described by removal or introduction of an extra layer respectively.

SFs play an important role in the plasticity of crystals. The presence of SFs in the crystal leads to the formation of grain boundaries and thus prevents the single crystal growth. The intrinsic SFs can be easily produced by a sliding process. The SFs are terminated either on the crystal and grains boundaries or on partial dislocation inside the single crystal. The destroy of perfection of the crystal by SFs is associated with energy per unit area known as stacking-fault energy. Its typical value lies in the range between 1 and 1000 mJ/m^2 [10]. The overview of SFs arisen in hexagonal lattice is given in Sec. 2.2.3.

Crystalline solids usually consist of a large number of randomly oriented grains separated by grain boundaries. Grains can range in size from nanometers to millimeters across. The size of the grains can be controlled by the cooling rate during the material growth. Rapid cooling produces smaller grains whereas slow cooling results in larger grains. Each grain is usually rotated with respect to neighbouring grains. Depending on this angle of rotation, small-angle (subgrain) or large-angle grain boundaries are distinguished. A large-angle grain boundary of the boundary region is referred to the randomly oriented crystal regions whose orientation difference exceeds an angle of 15^o. The grain boundaries produce a disturbance within a grain, limit the lengths and motions of dislocations and affect the grain boundaries of the neighbouring crystallites [14].

Twinning is a process in which a region of a crystal undergoes a homogeneous shear resulting in original crystal structure in a new orientation known as a twin [15]. The twin can be considered as a mirror image of the original (parent) crystal in the composition plane. A twin boundary is the boundary surface between the two parts of a twin crystal (see Fig. 2.4). Twinning usually occurs in the early stages of crystallization, during intergrowth of two or more crystalline parts. Their regular orientation with respect to the principal crystallographic directions are usually preserved. Sometimes deformation twinning can be induced by plastic deformation. Twins are typically observed in bcc and hcp metals and non-metallic crystals.

A real crystal has a finite size and thus a surface. It causes an interruption of the translational symmetry. Therefore the crystal surfaces can be considered as an interface between the homogeneous crystal and another phase. The atomic structure in the vicinity of this interface strongly depends on the state of matter of the chemical composition and crystallographic orientation of the second phase.

2.1.3 Another defects

The most important defects studied in GaN and its are classified as to one- or two-dimensional. However, the crystalline solids can possess another types of defects, which short description is given in this section.

Point or zero-dimensional defects are defects that have the extension of a single atom and are formally limited to a single lattice site. They occur during heating, doping, plastic deformation, in the process of crystal growth and as a result of radiation exposure. There are two types of point defects in the crystal lattice: intrinsic and extrinsic point defects [16].

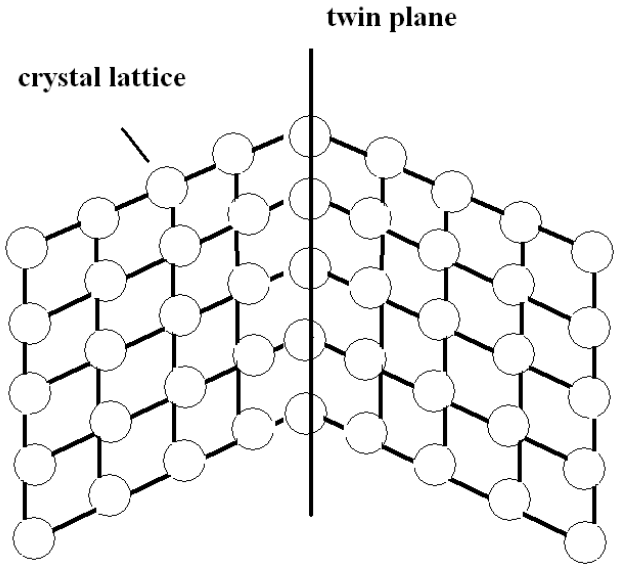

Figure 2.4: The sketch of the twin structure.

In pure materials two types of point defects are possible called intrinsic, namely a vacant atomic site site or vacancy, and a self-interstitial atom [10]. A vacancy is a place in the regular arrangement of atoms in the crystal lattice, which is unoccupied i.e. vacant. It is formed by the removal of an atom from an atomic site. Self-interstitial defects are atoms of the same type as the crystal lattice that occupy non-lattice sites in the crystal structure. Since ionic crystals are forced to be charged neutrally, it can not come to a single point defect in these structures. The same atom thus creates both vacancy and interstitial called a Frenkel defect. Another possible defect configuration arises when oppositely charged ions leave their lattice sites, creating vacancies, known as Schottky defect.

Impurity atoms in a crystal can be considered as extrinsic point defects. They play an important role in the mechanical properties and conductivity of the materials. They can be also divided into two types: substitutional and interstitial. Substitution atoms occur in lattice sites which are occupied in a regular lattice with a different atom type. A special case of substitutional defect is a color center, where an anion is replaced by an electron. The only atoms with similar sizes and electronic properties can substitute each other. The extrinsic interstitial is the impurity atom at a non-lattice site. The interstice sites between atoms have usually less volumes then one atomic volume and the impurities cause large distortions among the surrounding atoms. They are generally high energetic configurations and can increase the total volume of crystal [17].

Antisite defects occur in an ordered alloy or compound when atoms of different type exchange positions. They do not belong to any type of defects mentioned above [18].

Bulk defects in a crystal, also known as volume defects or three-dimensional, include voids and precipitates of extrinsic and intrinsic point defects.

Voids are regions where there are a large number of atoms missing from the lattice. They can occur for a number of reasons. When voids occur due to air bubbles becoming trapped when a material solidifies, it is commonly called

porosity. When they occur due to the shrinkage of a material as it solidifies, it is called cavitation.

Each impurity introduced into a crystal has a certain level of solubility, which defines the concentration of the impurity that the solid solution of the host crystal can accommodate. Impurity solubility usually decreases with decreasing temperature. If an impurity is introduced into a crystal at the maximum concentration allowed by its solubility at a high temperature, the crystal will become supersaturated with that impurity once it is cooled down. A crystal under such supersaturated conditions achieves equilibrium by precipitating the excess impurity atoms into another phase of different composition or structure. Precipitates are considered undesirable because they have been known to act as sites for the generation of dislocations. Dislocations arise as a means of relieving stress generated by the strain exerted by precipitates on the lattice [19].

2.2 Structural defects in GaN layers

In this section, we make a review of the most typical structural defects presented in c-plane and a-plane GaN films, i.e. in the heteroepitaxial layers with [0001] and $[11\bar{2}0]$ surface orientation respectively. Threading and misfit dislocations are two types of line defects generally observed in polar layers, whereas stacking faults and partial dislocations occur rarely and their densities are relatively low. In high-quality c-plane GaN films, the stacking disorder and partial dislocations usually are located in the region in immediate adjacency to the substrate and are associated with the growth of a disordered low-temperature nucleation layer [20]. However a-plane GaN layers contain another extended defects, namely stacking faults (SFs) terminated by partial or stair-rod dislocations.

2.2.1 Threading dislocations in c-plane GaN

[0001]-oriented GaN layers contain large number of threading dislocations (TDs) with dislocation lines along [0001] direction. They originate at the interface, propagate through the layer and reach the surface except those that annihilate each other. Threading dislocations can be the basis for the formation of nonradiative recombination and scattering centers that affect carrier mobility [21].

TDs can be divided into 3 types the edge, the screw and the mixed dislocations with Burgers vectors $\boldsymbol{b}_e = \frac{1}{3}\langle 11\bar{2}0\rangle$, $\boldsymbol{b}_s = \langle 0001\rangle$ and $\boldsymbol{b}_m = \frac{1}{3}\langle 11\bar{2}3\rangle$ respectively. Any mixed dislocation can be easily decomposed into pure edge and screw components, how is depicted in Fig. 7.1. In our work, we do not consider mixed TDs separately. The pure edge and pure screw dislocations are termed as a-type and c-type, both with dislocation lines in [0001] direction.

Each dislocation type is associated with a local lattice distortion [22]. These distortions are often approximated by the mosaic model, which assumes that the film consists of perfect blocks which are tilted or twisted with respect to each other [23]. Each block is separated from the surrounding ones by faults and cracks. Edge threading dislocations conform to a lattice twist and screw threading dislocations conform to a lattice tilt.

The density of TDs depends on the misfit between the substrate material and

GaN, growth technique and conditions. It is typically of order $10^8 - 10^{10}$ cm^{-2} but a lot of attempts have been made by growers to reduce TDs density as much as possible. The systematic research enables to report that the density of screw TDs is one to two orders of magnitude lower than the density of edge TDs [3, 24]. The ratio of the elastic energies $\frac{E_{screw}}{E_{edge}}$ is about 1.66, which confirms the statement above. Pure edge dislocations have a tendency to to bend and annihilate. It means, their density near the surface is much lower than at the interface [1]. This feature is pronounced especially in GaN compounds (a good example could be found in Sec. 7.4).

The displacement field caused by both types of dislocations with Burgers vector $\boldsymbol{b}_s$ and $\boldsymbol{b}_e$ can be estimated using expressions taken from [25]. These formulae include the surface relaxation, however they are cumbrous and require simplifications, if the dislocation lines are perpendicular to the sample surface. In this case the parameter α is considered in the limit $\alpha \to 0$. For a pure screw threading dislocation the components of displacement field are:

$$\begin{aligned} u_x(\boldsymbol{r}) &= \frac{b_s}{2\pi}\frac{y}{R-z}, \\ u_y(\boldsymbol{r}) &= -\frac{b_s}{2\pi}\frac{x}{R-z}, \\ u_z(\boldsymbol{r}) &= \frac{b_s}{2\pi}\arctan\frac{y}{x}, \end{aligned} \tag{2.6}$$

where $R^2 = x^2 + y^2 + z^2$ and b_s is the length of the Burgers vector.

The vertical component of displacement produced by an edge threading dislocation is simplified to

$$u_z(\boldsymbol{r}) = \frac{\nu}{1-\nu}\frac{Rb_e}{2\pi}\frac{z + 2r(\nu - 1)}{R(R-z)}, \tag{2.7}$$

while expressions for the remaining components are much more complicated. Their explicit values can be found in Appendix A in the text of our software. In Eq.(2.7), ν is Poisson ratio and b_e is the length of the Burgers vector of edge dislocation.

2.2.2 Misfit dislocations in c-plane GaN

The difference between lattice parameters of GaN epitaxial layer and substrate crystals gives rise to elastic strains. These can relax by formation of surface undulations, of three-dimensional islands and of misfit dislocations (MDs). The first two mechanisms take place during the initial stages of epitaxy while the latter process is a dominant mechanism for comparatively thick layers. The dislocation densities vary from several dislocations per sample at initial stages of the relaxation process to a dislocation per 10-100 lattice spacings in completely relaxed heteroepitaxial systems with large mismatch [26].

MDs are confined to the interface between the GaN epitaxial layer and the substrate interface. They are not supposed to thread up into the layer and are very efficient in relieving strain. However, threading dislocations can be interconnected to the misfit dislocation network. As the misfit in the in-plane

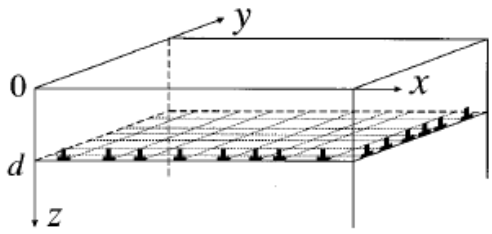

Figure 2.5: Geometry of the network of the misfit dislocations in a layered heteroepitaxial system taken from [26].

lattice constant between the epitaxial film and the substrate increases, the spacing of misfit dislocations decreases, and for high values of misfit the interface is incoherent. If the misfit is not large, the interfacial area of GaN/substrate can exhibit zones without extended defects [1].

When dislocation densities exceed about 10^3 cm^{-1} the strain relaxation can be calculated from the lattice-parameter measurements. The presence of MDs gives rise to substantial broadening of the x-ray diffraction peaks. With the film thickness increase the dominant contribution to the peak width comes from TDs.

Kaganer et al. developed the theory enabling to calculate the density of MDs in zinc-blende GaAs material [26]. The misfit dislocations observed in heteroepitaxial GaAs layers belong mostly to 60^o glide dislocations, i.e. the angle between their Burgers vectors and dislocation lines is 60^o. They can be divided into screw and edge ones. If the dislocation lines coincide with y axis (see Fig. 2.5), the Burgers vector of pure screw misfit dislocation can be represented as $\boldsymbol{b}^{(s)} = (0, \pm b_y, 0)$ in three-index Miller notation. The edge MDs can possess either $\boldsymbol{b}^{(e)} = (b_x, 0, \pm b_z)$ (glide dislocations) or $\boldsymbol{b}^{(e)} = (b_x, 0, 0)$ (sessile dislocations) Burgers vectors, where x- and z-components refer to misfit and tilt respectively. Any mixed misfit dislocation can be decomposed into pure screw and pure edge one.

It was found that the relaxation of polar GaN film on the substrate gives rise to only 60^o edge sessile (or Lomer type) MDs that are able to glide along the interface and may order to reduce the elastic energy. Experimental TEM data revealed that their Burgers vector is $\boldsymbol{b} = \frac{1}{3}\langle 11\bar{2}0\rangle$ [27].

The displacement field due to an edge dislocation with the Burgers vector parallel to the surface $\boldsymbol{b} = (b_x, 0, 0)$ can be represented as a sum of three items: displacement due to a dislocation in the infinite medium (1), the image dislocation (2), and an additional term (3). The second and the third items compensate the first one so that the condition of stress-free surface is fulfilled. Choosing the coordinates system as shown in Fig. 2.5 the non-zero components of displacement field remain in x and z directions. Then the displacement field caused by sessile edge dislocation in the isotropic half-space on a given distance d from the surface can be written as follows [26, 28]:

$$u_{1x} = -\frac{b_x}{2\pi}\left[\arctan\frac{z-d}{x} + \frac{\alpha x(z-d)}{x^2+(z-d)^2}\right], \tag{2.8}$$

$$u_{1z} = \frac{b_x}{2\pi}\left[\frac{1-\alpha}{2}\ln(x^2+(z-d)^2) + \frac{\alpha x^2}{x^2+(z-d)^2}\right], \tag{2.9}$$

$$u_{2x} = \frac{b_x}{2\pi}\left[\arctan\frac{z+d}{x} + \frac{\alpha x(z+d)}{x^2+(z+d)^2}\right], \tag{2.10}$$

$$u_{2z} = -\frac{b_x}{2\pi}\left[\frac{1-\alpha}{2}\ln(x^2+(z+d)^2) + \frac{\alpha x^2}{x^2+(z+d)^2}\right], \tag{2.11}$$

$$u_{3x} = \frac{b_x d}{\pi}\left[\frac{(1-\alpha)x}{x^2+(z+d)^2} - \frac{2\alpha x z(z+d)}{(x^2+(z+d)^2)^2}\right], \tag{2.12}$$

$$u_{3z} = -\frac{b_x d}{\pi}\left[\frac{z+d}{x^2+(z+d)^2} + \frac{\alpha z((z+d)^2-x^2)^2}{(x^2+(z+d)^2)^2}\right] \tag{2.13}$$

Here, $\alpha = \dfrac{1}{2(1-\nu)}$, where ν is the Poisson ratio.

The total displacement produced by an edge misfit dislocation is then:

$$u = u_x + u_z = \sum_{i=1}^{3} u_{ix} + \sum_{i=1}^{3} u_{iz} \tag{2.14}$$

Recently Kaganer et al. developed Monte Carlo simulation method of x-ray diffraction and determined the density of MDs in polar GaN/SiC [29]. The dislocation with the linear dislocation density ρ were generated at the interface as a stationary Markov chain. Once the position of a dislocation x_j was specified, the position of the next dislocation was selected as $x_{j+1} = x_j + \delta x$. The increment δx taken from the gamma distribution (for $\gamma = 1$ they are considered uncorrelated) defines the density of MDs: $\langle \delta x \rangle = \rho^{-1}$. The displacement field caused by MDs is calculated as a sum of the contributions of the individual dislocations:

$$\boldsymbol{U}(x,z) = \sum_j \boldsymbol{u}(x - x_j, z), \tag{2.15}$$

where $\boldsymbol{u}(x,z)$ is the displacement due to a dislocation located at (0,d). It is determined from the equations 2.8-2.13 modified for four-index notation.

2.2.3 Defects in a-plane GaN

Application of various growing methods enables to produce GaN films with surface orientation different from c-plane. [11$\bar{2}$0]-oriented a-plane GaN does not exhibit the quantum confined Stark effect occurring in polar [0001]-oriented material [30].

The hexagonal GaN is close packed in the [0001] direction. The stacking sequence can be written as ...AaBbAaBb..., where the capital letters correspond to Ga atoms and small letters to N atoms. The GaN molecule can be considered as a stacking unit and the small letters can be then omitted. During the growth process the cubic phase inclusions with the stacking sequence ...ABCABC... occur in the hexagonal matrix yielding violation of the stacking rules in basal (0002) planes. These imperfections are called basal stacking faults (BSFs). The energy of BSFs formation is proportional to the number of inserted cubic bilayers in the stacking sequence. They can be divided into extrinsic (E) and three intrinsic (I1-I3) types [31].

The I1 type of BSFs is formed by insertion or removal of a basal plane with further $1/3\,\langle 1\bar{1}00\rangle$ slip of one part of a crystal with respect to the other to decrease the fault energy. It is surrounded by sessile Frank-Shockley dislocations. I1 BSF

Stacking fault type	$\boldsymbol{R}$	Stacking sequence	Dislocation type on SFs bounds	$\boldsymbol{b}$
I1	$\frac{1}{6}\langle 20\bar{2}3\rangle$	ABABCBCBC	Frank-Shockley partial	$\frac{1}{6}\langle 20\bar{2}3\rangle$
I2	$\frac{1}{3}\langle 1\bar{1}00\rangle$	ABABCACAC	Shockley partial	$\frac{1}{3}\langle 1\bar{1}00\rangle$
I3	none	ABABCBABA	none	none
E	$\frac{1}{2}\langle 0001\rangle$	ABABCABAB	Frank partial	$\frac{1}{2}\langle 0001\rangle$
Prismatic	$\frac{1}{2}\langle 10\bar{1}1\rangle$	along $\{\bar{1}2\bar{1}0\}$ planes	Stair-rod	$\frac{1}{6}\langle 10\bar{1}0\rangle$, $\frac{1}{6}\langle 3\bar{2}\bar{1}0\rangle$

Table 2.1: Stacking faults with the displacement vectors $\boldsymbol{R}$ observed in a-plane GaN layers and linear defect with the Burgers vectors $\boldsymbol{b}$ considered as bounds of SFs.

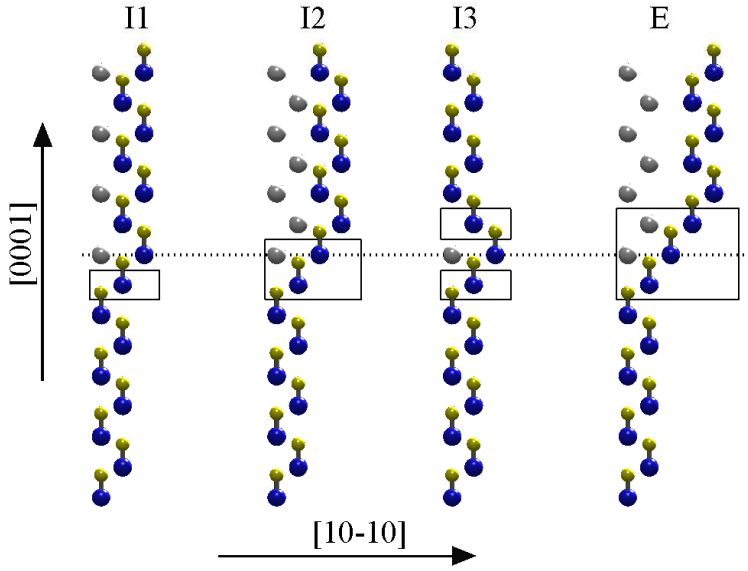

Figure 2.6: Sketch of the positions of Ga (blue) and N atoms (yellow) in various types of basal stacking faults. The fault plane is denoted by the dotted line. The black rectangles denote the segments with fcc-like stacking. Grey spheres denote the Ga positions in an ideal lattice. The picture is taken from [32].

has the lowest energy of formation and it appears in the film during its growth process.

The I2 BSF appears due to $1/3\langle 1\bar{1}00\rangle$ shear of one part of a crystal with respect to the other or due to dissociation of a perfect dislocation with $\boldsymbol{b} = 1/3\langle 11\bar{2}0\rangle$ into two Shockley partial dislocations with $\boldsymbol{b} = 1/3\langle 1\bar{1}00\rangle$. This type of SFs can be formed either during the growth by stress or after it by movement of a glissile Shockley dislocation in the basal plane.

The I3 BSF is characterized by occupation of so called "wrong" C position with A or B layers. It can be considered as a sum of two I1 SFs. However, the I_3 stacking faults have formation energy slightly less than twice the formation

energy of the I1 defect [33].

The extrinsic BSF can be observed when extra basal plane is inserted into the normal stacking sequence. This fault is bounded by Frank type partial dislocation with $\boldsymbol{b} = 1/2[0001]$ creating a dislocation loop. The E type BSF is formed by precipitation of point defects on the basal plane and has the highest energy of formation besides all SFs, so it is generally not observed in experiments.

The planar defects are reported to exist not only in the basal planes of nonpolar GaN layers. The prismatic stacking faults (PSFs) lie in prismatic $\{\bar{1}2\bar{1}0\}$ planes and terminate BSFs. Stair-rod dislocations are observed at the intersections of PSFs and BSFs, since the intersecting faults had different fault vectors. A zigzag-like propagation from substrate toward the GaN layer surface is exhibited by PSFs. It is believed that such zigzag-like behaviour decreases the total energy of the PSFs [34].

The stacking of the (0001) basal planes with all types of BSFs is shown in Fig. 2.6. Basal and prismatic SFs with their bounds are summarized in Table 2.1. The displacement vectors of SFs and the Burgers vectors of dislocations are given there as well [22].

Nonpolar a-plane GaN films are commonly reported with a BSFs density of order $10^5 - 10^6$ cm^{-1} and a dislocation density of 10^{10} cm^{-2}. The density of PSFs was observed less than 10^2 cm^{-1}, so their presence in material can be often neglected.

3. Growth of GaN Thin Heteroepitaxial Layers

3.1 Types of GaN layers

GaN is nowadays one of the most promising wide band gap semiconductors. However, achievement of its full potential has still been limited by a dramatic lack of suitable GaN bulk single crystals. GaN has a high melting temperature and a very high decomposition pressure; therefore it cannot be grown using conventional methods like Czochralski or Bridgman growths [35]. GaN and is typically grown in the form of epitaxial layers on sapphire or 6H-SiC substrates. The main challenge for growers of GaN is to achieve high quality materials i.e. to reduce the density of TDs occurring due to the lattice mismatch and difference in thermal expansion between wafers and deposited films.

GaN can be epitaxially grown in either hexagonal (wurtzite) or cubic (zinc-blende) structure depending on the substrate symmetry and growth conditions [4]. There is a small difference between the energies of their formation and direct band gaps.

3.1.1 Cubic GaN films

Zinc-blende structure is usual for III-V semiconductors. Due to higher crystallographic symmetry it possesses superior electronic properties for device applications. It can be easily doped by n- and p-type impurities, while in hexagonal GaN doping is not a trivial procedure. The electrons have higher saturated velocities because of reduced photon scattering. Due to its central symmetry the cubic GaN does not display spontaneous or piezoelectric effects, which makes these material competitive to nonpolar and semipolar hexagonal GaN [22]. The possibility of cleaving atomically smooth surfaces along the stable (100) facets allows to use cubic GaN for lasers [36].

In contrast to hexagonal phase of GaN the cubic one is metastable that requires for its growth nonequilibrium methods and appropriate substrates stable at the high growth temperature [37]. The most common sapphire substrate material has hexagonal structure that results in growth of subsequent film in hexagonal phase. Typically cubic phase epilayers include a few volume percent of hexagonal GaN, which interferes with device applications. It yields development of new challenging methods to obtain materials with the lowest possible inclusions of hexagonal phase [38].

Another possible wafers for cubic GaN growth are GaAs and SiC. However, due to the large lattice mismatch, these substrates produce a strain within the epitaxial layers. The energy of $\langle 111 \rangle$ SFs formation is relatively low, so they are the main mechanism to relieve the strain in the film. There SFs can be considered as hexagonal phase inclusions. Besides $\langle 111 \rangle$ oriented SFs, threading dislocations can also occur in cubic GaN. Their presence negatively affect the working characteristics of devices based on GaN material.

A lot of works are devoted to study of cubic GaN material and improving of

its growth process [39, 40]. None the less in our research, we focus on hexagonal epitaxial GaN layers and consider their properties depending on their orientation on a substrate.

3.1.2 Polar (c-plane) GaN films

Hexagonal GaN is usually grown heteroepitaxially on foreign substrates such as (0001)-sapphire or SiC so that its (0001) planes make the surface. This film orientation is called c-plane or polar (see Fig. 3.1 a).

A large mismatch in the lateral lattice constants (14% in case of sapphire) give rise to a huge number of threading dislocations going perpendicular to the layer's surface. The density of TDs depends on the growth technique and parameters, layer thickness, miscut of the substrate etc. Exceeding critical value of 10^9 cm^{-2} TSs make GaN-based materials useless for certain industrial applications. Furthermore arrays of misfit dislocations emerge at the GaN/substrate interface revealing the stress. Such crystal imperfections negatively affect the electrical and optical properties of GaN-based devices as they work as very effective nonradiative recombination centres.

The usual way to improve the surface morphology, crystallinity and the electrical and luminescent properties of GaN layers is to deposit the nucleation layer (NL) with its subsequent annealing on the top of the substrate. AlN NL is one of the most powerful tool to decrease GaN/substrate mismatch. The optimal thickness of NL can be accessed by varying growth pressure, temperature and time [41].

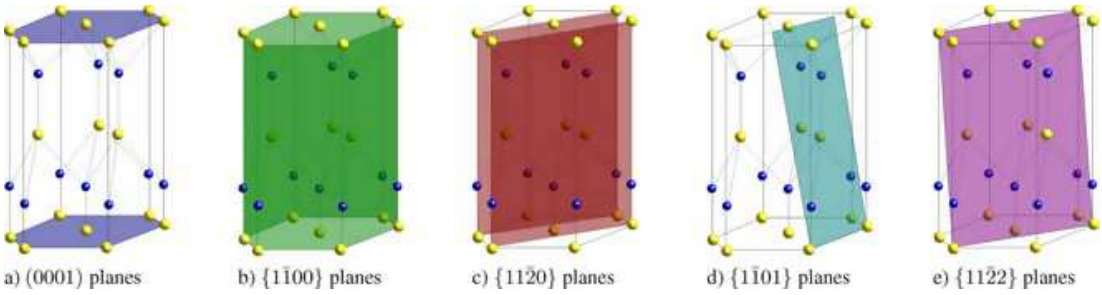

Figure 3.1: Commonly used surface orientations of GaN. Galium atoms are yellow, nitrogen atoms are blue. The sketch is taken from [42].

Polar GaN films are often used in optoelectronic devices. The spontaneous polarization fields arise along the [0001] direction. The discontinuity in total polarization in (0001)-oriented nitride-based interfaces in heterostructures results in significant fixed charges at the interfaces that may be beneficial or deleterious depending on the final device technology [43]. However, sometimes the efficiency of devices can be limited by a band bending known as the quantum confined Stark effect [30].

3.1.3 Nonpolar (a-plane, m-plane) GaN films

(11$\bar{2}$0)-oriented a-plane and (10$\bar{1}$0) m-plane GaN layers are generally called nonpolar (see Fig. 3.1 b and c). This films do not cause the piezoelectric field because

their polar axis is parallel to the quantum well region. Thus, they do not exhibit the quantum-confined Stark effect.

Nonpolar a-plane GaN is typically grown on planar r-plane sapphire wafers. The major challenges are still related to the limited crystalline quality of the material [44]. Similar to c-plane GaN the misorientation of the wafers play an important role in the quality of a-plane GaN films. Besides r-plane sapphire, some other substrates for growth of a-plane GaN have been reported in the literature, namely a-plane SiC [45] and γ-$LiAlO_2$ [46]. However, GaN layers grown on such substrates do not reveal good surface and crystalline properties.

For non-polar and semipolar films, the thermal expansion coefficients and elastic constants of the film and the substrate are usually anisotropic in plane. For example, the thermal expansion coefficients of both GaN and sapphire are larger parallel to the a-axis than parallel to the c-axis. Non-polar films often show a higher wafer curvature parallel to [0001] direction than perpendicular to it and are often orthorhombically distorted [22].

Except large densities of dislocation (above 10^9 cm^{-2}), a-plane GaN possesses different types of stacking faults with total density exceeding 5×10^5 cm^{-1} (for details see Sec. 2.2.3). These densities can be slightly reduced by in-situ SiN or ex-situ ScN interlayer deposition. The epitaxial lateral overgrowth method significantly helps to improve the layer quality [47].

Even optimized growth of a-plane GaN results in non-smooth surfaces because freely growing GaN crystals usually do not develop a-plane facets, while m-plane and related semipolar facets are observed. This fact makes m-plane GaN more attractive for industrial applications. It is typically grown on m-plane SiC or γ-$LiAlO_2$. The average density of SFs are estimated as around 10^6 cm^{-1}, which is extremely high [48] but it can be decreased by epitaxial lateral overgrowth by one order of magnitude [49]. SiC material is very expensive and the use of sapphire wafers is of great importance. Nevertheless, only few attempts resulted in successful growth of m-plane GaN on m-plane sapphire [50].

3.1.4 Semipolar (r-plane) GaN films

Semipolar GaN layers include $(10\bar{1}2)$ r-plane , $(10\bar{1}1)$, $(10\bar{1}3)$, $(11\bar{2}2)$ and another orientations characterizing with non-zero last Miller index [51]. Some of them are shown in Fig. 3.1 d and e. The growth in one of possible directions depends on the substrate orientation, temperature and pressure during the growth. For instance, $(10\bar{1}2)$ structure is preferable at nucleation layer growth temperature of 1080^oC, while at higher temperatures $(10\bar{1}3)$ film orientation is dominant [44]. However, r-plane GaN is considered as the most promising nonpolar example due to its higher crystalline quality and favourable growth conditions. The most common wafer for r-plane GaN is m-plane sapphire; pure silicone or $MgAl_2O_4$ are used as well [52].

As it was mentioned in the previous section, non-polar GaN films have a lot of stacking faults. This problem is not revealed for c-plane epitaxy. Therefore SFs emergence can be overcome, if semipolar layers can be grown epitaxially in the c-direction. Several techniques are developed to obtain the improved GaN semipolar layers with reduced density of SFs. The growth of semipolar side-facets on c-plane GaN structures is the following. An ordinary c-plane epitaxial GaN

layer is covered by SiO_2 stripe-shape mask. Then the sample is given back to the subsequent growth, which occurs in the regions where is no deposited mask. Above the SiO_2 mask the growth continues laterally and coalesces into a planar surface. The mask can be either one- or two-dimensional grown on c-plane GaN or directly in the etched trenches of the sapphire substrate. The appropriate chose of the mask type and geometry yields the growth of differently oriented semipolar layers [44].

The density of SFs in such layers is less than in non-polar GaN by several orders [53]. It enables their wide application for optoelectronic devices. However, the reliable methods for SFs density determination are still needed.

3.2 Methods of GaN epitaxial growth

In this section, we demonstrate the most widely used techniques of GaN growth and analyse their advantages and disadvantages. We make an emphasis on c-plane GaN layers, nevertheless the growth of material with another orientation is mentioned as well.

3.2.1 Metalorganic vapour phase epitaxy

Metalorganic vapour phase epitaxy (MOVPE) is a chemical vapour deposition method of epitaxial growth of materials from the surface reaction of organic compounds or metalorganics and metal hydrides containing the required chemical elements. In contrast to molecular beam epitaxy (see Sec. 3.2.4) the growth of crystals is by chemical reaction and not physical deposition. There are variants of the basic phase technique such as hydride vapour phase epitaxy or liquid phase epitaxy (see Sec. 3.2.2 and 3.2.3). However MOVPE is the most common method to grow GaN and related compounds. Most of the current commercial device structures are fabricated using MOVPE [35].

The Ga sources are generally trimethylgallium ($Ga(CH_3)_3$) or triethylgallium ($Ga(C_2H_5)_3$) with the high purity of 99.9999%. Ammonia gas (NH_3) under the high pressure is the most widely used precursor. H_2 or N_2 is traditionally chosen as a carrier gas to transport volatile precursor molecules. The reaction between source and precursor can be written as $(CH_3)_3 + NH_3 \rightarrow GaN_{(solid)} + 3CH_{4(gas)}$. It does not requires high vacuum and can be performed at moderate pressure (2-100kPa). The temperature of MOVPE growth normally exceeds 1100°C.

The basic scheme of MOVPE reactor is shown in Fig. 3.2. One considers two orientation of reactors: horizontal and vertical. It depends on the direction of the gas flowing inside the device (parallel or perpendicular to horizontally mounted sample). Every reactor consists of four principal components:

- Reactor chamber.
- Gas inlet and switching system.
- Pressure maintenance system.
- Gas exhaust and cleaning system.

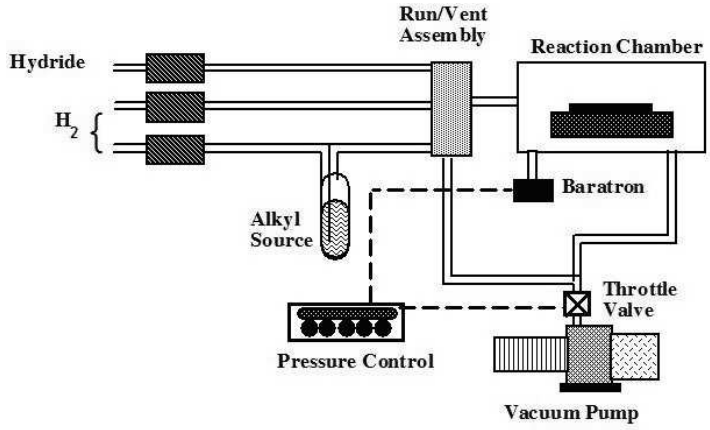

Figure 3.2: A scheme of horizontal MOVPE reactor system taken from Wikipedia.

The detailed description of all parts mentioned above can be found elsewhere [54–56].

The epitaxial growth of GaN on foreign substrates usually starts with thermal cleaning and deposition of a nucleation layer (NL) at lower temperature. This layer serves to reduce the lattice mismatch and in turn the density of TDs in GaN. Due to its appropriate lattice parameters AlN is often used as a material for buffer layer [57, 58]. 2D and 3D nucleation processes are distinguished in literature [59]. Thermal annealing and subsequent MOVPE growth of GaN layer are followed the NL [60].

Epitaxial lateral overgrowth (ELO) is widespread technique for improving the crystalline quality [61, 62]. ELO consists in local epitaxial growth of the dialectic nanomask (typically SiO_2 or SiN_X) with etched openings, which initially occurs in the direction normal to the surface of the substrate but then proceeds preferentially in the direction parallel to it. The upper GaN layer is deposited above the nanomask. The propagation of TDs is stopped by this mask so that they can reach the upper GaN layer only through the etched regions [63]. It results in dislocation bending and their drastic decrease in the top layer. Application ELO to MOVPE growth enables to obtain the GaN layers with total density of TDs of order $10^6 - 10^7$ cm^{-2}.

Laser reflectometry (LR) is a powerful tool for in-situ real time monitoring of the heteroepitaxial growth [64]. The information provided by LR is the change of refractive index of an epitaxial layer during its growth. It represents periodic oscillations damping due to absorption or scattering on the surface roughening.

Except the high quality of grown material MOVPE technique has a big number of advantages. A noteworthy factor in the widespread take-up of the technique is the high degree of flexibility in the design of precursor molecules. Since the growth processes are far from equilibrium, stable and metastable compounds can be grown. Almost any combination of layers and layer sequences can be deposited on almost any crystalline substrate. Nowadays MOVPE is the the principal engine for development and production of wide band gap semiconductors [4].

The weak points of MOVPE are environmental damage produced by gas exhaust and high demands to waver materials that should stay stable under the high temperature of epitaxial deposition. Due to the low growth rate, a thick bulk GaN film is not possible to be produced by MOVPE method.

3.2.2 Hydride vapour phase epitaxy

Hydride vapour phase epitaxy (HVPE) is an epitaxial growth technique often employed to produce III-V semiconductors. In general, HVPE is related to MOVPE method but there are a number of basic differences. HVPE process is usually hold at atmospheric pressure and close to thermodynamic equilibrium whereas MOVPE growth is non-equilibrium. It yield higher efficiency of grown material usage. The high growth rate (1 μm/min) in HVPE does not allow to control the growth process. Nevertheless it is a reason for substantial decrease of material cracking grown on foreign substrates. It makes possible to grow low-defect and low-cost thick films of GaN or its compounds [65].

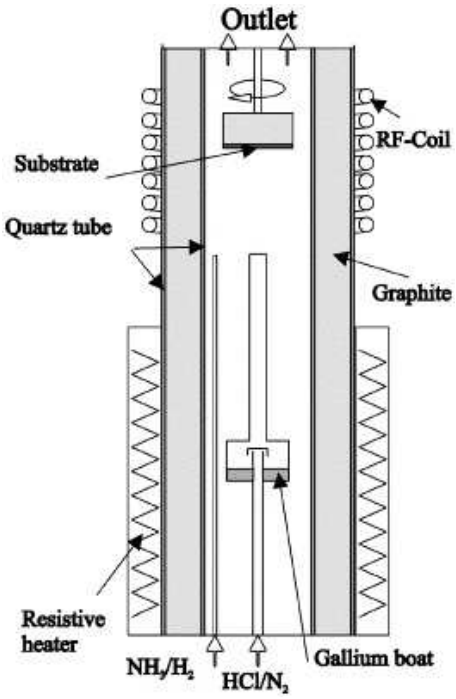

Figure 3.3: Schematic view of the inverted vertical HVPE growth reactor taken from [66].

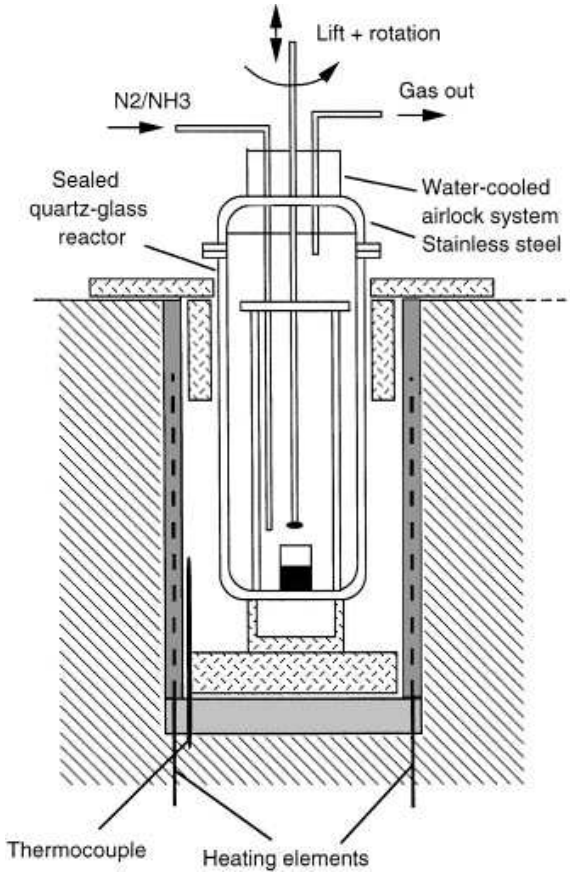

Figure 3.4: Schematic view of the LPE growth reactor system taken from [67].

For GaN HVPE, GaCl is typically used as precursor, ammonia (NH_3) or nitrogen halide (NCl_3) as nitrogen sources and HCl, N_2 or H_2 as carrier gases [66]. The most common way to obtain GaN is $GaCl + NH_3 \rightarrow GaN + HCl + H_2$. Another chemical reactions to produce GaN are discussed elsewhere [68].

The schematic drawing of the vertical growth reactor is shown in Fig. 3.3. Here, the GaCl is synthesized within the reactor in a Ga-boat by reacting HCl with Ga at 850–900 ^{o}C. The growth is done at atmospheric pressure in the temperature range 1000–1100^{o}C. Such temperatures are typical for HPVE growth of GaN [69]. The walls of reactor are heated to keep the constant temperature

inside the growing chamber. Some difficulties during the growth process are linked to the strong thermodynamic propensity for GaN to form undesirable gas phase reactions and wall deposition problems. Another problem is associated with destruction reactor equipment by highly corrosive HCl gas if leaks to air are not avoided.

The density of TDs in the GaN with c-plane orientation are strongly dependent on the layer thickness varying from 10^9 to 10^4 cm^{-2} [70]. However, except of TDs these layers possess a large number of stacking faults occurring due to very high speed of growth. Recently successful nucleation of GaN layers on sapphire substrates at intermediate temperature of 750-900^{o}C has been reported [71].

HVPE technique is often combined with epitaxial overgrowth by MBE and MOVPE. The layers grown in such way are shown comparatively low defect densities.

3.2.3 Liquid phase epitaxy

Liquid phase epitaxy (LPE) is a method of crystal layers growth from the melt on crystalline oriented substrates [72]. It is mainly used for the growth of compound semiconductors resulting in very thin, uniform and high quality layers. The temperatures of the process has to be below the melting point of the deposited material. The solvent element can be either a constituent of the growing solid or some other low-melting metal like Sn, Bi or Pb, which is incorporated into the solid only as a dopant. The slow and uniform growth requires conditions close to equilibrium between dissolution and deposition, which is very sensitive to the temperature and the concentration of the dissolved material in the melt as well as to the substrate orientation. The growth of the layer from the liquid phase can be controlled by a forced cooling of the melt.

The growth of GaN and its compounds is less common by LPE than by another methods. However among the different techniques used to grow thick GaN films and crystals, LPE is the most promising. GaN films are grown on typical sapphire or SiC substrates as well as on challenging $LiGaO_2$, $LiAlO_2$ or AlN materials[67, 73].

An example of LPE vertical reactor system used for single crystalline GaN growth is shown in Fig. 3.4. The GaN LPE layers are grown from pure Ga or Ga + metallic additive solutions. The additives significantly increase the growth rate of GaN [74]. Ammonia is used as a source and H_2 or N_2 as a carrier gas. The chemical reaction of GaN formation can be represented as follows: $Ga + NH_3 \rightarrow GaN + \frac{3}{2}H_2$. After thermal and chemical reactor cleaning, Ga solution is introduced into the crucible from the top of the reactor through an airlock system. The chamber is heated up to a temperature above $T_{saturation}$ in order to obtain a homogeneous mixture of the solution constituents. Then it is cooled down to the growth temperature (about 900-1050^{o}C), and the substrate fixed on the substrate holder is dipped into the solution and rotated. Growth is stopped by removal of the substrate, and the reactor is subsequently cooled down quickly to avoid thermal degradation of the grown layer. Several films can be successively grown, the limitation being the formation of gallium oxide or other contaminants[67].

The typical density of TDs in c-plane LPE grown GaN exceeds 10^9 cm^{-2}.

LPE technique is often combined with MOVPE and HPVE to achieve the best material characteristics. For example, MOCVD sapphire/GaN and HVPE free-standing GaN substrates gives material with excellent quality [75]. Non-polar m-plane and a-plane MOVPE GaN samples grown on LPE-GaN substrates by the Na flux method were shown reduced to 10^7 cm^{-2} dislocation densities [76].

An alternative to conventional LPE technique is low-pressure solution growth (LPSG) performed at ambient pressure. With this method the density of TDs in c-plane GaN are reported to be reduced to 5×10^8 cm^{-2} [77].

Among the drawbacks of LPE technique it is worth to mention that growth of thin epitaxial layers (less than 100 nm) is very difficult to control. The growth rate is not constant during the whole process and is maximal in the beginning. The surface flatness of LPE materials strongly depends on the misorientation, supersaturation and dopant used. In contract to another methods, an in-situ characterization of the growing layer is impossible in LPE, because the epilayer is hidden by the metallic solution [72].

3.2.4 Molecular beam epitaxy

Molecular beam epitaxy (MBE) is a technique for epitaxial growth via the interaction of one or several molecular or atomic beams that occurs on a surface of a heated crystalline substrate [78, 79]. The general principles of this technique is similar to MOVPE (more detailed in Sec. 3.2.1). The major differences between them are the more kinetic, non-equilibrium growth mechanism of MBE and superior in-situ measurement capabilities, which have made the growth process simpler to understand and provided superior control of interfaces and atomic layer structures.

A molecular beam is defined as a directed ray of neutral molecules or atoms in a vacuum system produced by heating a solid substance contained in an effusion cell [80]. It is guided by a set of slits and shutters onto a substrate. Under the certain conditions, governed mainly by kinetics, the beam would condense resulting in nucleation and growth [81]. Despite a simplicity of this method, it requires special conditions for successful growth of heteroepitaxial layers:

- The ultra high vacuum (UHV) of about 10^{-8} Pa is the essential environment for MBE. Therefore the rate of gas evolution from the materials to the chamber has to be as low as possible.
- The source materials should possess the purity of 99.999999%.
- The molecular source has to evaporate refractory materials (such as metals) and adjust the flux density of the substance.

The typical scheme of MBE system is depicted in Fig. 3.5. The solid sources materials are placed in evaporation cells to form an angular distribution of atoms or molecules in a beam. The substrate is heated to the necessary temperature and continuously rotated to improve the growth homogeneity. A spectral mass analyzer [82] is used to monitor the environment inside the chamber. For the crucibles of the MBE machine pyrolytic boron nitride (PBN) is often chosen. It gives low rate of gas evolution and chemical stability up to 1400 ^{o}C. Molybdenum

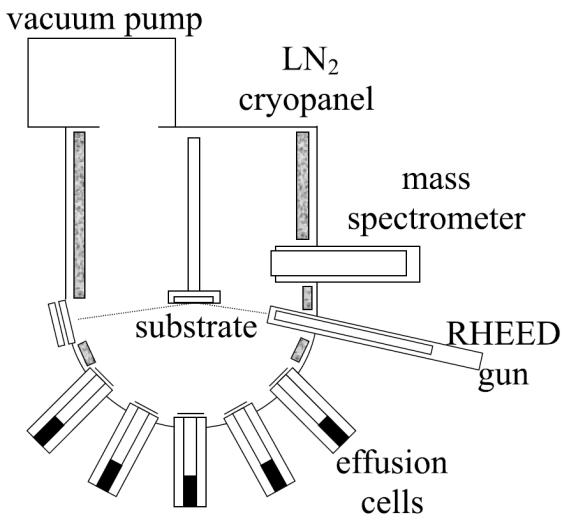

Figure 3.5: A typical MBE system taken from [79].

and tantalum with excellent refractory properties are widely used for shutters, heaters and other components of the device. A cryogenic screening around the substrate is required to minimize spurious fluxes of molecules and atoms from the walls of the chamber.

The control of composition and doping of the growing material at monolayer level is performed by opening and closing mechanical shutters. Their typical operation time is about 0.1 s that is much shorted than time needed to create one monolayer (about 5s). The flux of every component is controlled by variation of the cells temperature.

Due to UHV inside the chamber many in-situ characterization tools are used in such systems, for instance reflection high energy electron diffraction (RHEED) [83], scanning electron microscopy (SEM) [84] or Auger spectroscopy [85].

GaN layers are commonly grown by MBE technique. Except Ga effusion cell the MBE chambers can be equipped with Si and Mg cells for n- a p-type doping, as well as In or Al for growth of InGaN and AlGaN compounds [86]. The density of threading dislocations in GaN films grown with MBE method on SiC porous template is estimated of order 10^{10} cm^{-2} [87]. With refined procedures, however, dislocation densities of 10^8 order can be obtained when grown directly on sapphire substrates with AlN or GaN buffer layers. The MBE templates is often used for the subsequent MOVPE or HPVE overgrowth improving the material quality and reducing the TDs densities by one-two orders [88].

However, the major disadvantage of MBE technique is a relatively low temperature of GaN growth (700-800 ^{o}C). It yields decomposition of GaN film into Ga and N_2 because of thermodynamic instability of GaN under UHV. Low temperature of the substrate reduces surface atom mobility leading to high densities of TDs in GaN epilayer [89]. This problem can be avoided for ternary materials by increase the surface adatom mobility with surfactant impurities (In, Al, As e.g.).

MBE technique is used in the fabrication of certain optoelectronic devices based on GaN, such as laser diodes for CD player optical pick-ups. Nowadays the usage of this method is much less common than LPE, MOVPE and other techniques. However, MBE is especially appropriate for the fabrication of electronic

devices and it is a key tool in the mass production of transistors and diodes for applications such as mobile phones and satellite receivers [4].

3.3 Series of samples grown for our investigation

The goal of our study is to determine the density of defects (threading dislocations in case of c-plane and basal stacking faults in case of a-plane GaN) in heteroepitaxial layers. Our collaboration with Institute of Optoelectronic in Ulm University (Germany) gave us an opportunity to obtain the series of samples appropriate to our investigations. A model system for our research consisted of three series of samples, namely c-plane GaN, a-plane GaN and c-plane $Al_{0.2}Ga_{0.8}N$. Each sample from all series differed from another ones in growing mode that led to different defect densities.

3.3.1 c-plane GaN

A series of four c-oriented GaN thin films with different dislocation densities was grown by metal-organic vapor phase epitaxy in an AIXTRON 200/RF-S horizontal flow reactor. All layers were grown on 2in c-plane (0001) epi-ready sapphire wafers slightly miscut by about 0.3^o toward the a-plane. This miscut has been shown to improve the optoelectronic properties of the layers[90, 91].

All samples were grown in four steps (Fig. 3.6). The growth of GaN films was carried out with trimethyl-aluminum (TMAl), trimethyl-gallium (TMGa) and high purity ammonia (NH_3) precursors and Pd-diffused hydrogen (H_2) carrier gas [57].

After thermal cleaning the reactor was cooled down to 950 ^{o}C and the nucleation was started. On top of the substrate, an oxygen doped 20 nm AlN nucleation layer was deposited. The optimized parameters for the nucleation were selected based on an analyses of the observed full width at half maximum (FWHM) of x-ray rocking curves in symmetric (0004) and asymmetric ($10\bar{1}4$) diffractions. The best reproducibility was demonstrated with a temperature of 920 ^{o}C, 10 sccm oxygen flow and 10 min deposition time, so these parameters were used to grow the series of samples.

The next step was a 360s annealing under hydrogen atmosphere and constant ammonia flow at 1140 ^{o}C. The optimized annealing conditions yield a reduced number of screw TDs whereas the formation of edge dislocations is not strongly affected [92]. The annealed AlN NL was followed by a 300 nm thick GaN buffer layer. The decrease of the reactor pressure (from 200 to 100 mbar) yielded increase of the GaN growth rate. It affected the quality of crystals so that surface smoothing by AFM and reduce of FWHM by x-ray measurements were observed. The buffer layer was nominally undoped and showed semi-insulating behaviour in resistivity measurements.

The large lattice mismatch between the GaN epitaxial layer and the substrate yields high dislocation densities up to the order of 10^9 cm^{-2} even in optimized samples. An in-situ deposited intermediate SiN_X layer with a submonolayer thickness reduces the density of edge threading dislocations, while the density of screw TDs remains almost unchanged[62]. In addition, the reduced edge TDs density lead to a smoothing of the sample surface. One disadvantage of the SiN

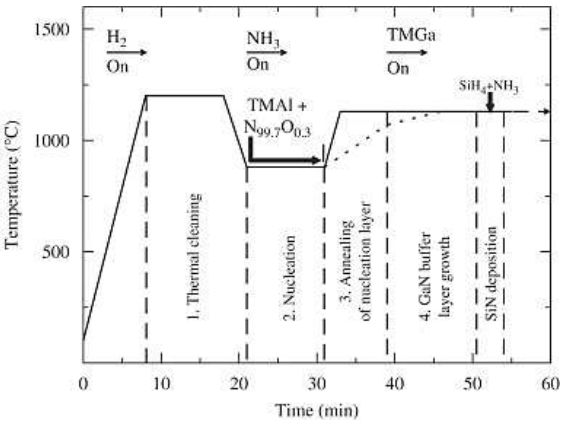

Figure 3.6: Temperature cycles during the four-step growth process (taken from [57]).

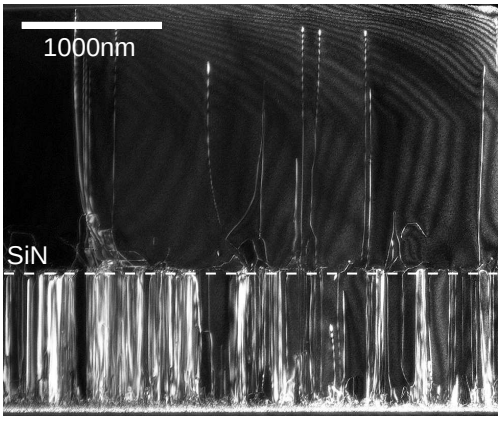

Figure 3.7: Transmission electron micrograph of the cross-section of the sample S1 (taken from [93]).

Sample	GaN thickness, (μm)	SiN_x deposition time, (s)	Total TDs density, ($10^8 cm^{-2}$)
S1	1.8	180	2.6
S2	1.8	150	4.8
S3	1.8	120	7.6
S4	2.4	0	20

Table 3.1: Characteristics of samples S1-S4 and total densities of TDs determined from EPD technique.

layer is the back-ground doping concentration ($n = 6 \times 10^{17} cm^{-3}$) that has not influence on the optical properties but makes material not useful in high electron mobility transistors[93, 94].

The SiN_X layer deposition was accompanied with decrease of ammonia flow to 500 sccm, stop of the Ga flow and opening the silane source. The dislocation density in the top GaN layer has been systematically varied by tuning the SiN_X interlayer deposition time between 0 and 180 s. The total thickness of the GaN film was 1.8 μm and 2.4 μm for samples with (S1-S3) and without (S4) the SiN_X layer, respectively (listed in Table 3.1).

TEM revealed that most of the threading dislocations are pinned at the SiN_X interface (Fig. 3.7) so that the dislocation density in the upper GaN layer is substantially reduced. From EPD studies (see Sec. 5), it has been found that the densities of threading dislocations in the upper layer decrease indeed with increasing SiN_X interlayer deposition time and vary between 2.6×10^8 and 20×10^8 cm^2 (see Table 3.1). These values can be compared with ones obtained from simulations and help us to estimate the accuracy of our approach.

3.3.2 a-plane GaN

The object of our further investigation is a series of four a-plane GaN samples denoted M1 to M4 grown heteroepitaxially on r-oriented sapphire substrates by metalorganic vapor-phase epitaxy (MOVPE) in an AIXTRON 200/RF-S horizon-

tal flow reactor [95]. TMGa, TMAl and ammonia (NH_3) have been used as Ga, Al, and N precursors and Pd-diffused hydrogen as a carrier gas. Before starting the growth, the substrate was heated up to 1200°C for 10 min in hydrogen atmosphere for a desorption of surface impurities. Then, the growth of all samples was initiated with an about 20 nm thick high temperature AlN nucleation layer. This layer significantly improved the morphology of a-plane GaN films and decreased the actual number of defects arisen due to mismatch in lattice constants between film and its substrate [96, 97].

We have chosen a series of samples with different growth conditions and different densities of defects. For sample M1, the AlN NL was followed by a GaN film deposited at the same temperature of 1120°C and a NH_3 to TMGa molar flow ratio (V/III ratio) of about 1100 to a total thickness of approximately 2.2 μm.

In order to optimize the GaN layer quality, a two-step procedure was applied to sample M3 where the V/III ratio was increased in the first step to a value of about 2200 for the growth of the first 1 μm owing to achieve best "bulk" crystal quality. Then, this parameter was reduced to about 540 for the growth of the top layer (2.3 μm) in order to minimize the surface roughness.

For sample M2, the first 1 μm thick GaN layer was grown applying an increased V/III ratio of about 2200, where a defect-reducing in-situ deposited SiN_X layer was integrated after 300 nm, similar as described in [62]. Then, the second SiN_X layer was deposited before about 2.3 μm GaN grown with reduced V/III ratio of about 540. Finally, an about 1 μm thick GaN top layer was grown at slightly increased temperature ($\Delta T = 20$K).

For sample M4, a template according to M3 was additionally overgrown by hydride vapor phase epitaxy to a total thickness of approx. 9 μm. This overgrowth was performed on horizontal flow Aixtron single-wafer system with high purity NH_3 and GaCl precursors. The carrier gas was a mixture of nitrogen and Pd-diffused hydrogen. The growing temperature was approximately 900°C and V/III ratio was about 18. The optimized HVPE overgrowth predicted the better quality of GaN film that has been proven by our simulations.

3.3.3 c-plane $Al_{0.2}Ga_{0.8}N$

One of the most important tasks of our study was to apply our method of TDs density determination developed for c-plane GaN layers to another materials. A good example of such material is AlGaN layers grown on sapphire exhibiting a large number of threading dislocations.

We investigated a series of 5 samples denoted A1 to A5 with different thicknesses (from 0.5 to 3.5 μm) of AlGaN top layer grown by MOVPE technique on (0001) sapphire substrates with a miscut of 0.3° towards the a-plane, in a low-pressure horizontal reactor (Aixtron AIX-200/4 RF-S) [98]. TMGa and TMAl were used as group-III precursors, and ammonia as group-V precursor. The Al content in the samples was confirmed by photoluminescence of about 20% [99]. For higher quality of AlGaN layer after the first nucleation layer of oxygen doped AlN with a thickness of about 60 nm followed the 150 nm interlayer of AlGaN grown at temperature of 1200°C.

An additional sample called A0 was studied in order to resolve complicated

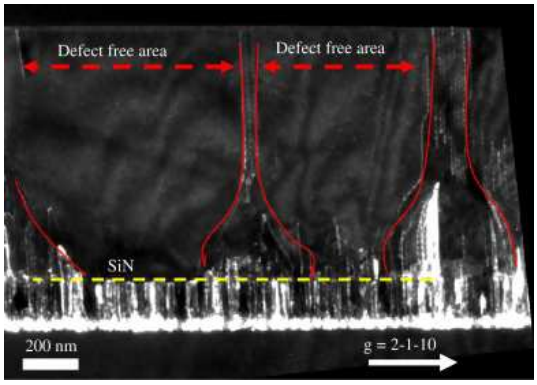

Figure 3.8: TEM from cross-section of the sample A2 taken from [98]. Edge TDs can reach the surface mostly in form of bundles.

diffraction patterns occurred in symmetrical diffraction (see Sec. 6.2). This sample has the same structure as the series A1-A5, however the thickness of AlGaN top overgrown layer is estimated to be about 90 nm, which is less that the 150 nm interlayer of AlGaN.

A common method to reduce the TD density in GaN layers is the use the SiN_X intermediated layers [57]. However, this technique does not reveal any visible improvements in crystal quality of AlGaN layers, since this material does not grow as selective as GaN [100]. Nevertheless the SiN_X masks deposited in-situ were recently successfully implemented to $Al_{0.2}Ga_{0.8}N$ [101]. Each of our samples has SiN_X mask with a submonolayer thickness produced in-situ from silane source during 4 minute of deposition time. Finally, the main layer of AlGaN was grown above the mask. The roughness of the samples was estimated by atomic force microscope (AFM) as about 6 nm.

The investigations performed by beam dark field transmission electron microscopy showed that the high number of edge TDs were stopped by the SiN_X interlayer, while the density of screw TDs remained almost unchanged (see Fig. 3.8). However, screw TDs do not hamper the electronic device performance based on AlGaN as strongly as edge TDs [102], so the presence of SiN_X mask made real improvement of the material. From TEM image in Fig. 3.8 we can observe the regions with dislocation bundles yielding large defect- free areas in the film. TDs reaches the surface rather in the form of bundles then separately that leads to decrease of their averaged density.

4. Basics of X-ray Scattering

The x-ray scattering is one of the most important methods for characterization of thin films and nanostructures. By means of the x-ray scattering, the structure of thin films, morphology, strain in the material, electron density and many other properties can be determined. The x-rays can differently interact with matter, they can be absorbed and elastically or inelastically scattered. In this chapter, we will focus on the basic principles of elastic x-ray scattering.

4.1 X-ray diffraction

The wavelength of the x-rays is of order 10^{-9}-10^{-10}m that corresponds to dimensions of atomic plane interspacing in the crystals. It gives rise to examine the crystalline structure by use of x-rays [103, 104]. In this work, we consider the x-rays to be elastically scattered from the solid structure i.e. the wavelengths of the incidence and outgoing beams are equal.

4.1.1 Interaction of x-rays with the crystalline material

The incoming x-ray beam can be absorbed by material resulting with the weaker outgoing beam. This process is described by exponential reduction of incident intensity I_0 while propagating through the sample with the thickness z:

$$I(z) = I_0 \exp(-\mu z), \tag{4.1}$$

where μ is absorption coefficient of the sample material at certain energy of x-rays.

Except being absorbed the incoming beam can be refracted or reflected. Every material possesses its own refractive index. For x-rays the complex refractive index is less then unity and it can presented as follows: $n = 1 - \delta + i\beta$, where δ and β are related to the electron density and to the absorption of material respectively. X-rays can undergo total external reflection if the incident angle is smaller than the critical one given as $\alpha_c = \sqrt{2\delta}$ that is often used in surface and near-surface regions investigation.

Finally, the incident x-ray beam can be diffracted from ordered crystalline structure. In general, diffraction of X-rays from a crystal lattice obeys the Bragg's Law:

$$n\lambda = 2d \sin\Theta, \tag{4.2}$$

where λ is the wavelength, d is the lattice spacing, Θ is the Bragg angle and n means integer.

4.1.2 Classification of scattering approaches

There are two general approaches to describe the x-ray diffraction, namely the dynamical and kinematical scattering theories [105]. Dynamical theory can be applied to highly prefect semi-infinite single crystal systems evolving the narrow Bragg peaks. It takes into account multiple scattering processes. The exact theoretical treatment of x-ray diffuse scattering from GaN epitaxial layers within the dynamical theory is practically impossible.

The kinematical approach known as the first Born approximation is successfully applied to describe the diffraction from rather imperfect systems and small scattering volumes. In the processes described by kinematical diffraction, scattering is supposed to be weak what implies that multiple scattering effects can be neglected. The kinematical x-diffraction can be observed when the diffraction vector $\boldsymbol{Q}$ is close to the reciprocal lattice point so the Bragg condition is fulfilled. Its magnitude can be thus written as follows:

$$|Q| = \frac{4\pi}{\lambda}\Theta, \tag{4.3}$$

From a classical point of view, a charged free electron is accelerated by the incoming electromagnetic wave with the amplitude $E_o \exp(i\boldsymbol{K_i r})$. The resulting forced oscillation of the electron leads to reemission of an electromagnetic spherical wave, which has the same frequency as the original incoming wave and exhibits a characteristic dipole-like angular distribution. At large distance R of the electron from the observer, the electric far field of the scattered wave is given by

$$E(r, R) = r_0 C E_0 \exp(i\boldsymbol{K_i r})\frac{\exp(iKR)}{R}, \tag{4.4}$$

where r_0 is the classical electron radius, K_i is the incidence wave vector and C is the polarization factor having 1 or $|2\cos\Theta|$ values for s- and p-polarizations respectively. $K = |\boldsymbol{K_i}|$ is defined as a length of the wave vector that is constant for incidence and diffracted beams within the kinematical approximation.

The total scattered amplitude is given by a coherent summation over all scattered partial waves:

$$E(\boldsymbol{R}) = r_0 C E_0 \int \rho(r) \exp(i\boldsymbol{K_i r})\frac{\exp(iK|\boldsymbol{r}-\boldsymbol{R}|)}{\boldsymbol{r}-\boldsymbol{R}} dV, \tag{4.5}$$

where $\rho(r)$ stands for the electron density in the material. The integration is performed over the coherently illuminated volume. The expression in the right hand side of the Eq. 4.5 can be simplified when the appropriate approximation is used.

A rough qualitative rule connects the use of the kinematical approximation with at least one of the following conditions [103]:

- the length of the x-ray trajectory in the sample is sufficiently small;
- the layer is highly disturbed;
- the angular deviation of the primary x-ray beam from the direction of the diffraction maximum is sufficiently large.

In some cases the experimental problem cannot be solved neither dynamically nor kinematically, so other suitable approximation should be found. Within semi-kinematical approach the scattering from an undisturbed sample is assumed to be dynamical, while the contribution of the disturbance is calculated kinematically.

4.1.3 Fraunhofer approximation

If the distance between the sample and detector is much larger than the diameter of the coherently illuminated sample area ($|\boldsymbol{R}| \gg |\boldsymbol{r}|$), the Fraunhofer approximation known as far-field diffraction is valid. Another words the square of the size D of scattering object is much smaller then product of the x-rays wavelength λ and R ($D \ll \sqrt{\lambda R}$).

In this case Eq. 4.5 can be rewritten as

$$E(\boldsymbol{Q}) = r_0 C E_0 \frac{\exp(ikR)}{R} \int \rho \boldsymbol{r} \exp(i\boldsymbol{Q} \cdot \boldsymbol{r}) dV \tag{4.6}$$

Here, $\boldsymbol{Q}$ is the scattering vector defined as a difference between wave vectors of the diffracted and incidence beams:

$$\boldsymbol{Q} = \boldsymbol{K_f} - \boldsymbol{K_i}, \tag{4.7}$$

and the phase difference between the scattered on two electrons waves is equal to $\boldsymbol{Q} \cdot \boldsymbol{r}$. The scattering vector can be complex. In this case its real part is connected with refraction and the imaginary part describes absorption. However, since relative changes of scattered intensity are probed in just a small area of reciprocal space, absorption can usually be neglected as long as the photon energy is not chosen close to an absorption edge.

If one neglects the prefactor in front of the integral in 4.6, the amplitude can be treated as the three-dimensional Fourier transform of the electron density $\rho(\boldsymbol{r})$.

The result of the Fraunhofer approximation is that the scattering object is treated as a pointlike source that emits a spherical wave front $\exp(iKr)/R$, which is modulated by $\int \rho \boldsymbol{r} \exp(i\boldsymbol{Q} \cdot \boldsymbol{r}) dV$ amplitude, which is non-zero when the Bragg condition 4.3 is fulfilled. The diffracted wave is treated as a plane wave with the wave vector $\boldsymbol{K_f}$ determined by the position $\boldsymbol{R}$ of the detector [105].

4.1.4 The resolution elements in reciprocal space

The divergences of the incidence and the scattered beam yield the certain distribution of different scattering signals that are summed up to the total intensity. In order to describe this effect properly the scattering intensity has to be averaged over the resolution element. The resolution element is called an area in reciprocal space that is illuminated by the incident beam and at the same moment accepted by the detector under geometrical and spectral conditions of the scattering experiment [103]. Its shape depends on the geometrical conditions of the x-ray experiment. For coplanar diffraction in the $Q_x Q_z$-plane the resolution element can be expressed as

$$A_{coplanar} = \Delta Q_z \Delta Q_x, \tag{4.8}$$

where ΔQ_z and ΔQ_x depend on the wavevector amplitude K, incidence and exit angles $\alpha_{i,f}$ and the divergences of the incident and diffracted beams $\Delta_{i,f}$

$$\begin{aligned} \Delta Q_x &\approx K \sqrt{(\Delta\alpha_i \sin\alpha_i)^2 + (\Delta\alpha_f \sin\alpha_f)^2}, \\ \Delta Q_z &\approx K \sqrt{(\Delta\alpha_i \cos\alpha_i)^2 + (\Delta\alpha_f \cos\alpha_f)^2}, \end{aligned} \tag{4.9}$$

In grazing-incidence diffraction with $Q_{ang}Q_{rad}$ plane of diffraction the resolution element is introduced as

$$A_{GID} = \Delta Q_{ang} \Delta Q_{rad}, \tag{4.10}$$

where

$$\begin{aligned} \Delta Q_{ang} &\approx K\sqrt{\sin^2\Theta_B\left[\alpha_f^2(\Delta\alpha_f)^2 + \alpha_i^2(\Delta\alpha_i)^2\right] + \cos^2\Theta_B\left[(\Delta\Theta_f)^2 + (\Delta\Theta_i)^2\right]}, \\ \Delta Q_{rad} &\approx K\sqrt{(\Delta\alpha_f)^2 + (\Delta\alpha_i)^2}, \end{aligned} \tag{4.11}$$

where $\Delta\Theta_{i,f}$ are the in-plane Bragg angles between the lateral projection of the incident and the scattered beam and the diffraction plane.

In simulations of the diffraction experiment, the incident photon flux should be additionally corrected according to the effective illuminated area. If the incidence angle is α_i, then the calculated intensity should be multiplied by the factor of $1/\sin\alpha_i$.

In our work, we calculate resolution elements for every diffraction experiment based on Eq. 4.1.4 and 4.1.4 and perform the convolution of calculated intensity with the appropriate resolution function that allows us to compare the intensity distributions from x-ray experiment and our calculations.

4.1.5 The intensity of the scattered wave

The x-ray scattering intensity $I(Q)$ is the ratio of intensity scattered by the crystal at large distances to one scattered by classical electron. In the kinematical theory the complex amplitude of scattering is treated as a sum of amplitudes scattered from individual atoms taken with appropriate phase [2]. Then the intensity of high-frequency monochromatic radiation is expressed in electron units as follows:

$$I \propto \left| \int \rho(\boldsymbol{r}) \exp(i\boldsymbol{Q}\cdot\boldsymbol{r}) d\boldsymbol{r} \right|^2 \tag{4.12}$$

The integration in Eq. 4.12 is performed over the entire volume of the crystal.

Let us consider the n-th atom placed in the s-th unit cell occupies the site γ. In imperfect crystals the positions of atoms do not coincide with the sites γ of the perfect lattice and are displaced by some vectors $u_n = u_{s,\gamma}$. In that case the total electron density can be written as

$$\rho(\boldsymbol{r}) = \sum_{n=1}^{N_0} \rho_n(\boldsymbol{r} - \boldsymbol{R_n} - \boldsymbol{u_n}) = \sum_{s=1}^{N}\sum_{\gamma=1}^{\nu} \rho_{s\gamma}(\boldsymbol{r} - \boldsymbol{R_{s\gamma}} - \boldsymbol{u_{s\gamma}}), \tag{4.13}$$

where $N_0 = N\nu$ is the total number of atoms, N is the number of cells in the crystal, ν is the number atoms in one cell, and $\boldsymbol{R_n} = \boldsymbol{R_{s\gamma}}$ is the radius vector of the n-th atom. Substituting Eq. 4.13 into Eq. 4.12 one can obtain:

$$I = \left| \sum_{n=1}^{N_0} f_n e^{i\boldsymbol{Q}\boldsymbol{R_n}} e^{i\boldsymbol{Q}\boldsymbol{u_n}} \right|^2 = \sum_{s=1}^{N}\sum_{\gamma=1}^{\nu} f_s\gamma e^{i\boldsymbol{Q}\boldsymbol{R_{s\gamma}}} e^{i\boldsymbol{Q}\boldsymbol{u_{s\gamma}}} \Big|^2, \tag{4.14}$$

$$f_n = f_{s\gamma} = f_n(\boldsymbol{Q}) = \int \rho_n(r') \exp(i\boldsymbol{Q}\boldsymbol{r'}) d\boldsymbol{r'} \tag{4.15}$$

is the atomic scattering factor of the n-th atom and $\boldsymbol{r'} = \boldsymbol{r} - \boldsymbol{R_n} - \boldsymbol{u_n}$. Eq. 4.14 is valid if the frequency of scattered x-ray is higher that the electron Bohr frequency. In general, the atomic factor is complex:

$$f_n = f_n^0 + f_n' + if"_n \tag{4.16}$$

The item f_n^0 is given by 4.15, the additional real part f_n' is responsible for scattering at the absorption edge and the imaginary part $f"_n$ depends on the absorption coefficients and is determined by the oscillator strength for the electron transitions.

In real imperfect crystals the structure amplitude is determined in different cells for particular distributions of atoms and defect types. Since the scattering volume contains a large number of atoms, the calculate scattering intensity for particular defect distribution almost coincides with the mean scattering intensity for the statistical ensemble for given macroscopic parameters which describe the composition, order and correlation in the crystal. Let us introduce radius vector $\boldsymbol{R_{ss'}} = \boldsymbol{R_s} - \boldsymbol{R_{s'}}$ connecting two distorted unit cells inside the crystal. Then the scattered intensity can be rewritten in the form of general equation of the kinematical theory:

$$I(\boldsymbol{R_{ss'}}, \boldsymbol{Q}) = \frac{1}{n} \sum_s \langle f_s f_{s'}' \exp[i\boldsymbol{Q}(\boldsymbol{u_s} - \boldsymbol{u_{s'}})] \rangle \tag{4.17}$$

The displacement $\boldsymbol{u}$ is the sum of static displacements. The angle brackets in 4.17 denote the averaging performed over the statistical ensemble including the quantum-mechanical one over the vibrations of atoms around their equilibrium positions.

4.1.6 Diffuse x-ray scattering from defects

The intensity scattered diffusely from defect-containing single crystal can be obtained from Eq. 4.17 if one considers individual structure amplitudes f_s and displacements u_s in different cells s [2]. Let a defect occupies the position t with the radius vector $\boldsymbol{R_t}$. For a dislocation, the dislocation line passes through the position t, for a dislocation loop, its center is located at the position t. The displacement vector $\boldsymbol{u_{st}}$ is defined for the center of the s-th lattice cell caused by a defect located at t. This displacement significantly changes the structural factors denoted as ϕ_{st}. This parameter usually decreases more rapidly then $\boldsymbol{u_{st}}$ with increasing distance from the defect position t.

The defect distribution in a crystal is described with the numbers $c_t = 1$, if a defect is in the position t and $c_t = 1$, if the defect is not placed there. These numbers are statistically independent in the case of non-correlated defects distribution and the probability is then equal to defect concentration c. If we consider only one type of defects with identical orientation, then the total displacement in the center of the s-th cell can be regarded as a superposition of the displacements caused by individual defects:

$$\boldsymbol{u_s} = \sum_t c_t \boldsymbol{u_{st}} \tag{4.18}$$

If the defect concentration is low, the structure amplitude for the s-th cell can be represented as:

$$f_s = f + \sum_t c_t \phi_{st}, \tag{4.19}$$

where f is the structural amplitude of the crystal without any defects and the summation is performed over all position t that can be occupied by defects.

Substituting 4.19 into 4.17, we obtain the expression for scattering intensity for given defects distribution in the crystal:

$$I = \sum_{s,s'} \left(f + \sum_t c_t \phi_{st} \right) \left(f' + \sum_{t'} c_{t'} \phi'_{s't'} \right) \exp(i\boldsymbol{Q}\boldsymbol{r}) \times \prod_{t"} \exp(i\boldsymbol{Q}\boldsymbol{u}_{\boldsymbol{ss't"}} c_{t"}), \tag{4.20}$$

where $\boldsymbol{r} = \boldsymbol{R}^0_{\boldsymbol{s}} - \boldsymbol{R}^0_{\boldsymbol{s'}}$ ($\boldsymbol{R}^0_{\boldsymbol{s}}$ stands for radius vector of the center of the s-th cell in the crystal without defects) and $\boldsymbol{u}_{\boldsymbol{ss't}} = \boldsymbol{u}_{\boldsymbol{st}} - \boldsymbol{u}_{\boldsymbol{s't}}$.

When the defect concentration c is small so they do not affect the structure amplitudes and $\phi_{st} = 0$, the averaging over the random variables c_t yields:

$$I = |f|^2 \sum_{s,s'} \exp(i\boldsymbol{Q}\boldsymbol{r}) \exp(-T), \tag{4.21}$$

where

$$T = c \sum_t [1 - \exp(i\boldsymbol{Q}\boldsymbol{u}_{\boldsymbol{ss't}})] \tag{4.22}$$

The same approach applied in the case of several defect types α that produce non-zero change in structural amplitude ϕ_{st}, gives rise to additional summation over α in 4.21and 4.22 and leads to the similar expression for the scattering intensity:

$$I = \sum_{s,s'} e^{i\boldsymbol{Q}\boldsymbol{r}} \left(|\bar{f}|^2 + \sum_\alpha c_\alpha \sum_t \phi_{st\alpha} \phi'_{s't\alpha} e^{i\boldsymbol{Q}\boldsymbol{u}_{ss't\alpha}} \right) e^{-T}, \tag{4.23}$$

where

$$T = \sum_\alpha c_\alpha \sum_t [1 - \exp(i\boldsymbol{Q}\boldsymbol{u}_{ss't\alpha})] \left[1 + \frac{1}{f} (\phi_{st\alpha} + \phi'_{s't\alpha}) \right] \tag{4.24}$$

and

$$\bar{f} = f + \sum_\alpha c_\alpha \sum_t \phi_{st\alpha} \tag{4.25}$$

. Eq. 4.23 is written as a sum of two terms, the first of which is proportional to a delta function in the limit of the infinite periodic lattice, whereas the second one does not contain any delta functions. Thus the first term leads to the sharp Bragg peaks appearing in the intensity distribution in reciprocal space. The sharp specular scattering is the Bragg scattering contains the information about the average sample structure. Any perturbation of the exact periodicity of the atomic lattice produces the diffuse scattering in the vicinity of the Bragg peaks, describing by the second term in 4.23. Except of crystallographic defects, the factors giving rise to diffuse scattering can be thermal vibration of the atoms, surface roughness etc. They additionally affect the position of Bragg peak and decrease its intensity [105].

5. Defects Determination

5.1 Direct methods

In this section, we make a brief review of the most common direct methods enabling to investigate the defect structure of materials. Electron microscopy, cathodoluminescence and technique based on etching belong to the most often used direct methods of defect determination. The main advantage of direct methods is relative simplicity of output data bearing the information about the defects. These data can be analysed without special mathematical transformations and simulations. However, the samples require special time consuming preparations for experiment and they can be damaged or destroyed during it.

5.1.1 Transmission electron microscopy

Transmission electron microscopy (TEM) is a microscopy technique that is characterized by a beam of electrons transmitted through ultra thin specimen and by an image obtained as a result of interaction between the electron beam and the specimen [106–108]. A magnified image can be focused onto a fluorescent screen, a layer of photographic film, or a detector equipped with a charge-coupled device (CCD) camera. The first Transmission electron microscope was built by Max Knoll and Ernst Ruska in 1931. Since that time it has be significantly modified, nevertheless its principal components such as vacuum system, specimen stage, electron gun, lenses and apertures remained unchanged. The scheme of modern TEM is shown in Fig. 5.1. Electrons are usually emitted in the electron microscope by means of thermionic emission from a tungsten filament. Then they are accelerated by a high potential difference and focus on the thin sample by electromagnetic lenses. The beam passed through the specimen contains information about the electron density, phase and periodicity and it forms an image. The detailed review of the TEM electron source and optics can be found elsewhere [109, 110].

Theoretically, the maximum resolution in the optical microscope is limited by the wavelength of the photons λ probing the sample and the numerical aperture N_A of the optical system:

$$d = \frac{\lambda}{2n \sin \alpha} \approx \frac{\lambda}{2N_A}. \tag{5.1}$$

The concept of de Broglie waves reflects the wave–particle duality of matter and enables to consider an electron as a particle with the wavelength

$$\lambda = \frac{h}{p}, \tag{5.2}$$

where h is Planck's constant and p is relativistic momentum of the electron [111]. The electron wavelength in TEM should be corrected for relativistic effects, since electrons moves with the velocities close to speed of light c in it. Taking into

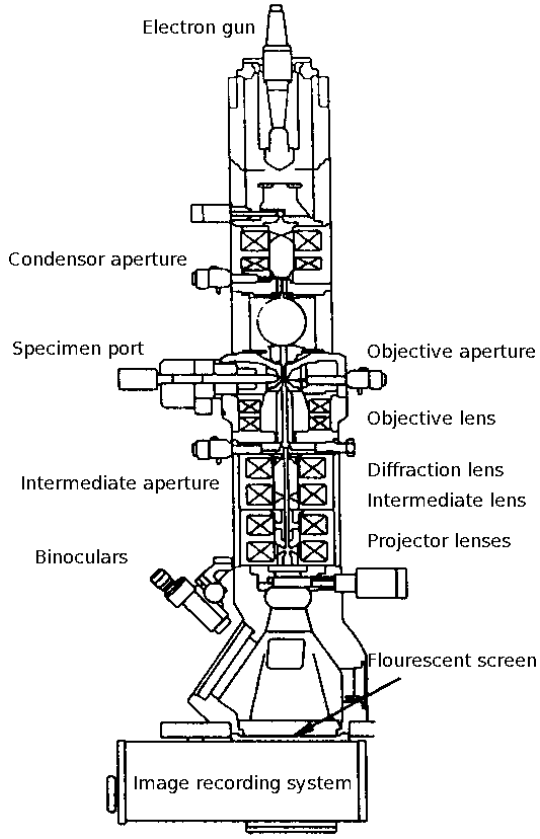

Figure 5.1: The scheme of a transmission electron microscope taken from Wikipedia.

account that $p = \frac{h}{\sqrt{2m_0eU}}$, it yields.

$$\lambda_e = \frac{h}{\sqrt{2m_0eU}} \frac{1}{\sqrt{1 + \frac{eU}{2m_0c^2}}}, \tag{5.3}$$

where m_0 is is the rest mass of an electron, e is its electrical charge, and U is an electric potential used for electron acceleration. The typical wavelength of the electrons in TEM of order 10^{-3} nm corresponds to electron energies from few tens to several hundreds keV that is by two order less than usual x-ray wavelength.

Two types of electron microscopy are distinguished, bright field and dark field microscopies namely. Bright field microscopy uses transmitted and scattered beams to form a picture. The contrast is caused by absorbance of some of the transmitted light in dense areas of the specimen resulting in dark sample image on a bright background. Dark field microscopy describes microscopy methods, which exclude the unscattered beam from the image. As a result, the field around the specimen is generally dark.

Sample preparation in TEM can be a complex procedure. The thickness of a specimen is required to be comparable to the mean free path of the electrons passing through it (usually a few tens of nanometers). Mechanical polishing is often used to prepare single crystal samples. It ensures constant sample thickness across the region of interest and removes any surface scratches that may cause contrast fluctuations. Ion etching can be used as a final polishing to achieve the better sample characteristics. It consists in a sputtering with a plasma stream generated from an inert gas passed through an electric field. Recently focused

ion beam methods have been used to prepare samples [112]. Chemical etching is a powerful technique to perform qualitative and quantitative analyses that will be discussed in the next section.

The study of crystallographic defects can be based on the diffraction contrast in TEM [113]. The periodic lattice of a crystalline solid acts as a diffraction grating, scattering the electrons in a predictable way. The contrast is observed when the electron beam undergoes Bragg condition, in which electrons are dispersed into discrete locations in the back focal plane. The specimen holder brings the sample to diffraction condition and the objective aperture allows to choose the appropriate Bragg angles to probe the defects. Due to small wavelength of electrons, the radius of the Ewald sphere is large that results in larger accessible area of crystal in reciprocal space than in x-ray diffraction experiments. In a TEM, a single crystal grain or nanometer size particles may be selected for the diffraction experiments. However, electron diffraction is often regarded as a qualitative technique. It reveals information about deviations from crystalline symmetry, whereas the defect densities can not be obtained directly from diffracted patterns. Another limitation of electron diffraction in TEM is the comparatively high level of user interaction needed for the data analysis.

High-resolution transmission electron microscopy (HRTEM) is an imaging mode of the transmission electron microscope that allows the investigation of the crystallographic structure of a sample at an atomic scale. The typical resolution of HRTEM images is about 0.1 nm so the crystalline defects can be directly seen. The basic principle of HRTEM is the following. A very thin slice of crystal

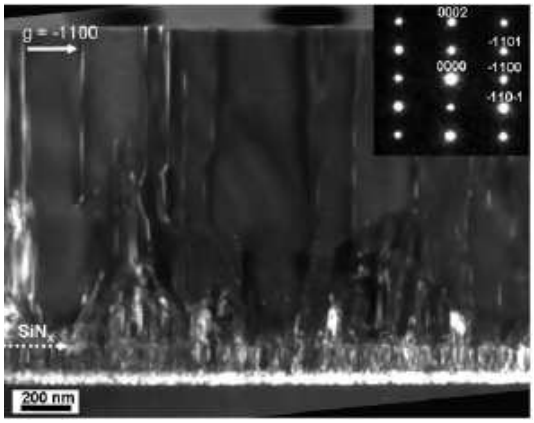

Figure 5.2: HRTEM cross-section of the AlGaN sample in $\bar{1}100$ electron diffraction taken from [114]. The inset shows the coordinates of different reciprocal space reflexes.

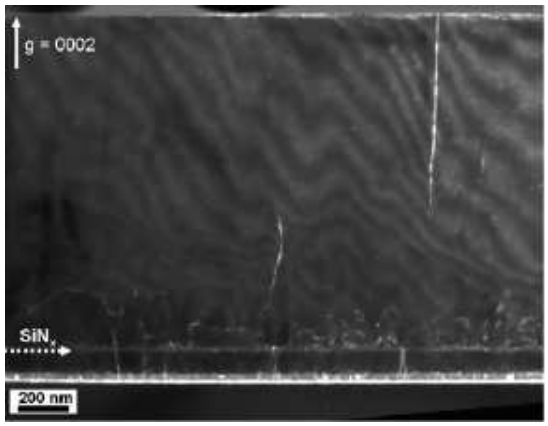

Figure 5.3: HRTEM cross-section of the AlGaN sample in 0002 electron diffraction taken from [114].

prepared in advance is placed perpendicular to the electron beam. All planes close to Bragg position will diffract the primary beam. The diffraction pattern is the Fourier transform of the periodic potential for the electrons in two dimensions. In the objective lens all diffracted beams and the primary beam are brought together again. Their interference provides a back-transformation and leads to an enlarged picture of the periodic potential. The magnified final pattern with diffraction contrast is projected onto the screen or recording device [115].

The one- or two-dimensional defects in crystalline material are characterized by Burgers vectors in case of dislocations or displacement vectors that are normal to stacking faults. For elastically isotropic medium the criterion of defect invisibility in TEM can be written as

$$\boldsymbol{g} \cdot \boldsymbol{b} = n, \tag{5.4}$$

where $\boldsymbol{g}$ is the vector of electron diffraction, $\boldsymbol{b}$ refers to dislocation Burgers vector or stacking fault displacement vector and n is integer. In anisotropic medium the equation 5.4 based on diffraction contrast distribution is not still valid and it has to be modified as it is discussed in [116].

A good example of appropriate diffraction selection to visualize screw and edge threading dislocation in c-plane AlGaN epitaxial layers can be found in [101, 114]. Here, cross-sectional weak-beam dark-field HRTEM studies are carried out to describe a growth model of $AL_{0.2}Ga_{0.8}N$ films with a SiN_X nano-mask. The edge dislocations with Burgers vectors $\boldsymbol{b}_e = \frac{1}{3}\langle 11\bar{2}0\rangle$ are mostly stopped by SiN_X mask (see Fig. 5.2). The TDs passing through the mask in some regions are merged or bent, creating bundles of dislocations, hence reaching the surface rarely separately. The density of edge dislocations below the SiN_X is several time higher than above it. As for screw threading dislocations with Burgers vectors $\boldsymbol{b}_s = \langle 0001\rangle$ (shown in Fig. 5.3), their number is very small and the deposited nano-mask has almost no influence on their propagation over the sample thickness. On both figures, a sub-monolayer SiN_X mask is clearly seen, which proves extremely high sensitivity of XRTEM method. The appropriate choice of $\boldsymbol{g}$ enables to probe screw and edge dislocation separately. Nonpolar a-plane GaN

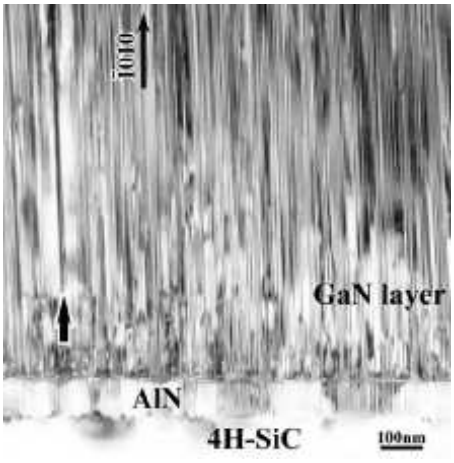

Figure 5.4: Cross-sectional HRTEM dark field image with $\boldsymbol{g} = \bar{1}010$ taken from [31]. The BSFs are stretched in vertical direction.

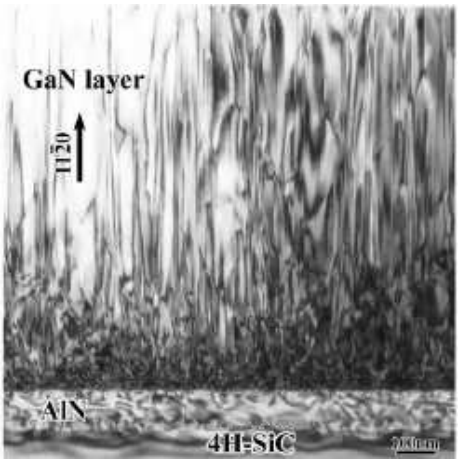

Figure 5.5: Cross-sectional HRTEM bright field image with $\boldsymbol{g} = 11\bar{2}0$ from [31] measured close to the [0001] zone axis. The PSFs are visible as thin lines coming to the sample surface at a 60^o angle.

was examined by bright and dark field TEM methods in [31]. The samples under study were grown by organometallic vapor phase epitaxy on $(11\bar{2}0)$ $4H$-SiC. AlN

nucleation layer was deposited to decrease substrate/film mismatch. The cross-sectional TEM in Fig 5.4 reveals basal stacking faults with $\frac{1}{6}\langle 20\bar{2}3\rangle$ displacement vectors nucleate at the 4H-SiC/AlN interface and propagate through the GaN to the sample surface. A crack formed approximately 100 nm from the AlN buffer layer is marked by an arrow. Selecting the diffraction vector as $\boldsymbol{g} = 11\bar{2}0$, one can observe the prismatic stacking located in $(\bar{2}110)$ and $(1\bar{2}10)$ planes (presented in Fig. 5.5). The use of HRTEM technique provided an excellent visual information about the two-dimensional defects typically present in a-plane GaN material.

Summarizing, a great advantage of the TEM consists in the capability to observe, by adjusting the electron lenses, both electron microscope images and diffraction patterns for the same region. It is a powerful technique to obtain a precise qualitative description of the object under study. On the other hand, for certain applications this method is limited by rather small size of the area covered by electron beam. Moreover, the prepared slice-like specimens might not always represent the features of the entire sample.

5.1.2 Etch pit density

The etch pit density (EPD) is a technique to study the defect structure of the crystalline material. In this technique, an etch solution is applied on the surface of the crystal. The etch rate is increased at crystallographic defects resulting in etch pits, which density can be counted in optical contrast or electron microscope [117].

The EPD methods is mostly used for determination of dislocation densities. The formation of etch pits in regions where the dislocations reach the surface is connected to the fact that the region of the crystal lattice near the dislocation has the excess of energy so the atoms can be easily removed from the surface at these sites. Another words, EPD is based on the differences in chemical dissolution rate between an undisturbed crystal material and a lattice place with a defect. Different shapes of pits are observed in different crystallographic planes. For example, (111) planes correspond to the pits in the form of equilateral triangles, (110) planes - in the form of squares. It can be explained that, since various crystal planes have different surface energies, they yield different etching rates [118].

In order to determine the density of dislocations, the surface of the sample is explored in two perpendicular directions. For this reason an eyepiece with a coordinate grid is used. The image is divided into several equal squares and one counts the average number of etch pits i in these squares. The dislocation density is calculated as follows:

$$\rho = \frac{iM^2}{S}, \tag{5.5}$$

where M is magnification and S is area of one square.

In EPD, both optimized etching conditions for revealing all defects and interpretation of the meaning of the etch features have to be established. Weyher et al. applied a combination of etching and TEM analysis to determine the density of threading dislocation in HVPE-grown c-plane GaN [119]. They found the temperature dependence of different types of dislocations visibility and optimized the etching conditions to the kinetic processes within the samples under study.

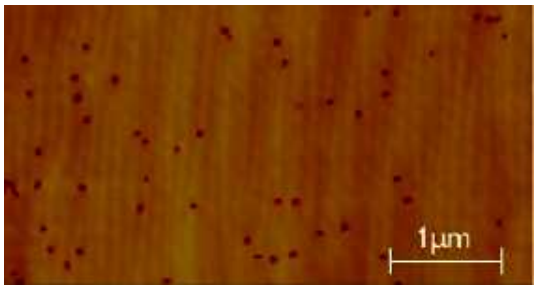

Figure 5.6: EPD image of the sample S4 taken from [57]. The total density of threading dislocations is estimated as $2.6 \times 10^8 cm^{-2}$.

Using TEM on specimens prepared by conventional cross-section and cut by focused ion beam methods, it was unequivocally established that the largest pits are formed on screw-type dislocations, intermediate size pits on mixed-type dislocations and the smallest ones on edge-type dislocations.

Kamler et al. used a method of defect-selective etching for MOVPE-grown polar GaN films [120]. After etching, the samples were studied by differential interference contrast optical microscopy, transmission and scanning electron microscopies. Except determination of dislocation densities this method revealed the indentation-induced dislocations in the GaN single crystals and the presence of nano-pipes of density one to two orders of magnitude lower than the density of dislocations.

The series of GaN samples described in Sec. 3.3.1 were investigated by EPD method. Small slices of each GaN sample were etched and explored with SEM. The surface of the sample S1 with etch pits is shown in Figure 5.6. These measurements allowed us to determine the total density of TDs, nevertheless screw and edge dislocations were hard to distinguish.

The examples listed above confirms a huge importance of the etching methods in GaN structural study. The EPD technique has high enough accuracy to determine the total density of dislocations. It belongs to the most cheapest and time-effective methods. However, the etch pits of screw and edge threading dislocations can not always be easily distinguished. EPD measurements tend to underestimate the dislocation density if it is higher than 5×10^6 cm^{-2} [121].In addition, the main weakness of EPD is destruction of samples due to non-returnable chemical processes during the etching.

5.1.3 Cathodoluminescence

The cathodoluminescence (CL) is a method to study a direct band gap semiconductor materials like the III-nitrides. It is based on interaction of the electron beam generated by an electron gun with the semiconductor. CL wavelength and intensity are dependent on the characteristics of the sample and on the working conditions of the electron gun [122]. This interaction gives rise to electron-hole pairs generation within the sample. The density of these pairs is limited by the scattering process of the electron beam within the sample. Their distribution depends on the diffusion length and the recombination behaviour at the surface and in the bulk. The recombination can be either radiative in which case a photon is emitted or non-radiative generating phonons or Auger electrons. In general, the radiative and the non-radiative processes can not be separated quantitatively. CL photons are generated by electronic transitions between the conduction and the valence bands and due to impurities or defects located in the energy gap.

The generated photons can be collected and subsequently detected to provide the cathodoluminescence signal [123].

Mapping of cathodoluminescence in crystalline material shows enhanced intensity in the vicinities of dislocations due to localised gettering effects [124]. Another application of CL is cathodoluminescence spectroscopy. The luminescence spectra are obtain if the electron beam is hold stationary or it scan small area of the specimen.

In general, the CL methods enables the quantitative determination of many electronic and optical parameters of materials. Besides the density of defects it is possible to measure its distribution, the diffusion length, absorption coefficient, doping levels, defects recombination velocity or energy levels.

The threading dislocations in polar GaN act as non-radiative recombination centres [21]. This property of TDs give an opportunity of their direct imaging by the cathodoluminescence mapping. The so-called dark spot counting is based on the fact that the strain field around a dislocation can trap carriers and thus act as a recombination centre at which the luminescence intensity is drastically reduced [125]. This method enables to distinguish between threading and misfit dislocations. The first ones appears on the micrograms as dots, whereas the misfit dislocations give rise to lines [126].

The examples of CL investigations of GaN are published in many papers [127–129]. Typical CL maps and spectra can be found there as well.

The CL technique avoids destruction of the sample and possesses high accuracy. It demonstrates reliable densities of dislocations below 10^6 cm^{-2}, where TEM investigations are not sensitive.

5.2 X-ray based methods

The x-ray investigations provide complete information about the defect structure of crystalline materials under study. A large number of methods exists to characterize defects qualitatively and quantitatively. The detailed theory of x-ray diffraction and its connection to crystal imperfectnesses can be found in Sec. 4. Here, we make an overview of the most commonly used methods for defects density determination in III-nitrides.

5.2.1 Peak broadening and FWHM analysis

The triple-axis x-ray diffractometry is a powerful technique for linear defects study. Selecting the appropriate reflex x-ray diffraction is a suitable method for separation of edge and screw dislocations.

Metzger et al. used the broadening of diffraction curves for screw and edge TDs density determination in polar GaN layers grown by metallorganic chemical vapour deposition [24]. Their results were compared to transmission electron microscopy measurements. The TDs are considered within a grain boundary model which generally means the screw dislocation refer to the tilt grains and edge ones refer to their twist [130, 131]. The mosaic structure of GaN films within this model is usually described with four parameters: tilt angle α_Ω, twist angle α_Φ, mean out-of-plane grain size or vertical coherence length $L_\perp$ and mean

in-plane grain size or lateral coherence length $L_\parallel$ [132, 133]. The reciprocal lattice point is broadened along a specific direction by the mosaic parameters.

The rocking curves measured in symmetrical $000n$ x-ray diffraction were assumed possessing either Gaussian or Lorentzian peak shapes that led to different ways of TDs density calculation. The instrumental broadening estimated as few arcsec was neglected in the model. In general the measured x-ray profiles were fitted by a pseudo-Voigt function with the parameter $0 \leq \eta \leq 1$. The limit values $\eta = 0$ and $\eta = 1$ correspond to Gaussian and Lorentzian peak shape approximations respectively. Determining the parameter η by a least square fit and knowing the full width at half maximum (FWHM) β_Ω, one can calculate the tilt angle α_Ω [132]:

$$\alpha_\Omega = \beta_\Omega \left[0.184446 + 0.812692(1 - 0.998497\eta)^{1/2} - 0.659603\eta + 0.44554\eta^2\right], \tag{5.6}$$

Then the density of randomly distributed screw dislocations can be calculated by equation of Gay at al., modified by Dunn and Koch [134]:

$$\rho_s = \frac{\alpha_\Omega^2}{4.35\boldsymbol{b}_s^2}, \tag{5.7}$$

where $\boldsymbol{b}_s$ is the Burgers vector of the screw TD.

Edge TDs are related to an azimuthal rotation of crystallites around the surface normal. Similar to Eq. 5.7 the density of randomly distributed edge dislocations with the Burgers vector $\boldsymbol{b}_e$ can be presented as

$$\rho_e = \frac{\alpha_\Phi^2}{4.35\boldsymbol{b}_e^2}, \tag{5.8}$$

The twist angle α_Φ can be measured by performing Φ-scans in asymmetrical reflections, where the sample is rotated with respect to the surface normal.

If dislocations are piled up in small angle grain boundaries the Eq. 5.8 should be modified:

$$\rho_e = \frac{\alpha_\Phi}{2.1|\boldsymbol{b}_e|L_\parallel}. \tag{5.9}$$

$$L_\parallel = \frac{0.9\lambda}{\beta_\Omega(0.017475 + 1.500484\eta - 0.534156\eta^2)\sin\Theta}. \tag{5.10}$$

In Eq. 5.9 and 5.10 λ is the wavelength, and Θ is the Bragg angle of reflection.

The broadening of the diffraction curves in the radial direction due to strain field around each dislocation can also characterize separately the densities of screw and edge TDs.

$$\rho_{s,e} = \frac{1}{4r_{s,e}}, \tag{5.11}$$

where $r_{s,e}$ is the upper integration limit of the strain field, which is connected to the peak broadening [135]. Using Eq. 5.11 the strain broadening of asymmetrical reflections from different number of screw and edge TDs were simulated and compared with the measured values.

Finally, Metzger et al. determined separately densities of two types of TDs and both correlation lengths. The values obtained from TEM, pseudo-Voigt fits and strained broadening were compared and it was found they were in a good agreement.

Ayers calculated the densities of threading dislocations from rocking curve measurements of (001) zinc-blende GaAs epitaxially grown on Si (001) [121]. The x-ray curves in his work were assumed to be Gaussian in shape. It was considered three main contributions to the broadening of the diffraction curves caused by TDs:

- an angular rotation at the dislocation β_α;
- a strain field surrounded the dislocation β_ϵ;
- the walls between the small polycrystals (if the sample is not a single crystal).

Within a mosaics model the broadening in symmetrical diffraction due to rotation is related to screw TDs density:

$$\rho_s \approx \frac{\beta_\alpha^2}{4.36} \tag{5.12}$$

The strain component in the symmetrical case for screw and 60-degree edge TDs is given by the following equations:

$$\begin{aligned} \beta_{\epsilon s}^2 &= 0.09 b_s^2 N_s |\ln(2 \times 10^{-7} \sqrt{N_s})| \tan^2 \Theta \\ \beta_{\epsilon e}^2 &= 0.16 b_e^2 N_s |\ln(2 \times 10^{-7} \sqrt{N_e})| \tan^2 \Theta. \end{aligned} \tag{5.13}$$

In asymmetrical reflections these equations may be applied with less then 20% error.

The FWHM of the measured hkl rocking curve β_m includes these contributions as well as instrumental broadening β_d, intrinsic rocking curve width of the crystal β_0 and correction due to the crystal size β_L and curvature β_r:

$$\beta_m^2 = \beta_0^2 + \beta_d^2 + \beta_\alpha^2 + \beta_\epsilon^2 + \beta_L^2 + \beta_r^2 \tag{5.14}$$

The last two items here are negligible for deposited layers thicker than 1 μm. Then the part of broadening that corresponds to defect presence is

$$\beta_{adj}^2 = \beta_m^2 - \beta_0^2 + \beta_d^2 \approx K_\alpha + K_\epsilon \tan^2 \Theta. \tag{5.15}$$

If one measures rocking curve FWHMs for three or more diffractions and plots β_{adj}^2 versus $\tan^2 \Theta$ known as Williamson-Hall plot [136], the result should be a straight line with intercept K_α and slope K_ϵ. Then the densities of screw dislocation due to angular and strain broadening are:

$$\begin{aligned} \rho_s &= \frac{K_\alpha}{4.36 b_s^2}, \\ \rho_s &= \frac{K_\epsilon}{0.09 b_e^2 |\ln(2 \times 10^{-7} \sqrt{N_s})|} \end{aligned} \tag{5.16}$$

The expressions listed above allowed Ayers to determine separately densities of edge ans screw TDs and attribute them to grains rotation or strain distribution.

Nevertheless the methods based on analysing of peak profiles width have a few drawbacks. The peak shapes are assumed to be Gaussian or Lorentzian that is not true. The FWHM characteristic does not bear sufficient information about dislocation density that yields low accuracy of the methods, which operate this parameter.

5.2.2 Microdistortion tensor analysis

The dislocation structure of thick c-plane HVPE GaN layers can be studied by analysis of the microdistortion tensor components. This method was proposed by Kyutt, Ratnikov et al. in the end of the 20-th century [137, 138]. The sample is suggested to measure in symmetrical Laue and Bragg diffraction geometries in order to obtain the tensor components.

The TDs in highly mismatched heteroepitaxial layers cause the displacement field, which components are of high interest. The root mean square deviations of nondiagonal components $\langle\epsilon_{zx}\rangle$ and $\langle\epsilon_{xy}\rangle$ of the microdistortion tensor $\langle\epsilon_{ij}\rangle$ determine the misorientation of diffracting planes and the axis rotation in the xy plane respectively. If the crystal is supposed to consist of misoriented blocks tilted and twisted respective to each other, the densities of pure screw and edge TDs can be explicitly linked to the tensor components as follows:

$$\begin{aligned} \rho_s &= \langle\epsilon_{zx}\rangle^2 / 0.86\boldsymbol{b}_s^2, \\ \rho_e &= \langle\epsilon_{xy}\rangle^2 / 0.86\boldsymbol{b}_e^2. \end{aligned} \tag{5.17}$$

If one considers edge dislocation that form the low-angle boundaries [139] with τ_x distance between boundaries, the density of edge threading dislocations is given by expression:

$$\rho_{eb} = \langle\epsilon_{xy}\rangle^2 / (|\boldsymbol{b}_e|\tau_x). \tag{5.18}$$

The $\langle\epsilon_{xy}\rangle$ component can be directly determined from grazing-incidence diffraction, however, the authors of this approach suggested to use the Laue geometry instead. This choice was based on gradually decreasing density of TDs toward the surface in HVPE GaN material, while GID probes only thin (less than 100 nm) top layer of the sample. In each Bragg and Laue geometries rocking curve (Θ scan) and radial ($\Theta - 2\Theta$) scan have to be measured.

It was found that the broadening of the Bragg Θ-rocking curves reveal nondiagonal $\langle\epsilon_{zx}\rangle$ component of tensor and the coherent scattering size in direction normal to the interface τ_z, whereas the $\Theta - 2\Theta$-curves give $\langle\epsilon_{zz}\rangle$ and the coherent scattering size in direction parallel to the interface τ_x. In Laue geometry the Θ-scans contain information about $\Theta - 2\Theta$-curve gives $\langle\epsilon_{xz}\rangle$ and τ_z, while radial scans give $\langle\epsilon_{xx}\rangle$ and τ_x. The GID measurements bear the twist information related to $\langle\epsilon_{xy}\rangle$ component.

The value of $\langle\epsilon_{zx}\rangle$ necessary for screw dislocations density determination can be mathematically extracted from measured curve analysis. In the case of edge dislocation, Ratnikov et al. discussed and confirmed the validity to use the difference $\langle\epsilon_{xx}\rangle - \langle\epsilon_{zz}\rangle$ instead of $\langle\epsilon_{xy}\rangle$ [138]. The similar approach allows to estimate the density of misfit dislocations taking into account their screw or edge nature.

The densities of screw and edge TDs averaged over the layer thickness were obtained by technique mentioned in this section. In our opinion, this method suits for thick HVPE GaN films, whereas for thinner films its application encounters difficulties to perform measurements with different setups (especially Laue geometry) and to handle tensor quantities. The conventional asymmetrical and, of course, GID measurements possess higher precision and require less time to evaluate the results.

5.2.3 Krivoglaz theory modified by Kaganer

The theories based on FWHM of the diffraction peak analyses own low accuracy. The peak broadening refers not only to the density of dislocations but also to the correlation between them. Kaganer et al suggested to analyse the entire line shape of the diffracted profiles and particularly their tails [3]. The tails are hardly affected by the correlation between dislocations. Therefore they follow universal power laws that can be used to obtain the density of dislocations.

The intensity of x-ray scattering from a crystal disturbed by distortion fields of lattice defects is described by well-known Krivoglaz theory as Fourier transform of the correlation function $G(\boldsymbol{r})$ [2]:

$$I(\boldsymbol{q}) = \int G(\boldsymbol{r}) \exp(i\boldsymbol{q} \cdot \boldsymbol{r}) d\boldsymbol{r}. \tag{5.19}$$

The correlation function is in general the following:

$$G(\boldsymbol{r}) = \langle \exp\{i\boldsymbol{Q} \cdot [\boldsymbol{U}(\boldsymbol{r}) - \boldsymbol{U}(0)]\} \rangle, \tag{5.20}$$

where $\boldsymbol{Q}$ is the scattering vector, $\boldsymbol{q} = \boldsymbol{Q} - \boldsymbol{Q}_0$ is a reduced scattering vector and $\boldsymbol{U}(\boldsymbol{r})$ corresponds to the total displacement field at point $\boldsymbol{r}$ calculated as a superposition of displacement fields $\boldsymbol{u}(\boldsymbol{r})$ produced by defect located at the positions $\boldsymbol{R}$: $\boldsymbol{U}(\boldsymbol{r}) = \sum_{\boldsymbol{R}} \boldsymbol{u}(\boldsymbol{r} - \boldsymbol{R})$. The angular brackets denote the average over the statistics of the defect distribution.

If one considers large dislocation densities typical for GaN material, the correlation function $G(\boldsymbol{r})$ must be calculated for small distances $\boldsymbol{r}$. The distortion field of a dislocation follow the universal $1/R$ dependence. Taking into account that the main contribution to correlation function comes from remote dislocation ($R \gg r$)), Eq. 5.20 can be expanded as a Taylor series and the average can be performed according to Gaussian statistics:

$$G(\boldsymbol{r}) = \exp\left[-\frac{\rho}{2} \int (r_i Q_j \frac{\partial u_j}{\partial R_j} d\boldsymbol{R})\right]. \tag{5.21}$$

The derivative in Eq. 5.21 can be treated as $b\psi_{ij}/2/piR$, where b is the length of the Burgers vector and ψ_{ij} is a dimensionless factor that depends on the azimuth ϕ in diffraction experiment. Therefore Krivoglaz suggested to present the correlation function in the following form [140]:

$$G(\boldsymbol{r}) = \exp\left\{-C'\rho r^2 \int \frac{dR}{R}\right\}, \tag{5.22}$$

where

$$C' = \frac{Q^2 b^2}{8\pi^2} \int_0^{2\pi} (\widehat{r}_i \psi_{ij} \widehat{Q}_j)^2 d\phi. \tag{5.23}$$

Here, $\widehat{r}$ and $\widehat{Q}$ are unit vectors in the directions $\boldsymbol{r}$ and $\boldsymbol{Q}$ respectively.

In the case of TDs with dislocation lines perpendicular to the sample surface i.e. along the z-axis, Eq. 5.19 can be rewritten as

$$I(\boldsymbol{q}) = \delta(q_z) \int G(x, y) \exp(iq_x x + iq_y y) dx dy, \tag{5.24}$$

where the delta function $\delta(q_z)$ is due to the translational invariance in the direction of the dislocation lines. Integration of Eq. 5.24 over all direction of the scattered wave vector $\boldsymbol{K}_f$ yields a one-dimensional integral:

$$I(q) = \int G(x) \exp(iqx/\cos\Phi)dx, \tag{5.25}$$

in which Φ represents the angle between the (x, y)-plane and the scattered wave vector.

Kaganer's approach consists of a direct fit of the measured intensities on triple-axis diffractometer by the numerical Fourier transformation of the correlation function. From the fits, both the dislocation densities and the correlation range in the restricted random dislocation distribution were obtained.

In order to separate the screw and edge TDs the rocking curves in symmetrical and large inclined skew geometries were measured. The experimental setup had two different configurations, namely with open detector and with analyzer crystal. It was shown the advantage of open detector use, since the fitting procedure consists then in evaluation of the one-dimensional integral 5.25, while the analysis of the scans with the analyzer requires to compute the two-dimensional integration 5.24 of the correlation function. Therefore the model properties were discussed in case of experimental setup without analyzer crystal.

The final equation of the model to fit the measured intensity of the diffracted profile contains two parameters A and B describing the dislocation density ρ and the dislocation correlation length L respectively.

$$I(\omega) = \frac{I_i}{\pi} \int_0^{\inf} \exp(-Ax^2 \ln \frac{B+x}{x}) \cos(\omega x)dx + I_{backgr}, \tag{5.26}$$

where I_i is the integrated intensity of the peak and I_{backgr} is the background intensity. The Fourier integral in 5.26 can be quickly numerically computed. Achieving the best fits between the experimental and simulated ω scans, one can estimate the dislocation density and the dislocation correlation length as follows:

$$\begin{aligned} \rho_{s,e} &= \frac{A}{f b^2_{(s,e)}}, \\ L &= \frac{b_{(s,e)} B}{g}. \end{aligned} \tag{5.27}$$

The dimensionless quantities f and g are given by the diffraction geometry and vary from symmetrical to asymmetrical geometries.

The asymptotic behaviour of the rocking curve tails is analysed in detail in [3]. It has been shown that the slopes of x-ray profiles obey the q^{-3} law with a wide open detector and q^{-4} with an analyzer crystal. The deviation from these behaviour obliged to find another nature of the peaks broadening besides the dislocations.

The conventional equations 5.6 and 5.8 enabling to determine the density of dislocations from the FWHM were modified by Kaganer within his model:

$$\begin{aligned} \rho_e &\approx \frac{18\Delta\omega_e^2 \cos^2\Theta_B}{(2.8 + \ln M)^2 b_e^2}, \\ \rho_s &\approx \frac{36\Delta\omega_s^2}{(2.4 + \ln M)^2 b_s^2}, \end{aligned} \tag{5.28}$$

where $\Delta\omega_{(e,s)}$ are the FWHM of the rocking curve in skew and symmetrical geometries respectively, $M = L\sqrt{\rho}$ is the dimensionless parameter that characterizes dislocation correlation, and Θ_B stands for the Bragg angle. Compared to "classical" formulae, Eq. 5.28 resulted in a four times higher edge dislocation density and an order of magnitude higher screw dislocation density.

The densities of edge and screw TDs obtained from x-ray measurements were found in a good agreement with TEM results. It was estimated the range of correlation between randomly distributed dislocations. However, as it was mentioned in the paper, screw dislocations are not the only possible source of the peak broadening in symmetrical reflections. In order to determine their density precisely, one has to exclude the broadening due to edge dislocations, which lines deviate from the surface normal and include the stress relaxation at the sample surface.

The presence of misfit dislocations can be estimated in the similar way [26]. The intensity distribution of the diffracted wave in the scattering plane (xz) can be written as follows:

$$I(q_x, q_z) = \int_{-\inf}^{\inf} \int \int_0^d \langle \exp\{i[q_x x + q_z(z_1 - z_2) + \boldsymbol{Q} \cdot \boldsymbol{U}(x, z_1) - \boldsymbol{Q} \cdot \boldsymbol{U}(0, z_2)]\}\rangle$$

$$R(x)dxdz_1dz_2, \tag{5.29}$$

where $R(x)$ is the normalized resolution function of the experiment, z_1 and z_2 are values uniformly distributed from 0 to d. The angle brackets in Eq. 5.29 defines the averaging of the statistical ensemble over all possible defect configurations performed in this case by Monte Carlo method.

Kaganer et al. simulated the diffraction profiles in symmetrical reflexes and compared them to experimental data. The density of misfit dislocations were reliably determined. The method discussed above enables to distinguish the contributions of the screw threading dislocations and the misfit dislocations. It has been shown that MDs dominate in the diffraction peaks of thin films, while threading dislocations become important with increasing thickness.

5.2.4 Monte Carlo based approaches

The initial idea to use a Monte Carlo method for a numerical simulation of the diffuse scattering from threading dislocations belongs to V. Holý and V. Kaganer. This method directly allows to calculate the reciprocal space distribution from arbitrary dislocation arrays in any diffraction geometry.

Holý et al. applied Monte Carlo approach for simulation of threading dislocations in epitaxial laterally overgrown GaN layers [141]. The dislocation density determination was performed beyond the ergodic hypothesis. The condition of ergodicity is not valid when the measured x-ray signal cannot be averaged over the statistical ensemble of all defect configurations. It can occur when the samples with inhomogeneous defect distribution are explored by full-field microdiffraction imaging technique often called rocking-curve imaging (RCI) or by microbeam diffraction. The RCI technique enables to distinguish signals coming from individual grains of a mosaic structure. It means that the scattering by an individual dislocation of screw or edge type can be calculated, whereas a direct ensemble averaging is not feasible.

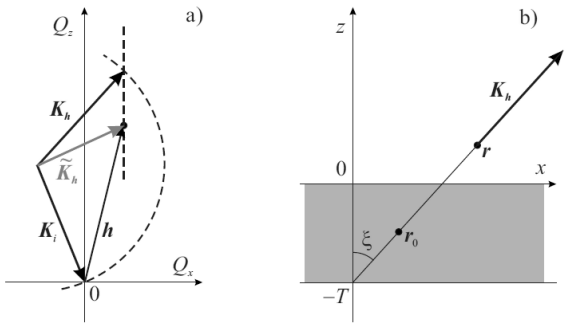

Figure 5.7: Sketch of the diffraction geometry used for RCI taken from [141]: a) in reciprocal space, b) in real space.

In general, the non-averaged amplitude of the scattered x-ray wave in point $\boldsymbol{r}$ outside the crystal can be written as:

$$E(\boldsymbol{r}) = \frac{K^2\chi_{\boldsymbol{h}}}{4\pi}\int_V d^3\boldsymbol{r}'\frac{\exp(iK|\boldsymbol{r}-\boldsymbol{r}'|)}{|\boldsymbol{r}-\boldsymbol{r}'|}\exp(-i\boldsymbol{h}\cdot\boldsymbol{u}(\boldsymbol{r}'))\exp(-i\check{\boldsymbol{K}}_{\boldsymbol{h}}\cdot\boldsymbol{r}'), \quad (5.30)$$

where $\chi_{\boldsymbol{h}}$ is the $\boldsymbol{h}$-th Fourier component of the crystal polarizability, V is the sample volume, and $K = \dfrac{2\pi}{\lambda}$. The meaning of vector $\check{\boldsymbol{K}}_{\boldsymbol{h}}$ can be understood from the Fig. 5.7. The standard kinematical two-beam approximation yields to significant simplification of the integral in Eq. 5.30, which is described elsewhere [2]. Beyond the ergodic hypothesis the two-dimensional integration over the planes parallel to the sample surface can be calculated using the stationary phase method. Then the expression for the scattered amplitude is:

$$E(\boldsymbol{r}) = \frac{K^2\chi_{\boldsymbol{h}}}{2K\boldsymbol{h}_z}\exp(i\boldsymbol{K}_{\boldsymbol{h}}\cdot\boldsymbol{r})\int_{-T}^{0} dz'\exp(-i(K_{\boldsymbol{h}z}-\check{K}_{\boldsymbol{h}z})z')\exp(-i\boldsymbol{h}\cdot\boldsymbol{u}(\boldsymbol{r}_0)). \quad (5.31)$$

Here, index z denotes the projection on the z-axis, $\boldsymbol{r}_0$ is the stationary point.

The simulation of the scattered intensity without performing the ensemble averaging is based on Eq. 5.31. Holý et al. considered separately random sets of screw and edge dislocation with definite dislocation densities in a square 200×200 μm^2 and calculated the intensities $I(\boldsymbol{r};\boldsymbol{K}_i)$ in symmetrical 0004 diffraction. There was no correlation in dislocation positions assumed. The explicit formulae for z-component of the displacement field that matters in symmetrical diffraction can be found in Sec. 2.2.1. Then, the data of RCI experiment, in which the signal comes from individual grains of a mosaic structure, were simulated. The local diffraction curves $I(\Delta\alpha_i)$ were obtained by numerical integration over a set of randomly placed virtual pixels with the size $D \leq L$.

It was established a strict connection between the FWHM β_i of the diffraction curves $I(\Delta\alpha_i)$ and dislocation density:

$$\beta_i = \zeta\sqrt{\rho}. \quad (5.32)$$

The coefficient ζ is equal to 2.2×10^{-6} or $(7.8\pm0.2)\times10^{-6}$ deg. cm for screw and edge TDs respectively. It was pointed out that the analysis of the diffraction curves tails can serve a method to estimate the prevailing type of the dislocations. The intensity diffusely scattered from edge threading dislocations drops approximately as q_x^{-2}, while for the screw threading dislocation, the intensity decreases roughly as q_x^{-3}.

By combining the Monte Carlo simulation method with the rocking-curve imaging, Holý et al obtained a detailed characterization method of the crystalline perfection in the micrometer scale. The next possible step is to develop the Monte Carlo approach within the conventional x-ray diffractometry, when the averaged scattered wave is considered statistically homogeneous and the sample under study is homogeneous as well. This investigation is one of the main topics of our work and its results can be found in Chapter 7.

Later on, Kaganer et al. presented a Monte Carlo technique to calculate the x-ray diffraction profiles from films with arbitrarily correlated dislocation distributions [29]. They considered the coexistence of misfit and screw threading dislocation ensembles with arbitrary correlations in relaxed c-plane GaN layers grown on SiC. In contrast to [141] Kaganer included the correlations in the dislocation positions. The discussion about the MDs density determination can be found in Sec. 2.2.2. The screw TDs were generated as positionally uncorrelated dislocation dipoles of random width. However, the widths were taken from an exponential distribution with the mean value s, which may be smaller or larger than the mean distance between dislocations r_d. It was shown that the width of diffraction peak depends on the r_d distance. When $s \ll r_d$, it is sharp. In the opposite limit, the dislocations are almost uncorrelated and the central part of the peak is a broad Gaussian.

The spatial integration in Eq. 5.30 was performed straightforward by the Monte Carlo method. The simulated rocking curves in symmetrical Bragg reflections were convoluted with a Gaussian resolution function, which dispersion σ_x defined the coherence length of the diffraction experiment. From comparison of theoretical and experimental rocking curves the densities of TDs and MDs were determined. However, this work was limited only to symmetrical diffraction, while the prevailing type of dislocation in GaN material is edge TDs, which affect mostly to asymmetrical or in-plane reflexes.

Kaganer and Sabelfeld continued their research in this field and performed the Monte Carlo study of dislocation screening applicable to cubic unit cell [142]. They arranged the screw and edge dislocations with opposite Burgers vectors in pairs providing the screening of the long-range strain field and calculated the diffracted intensity by method of standard quadratures. The averaging over statistics of the defect distribution was performed by Monte Carlo method. It has been shown that the width of simulated peaks was limited by the mean distance between dislocations in pair. The correlation length between dislocation pair was investigated in details.

Concerning GaN the theory in [142] is not completely suitable. The model of screening based on dislocation pairs with opposite Burgers vectors and correlation length can describe the properties of screw dislocations, whereas the hexagonal structure of GaN material does not permit to use apply it on edge threading dislocation. Egde TDs can have three different types of Burgers vectors that make an angle of 120^o between each other. Our independent study (see Sec. 7.2.1) shows that in about 2μm thick polar GaN samples the correlation in dislocation positions does not strongly influence the diffuse part of the diffracted intensity and it rather consumes the cpu time of computation than improves the accuracy of our approach.

5.2.5 Estimation of stacking faults density

In non-polar GaN grown heteroepitaxially on the foreign substrates the basal-plain stacking faults play an important role determining the properties of material. There are several attempts to characterize them quantitatively by x-ray diffraction technique.

Warren estimated the density of SFs in polycrystalline materials analysing the $\Theta - 2\Theta$ peaks broadening and their shift from Bragg positions [143]. Moram et al. made a detailed overview of x-ray diffraction from a-plane GaN films [144, 145]. They applied visibility criterion of stacking fault observation in TEM to x-ray diffraction: $\boldsymbol{g} \cdot \boldsymbol{R} \neq n$, where $\boldsymbol{g}$ is the diffraction vector, $\boldsymbol{R}$ is the SF displacement vector and n is integer. If this condition is fulfilled, the recorded RSMs possesses well pronounced diffuse streaks indicating the presence of SFs. There were observed I_1 and I_2 BSFs as well as PSFs in GaN/sapphire samples (see Sec. 2.2.3). The diffuse streaks were correlated to the density of SFs obtained from TEM. It was shown that the partial dislocations significantly contribute to the x-ray curve broadening and they have to be taken into account in data analyses.

McLaurin et al. investigated BSFs in m-plane GaN within mosaic block model [146]. The samples under study were grown by HVPE method on 6H m-plane SiC substrate. The SFs were considered as the boundaries of the crystalline domains being the sole source of the x-ray profiles broadening. Then modified Williamson-Hall analysis was used as a technique for determining of I_1 and I_2 BSFs densities [136].

Based on Warren theory for powder diffraction Paduano et al. developed the method of SFs density determination in m-plane GaN [147]. Several rocking curves in different reflections were measured. Those ones, where the criterion of SFs visibility is satisfied, show the substantial broadening. It is attributed to an independent contribution of crystalline tilt, twist, lateral coherence length, inhomogeneous lattice strain and stacking faults in material. The experimental profiles can be approximated as a sum of these contributions:

$$\Gamma^n = \left(\Gamma^a_{\perp} \cos(\chi)\right)^2 + \left(\Gamma_{\parallel} \sin(\chi)\right)^2 + \left(\frac{2\pi}{L^a K}\right)^n + \left(\xi \tan(\Theta)\right)^n + \left(\frac{B_{2\Theta}}{2} \sin(\xi)\right)^n, \tag{5.33}$$

Γ is the overall ω-scan peak width, K is the magnitude of the reciprocal lattice vector, χ is the inclination angle between diffraction plane and the surface normal, L is the average value of the lateral coherence length, $\Gamma_{\perp,\parallel}$ refer to the broadening resulting from tilt and twist respectively. Inhomogeneous strain contribution $\xi \tan(\Theta)$ depends on the Bragg angle Θ. The index a indicates the incident beam orientation parallel to $[11\bar{2}0]$.

The last item in Eq.5.33 characterizes the broadening due to BSFs. From the fits of experimental rocking curves in different diffractions one can exclude the influence of another factors and determine the $B_{2\Theta}$ value. In accordance with [143], the probabilities of I_1 and I_2 BSFs denoted as α and β are connected to the broadening of the rocking curves measured in (hkl) diffractions for even and

odd index l as follows:

$$\begin{aligned} l_{even} : B_{2\Theta} &= \frac{360}{\pi^2} \tan(\Theta)|l| \left(\frac{d}{c}\right)^2 (3\alpha + 3\beta) \ , \\ l_{odd} : B_{2\Theta} &= \frac{360}{\pi^2} \tan(\Theta)|l| \left(\frac{d}{c}\right)^2 (3\alpha + \beta). \end{aligned} \tag{5.34}$$

Here, d and c are the in-plane and out-of-plane lattice spacings, $|l|$ is the absolute value of the index l. The total fault densities can be estimated by multiplying the probabilities by the total number of planes along c-direction.

Besides the studies mentioned above, another methods of stacking faults densities determination in non-polar GaN performed with x-ray diffraction technique have not been yet published. Therefore the development of reliable method allowing to study the SFs quantitatively is of high importance. This reason made V. Holý et al. to start investigations resulted in theory presented in Sec. 9.

6. X-ray measurements of c-plane GaN and AlGaN layers

6.1 Measurements of GaN films

A large number of structural defects, especially threading dislocations with dislocation lines perpendicular to the surface are observed in c-plane GaN layers. The aim of our study is to determine independently densities of screw and edge TDs in the series of c-oriented samples (see Sec. 3.3.1). As a tool of our investigations we chose x-ray diffraction, which main advantage is its nondestructiveness, in contrast to the etching and TEM techniques. For each sample of our series we recorded RSMs in symmetric, asymmetric and grazing-incidence geometries. From comparison of experimental data with simulated ones in GID and coplanar diffractions we are able to find out the densities of edge and screw TDs respectively.

The difference between lattice parameters of the GaN epitaxial layer and sapphire substrate gives rise to misfit dislocations placed in their interface. The nonuniformity of the strains concentrated at the dislocation lines gives rise to diffuse scattering [26]. In coplanar diffraction, the defects distributed over the whole irradiated volume make contributions to scattered intensity. However, the displacement field caused by misfit dislocations is buried deeply under the sample surface and the main signal comes from threading dislocations stretching through GaN layer. In GID, the misfit dislocations are in general not detectable due to small penetration depth of x-ray beam. Misfit dislocations play an important role in diffracted intensity distribution if the thickness of an epitaxial layer is less then 0.5 μm [27]. Since the thinnest sample of our series is 1.8 μm thick (see Sec. 3.3.1), we neglect the presence of misfit dislocations and focus on TDs density determination.

6.1.1 Coplanar symmetrical and asymmetrical diffractions

The x-ray measurements were carried out on a Philips X'Pert PRO diffractometer equipped with a standard Cu Kα_1 tube [148]. We used a high resolution setup i.e. the Goebel parabolic mirror placed behind the x-ray tube, followed by a four-crystal Bartels monochromator (4xGe220) and a point detector with a three-bounce (3xGe220) analyzer crystal [149]. To reach a quasi-parallel beam geometry we used the fixed divergence slit of 1/4° and the automatic cross-slits of 1x4 mm^2 in incidence beam path. The 10 mm beam mask was installed before the mirror in order to define the irradiated width of the sample. The control of the axial divergence of the x-ray beam was performed by 0.04 rad Soller slits mounted between the mirror and the monochromator. The scheme with experimental setup is shown on Fig. 6.1.

The divergence of the primary beam of the diffractometer set-up and the angular acceptance of the crystal analyzer used in front of the detector were estimated as $\Delta\alpha_{i,f} \approx 12$ arc sec. According to Eq. 4.1.4 these values define the widths $\Delta Q_x \Delta Q_z$ of the device resolution function in the scattering plane $q_x q_z$ in

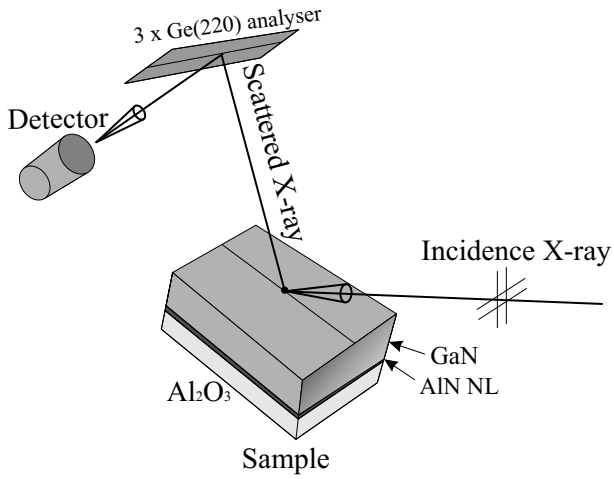

Figure 6.1: The scheme of coplanar measurements at laboratory diffractometer.

the directions perpendicular to the primary and diffracted beams, respectively [103]. The resolution element was estimated with Eq. 4.8

Across the scattering plane (i.e., along the q_y direction in reciprocal space), the divergence of the primary beam and the angular resolution of the detector were approximately 0.05°. From this value it follows that the reciprocal-space resolution ΔQ_y across the scattering plane is much larger than the width of the diffraction maximum. This fact enables us to consider the measured signal integrated in an infinite range along q_y axis, we included this q_y-integration in the device resolution function.

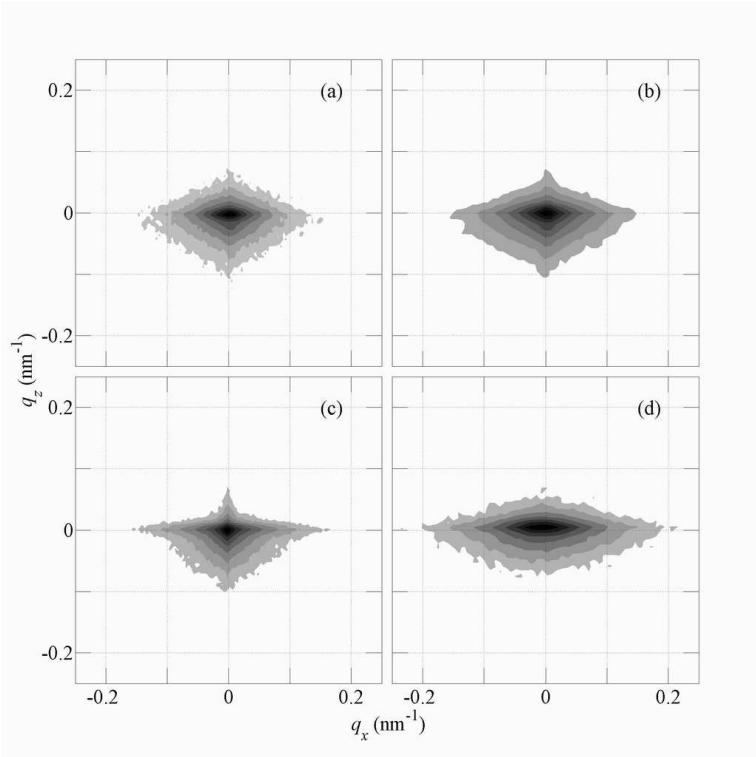

Figure 6.2: Measured 0004 RSMs of: (a) - S1, (b) - S2, (c) - S3, and (d) - S4 samples.

For each sample we measured the reciprocal-space maps (RSMs) around two reciprocal lattice points 0004 (symmetrical coplanar diffraction geometry) and

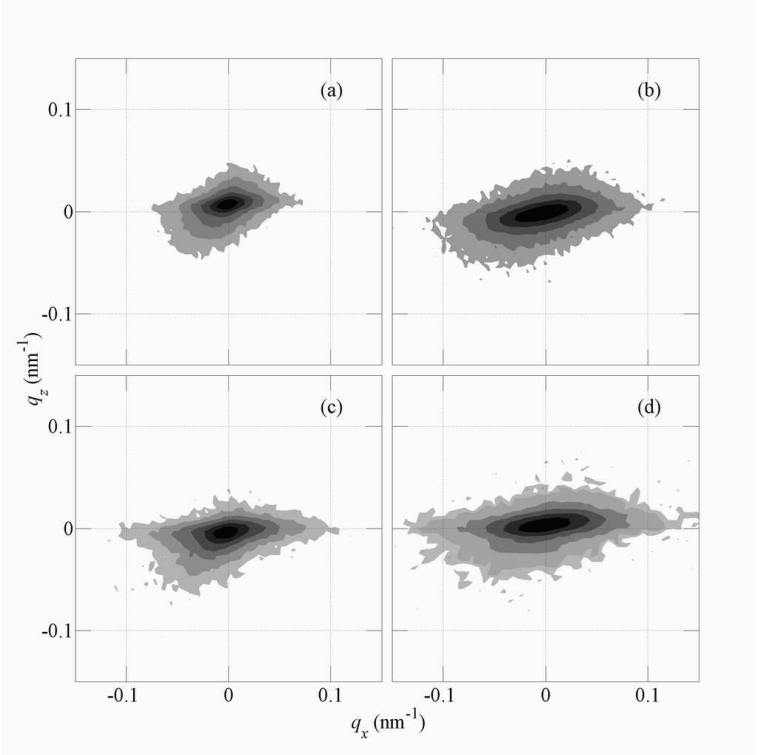

Figure 6.3: Measured $10\bar{1}4$ RSMs of: a) - S1, (b) - S2, (c) - S3, and (d) - S4 samples.

$10\bar{1}4$ (asymmetrical coplanar diffraction geometry, small exit angle). The reciprocal-space mapping consisted of a set of angular ω-scans measured for different values of $2\Theta/\omega$ where ω is the angular position of the sample and 2Θ is the scattering angle i.e. the angle of detector. As a result of the laboratory measurements we obtained the distributions of the measured scattered signal in the angular (ω, 2Θ)-space.

If z-axis is parallel to the surface normal and xz-plane coincides with the scattering plane, the formula for coordinates Q_x, Q_z in reciprocal space can be written as follows [103]:

$$\begin{aligned} Q_x &= \frac{2\pi}{\lambda}(\cos\alpha_f - \cos\alpha_i), \\ Q_z &= \frac{2\pi}{\lambda}(\sin\alpha_f + \sin\alpha_i). \end{aligned} \tag{6.1}$$

where α_i and α_f are the angle of incidence and the angle of exit respectively. They are related to ω and 2Θ angles:

$$\begin{aligned} \alpha_i &= \omega, \\ \alpha_f &= 2\Theta - \omega. \end{aligned} \tag{6.2}$$

Choosing the laboratory coordinate system so as mentioned above we converted the measured signal to the RSMs in the $(q_x q_z)$ plane perpendicular to the sample surface.

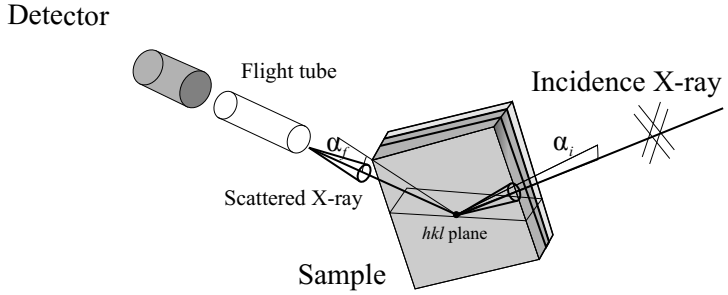

Figure 6.4: The scheme of GID measurements at synchrotron facility.

Fig. 6.2 and 6.3 show the measured reciprocal-space maps in symmetrical (0004) and asymmetrical ($10\bar{1}4$) diffractions respectively. From a direct comparison of the plotted RSMs we observe a significant broadening of the intensity distribution along the q_x axis with increasing dislocation density.

6.1.2 Grazing-incidence diffraction

In grazing-incidence diffraction (GID) the vector of diffraction is parallel to the Burgers vectors of edge threading dislocations. Therefore this geometry gives complete information for reliable determination of the density of edge TDs[150]. This type of dislocations makes up about 90 % of the total dislocations therefore it is of crucial importance to know their density with the highest possible precision.

In order to measure the diffuse part of the RSMs in GID, an intensive highly collimated synchrotron beam with a high-resolution experimental setup is required. Our x-ray experiment was carried out at the ID-01 beamline at ESRF (Grenoble, France) - samples S1, S2 and S3 and at the SCD beamline at ANKA (Karlsruhe, Germany) - sample S4. At both beamlines, we used the analogous high-resolution diffraction setup with the photon energy of 8 keV. This energy was selected basing on the sufficient distance from the Ga absorption edge. The basic scheme of experimental setup similar on both beamlines is depicted on Fig. 6.4.

The experiment was carried out on 6-circle Huber diffractometer. The sample kept in a He enclosure and placed vertically on the holder was irradiated by a monochromatic and parallel x-ray beam. We mounted an evacuated flight tube on the way between the sample and the point x-ray detector to avoid the scattering of the reflected beam in the air. We used Cyberstar NaI scintillator counter for our experiment. It had a number of advantages such as an appropriate selective energy range (from 5 keV to above 40 keV), a low noise (0.1 cps) and a relatively high maximum counting rate (2 x 10mm^5 cps) [151].

In order to collimate incidence and diffracted beams we used a set of slits. So called secondary slit were located at the beam path before the sample, flight tube and detector slits limited the beam size at the entrance to the respective elements. The distances between the principal elements of the setups and slit apertures differ for two beamlines (see Table 6.1). This fact yields a bit different shapes of the reflexes in reciprocal space recorded at ESRF and ANKA. Nevertheless, it should not affect our calculations because we analyse normalized intensities and moreover our software enables to include the resolution function of the experimental setup. This function can be represented by two-dimensional Gaussian with widths σ_{ang} and σ_{rad} in two perpendicular directions. The values $\frac{2\pi}{\sigma}$ represent the size of

Parameter	ID-01 beamline	SCD beamline
Distance between secondary slits and sample	15 cm	12.5 cm
Distance between sample and flight tube	32 cm	20 cm
Length of flight tube	65 cm	43 cm
Secondary slits size	0.5×0.5 mm^2	5×1 mm^2
Flight tube slits size	1×5 mm^2	5×5 mm^2
Detector slits size	1×5 mm^2	5×5 mm^2
σ_{ang}	$2.5\times10^{-2}nm^{-1}$	$4\times10^{-2}nm^{-1}$
σ_{rad}	$7\times10^{-2}nm^{-1}$	$1.1\times10^{-1}nm^{-1}$
The detector aperture	32 mm	32 mm

Table 6.1: The comparison of experimental parameters at ID-01 and SCD beamlines.

coherently irradiated area at the sample surface.

At the given experimental registration scheme, the vertical resolution element that corresponds to the angular acceptance of our system is defined by collimating properties of the slits $slit_1$ and $slit_2$ fixed in front and in the back side of the flight tube of the length L: $\Omega = \dfrac{slit_1 + slit_2}{L}$.

At the vertical scheme of diffraction experiment (both sample surface and diffraction plane are vertical) the vertical divergence is at least one order less than Ω. The horizontal divergence does not play any important role; horizontal size of the beam defines the projection length on the sample surface and for small incidence angles the visible length of the projection exceeds the size $slit_1$ of entrance slit of the flight tube. This considerations were taken into account estimating the values of σ in Table 6.1.

For each sample we measured the RSMs around two in-plane reciprocal lattice points $10\bar{1}0$ and $11\bar{2}0$ at the same incidence and exit angles $\alpha_i = \alpha_f = 0.6$ deg. close to critical angle. The Bragg angle Θ_i and the diffraction vector $\boldsymbol{h}$ lied in the plane of the sample surface, so the probing lattice planes were perpendicular to the surface. We performed a certain number of angular scans around the peak position at different radial distances. The distribution of the measured signal was converted from angular to reciprocal space (q_{ang}, q_{rad}). The axes in the reciprocal space are selected as followed: q_{rad} coincides with the direction of scattering vector, q_{ang} lies in the scattering plane and is perpendicular to q_{rad} (see

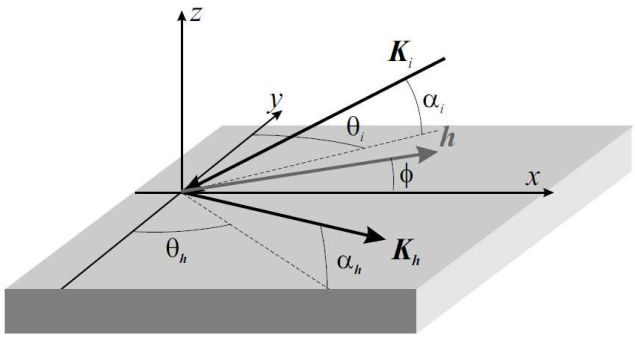

Figure 6.5: Definition of angles and axes for the GID setup taken from [103].

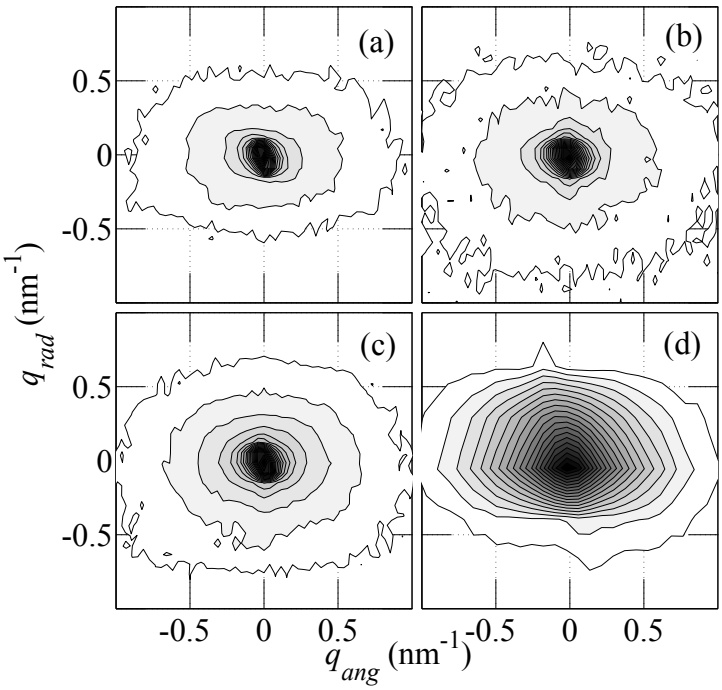

Figure 6.6: Measured $10\bar{1}0$ RSMs of: (a) - S1, (b) - S2, (c) - S3, and (d) - S4 samples.

Fig. 6.5). The formulae for geometric transformations taken from [103] are listed below:

$$Q_{ang} = -\frac{2\pi}{\lambda}(\cos\alpha_f \cos\Theta_f - \cos\alpha_i \cos\Theta_i), \tag{6.3}$$

$$Q_{rad} = \frac{2\pi}{\lambda}(\cos\alpha_f \sin\Theta_f + \cos\alpha_i \sin\Theta_i). \tag{6.4}$$

$$Q_z = \frac{2\pi}{\lambda}(\sin\alpha_f + \sin\alpha_i) \tag{6.5}$$

The RSMs in both geometries are depicted on Fig. 6.6 and 6.7.

In GID the roughness of the sample surface plays an important role. It gives rise to additional diffuse scattering that can be visible on RSMs [104]. Therefore for each sample we measured x-ray reflectivity (XRR). The long radial scans in the range between 0.3 and 10 degrees were performed in symmetrical coplanar geometry at energy of 8 keV. The reflected angle Θ was equal to incidence angle during XRR measurement. The data of measured XRR were corrected for the background intensity and normalized to unity.

The XRR curves were simulated with the commercial "Leptos" software for each sample. The roughness of sapphire wafer was neglected. The best fits were performed taking into account thin oxide layer on the top of GaN. The results of the simulations are depicted in Fig. 6.8 and the fit parameters are summarized in the Table 6.2. The root mean square surface roughness (σ^{rms}) of the thin GaN film decreases with increasing SiN_X deposition time. The nominal values of the surface roughness vary from 0.4 nm to 0.8 nm, while the thickness t of the oxide stays almost the same for all samples [152].

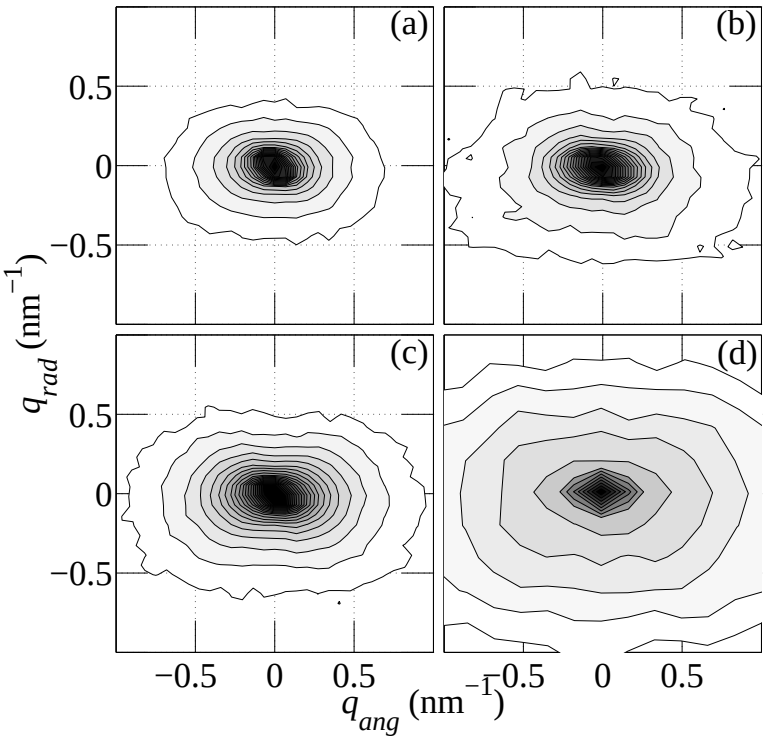

Figure 6.7: Measured $11\bar{2}0$ RSMs of: a) - S1, (b) - S2, (c) - S3, and (d) - S4 samples.

6.2 Measurements of $Al_{0.2}Ga_{0.8}N$ films

$Al_xGa_{1-x}N$ material has Wurzite crystal structure and possesses a large number of threading dislocations. In c-plane AlGaN samples the dislocation lines are perpendicular to their surface. For these objects we can apply our developed Monte Carlo method based on simulation of diffuse x-ray scattering to determine independently the densities of edge and screw TDs.

6.2.1 Coplanar symmetrical and grazing-incidence diffractions

The series of 5 $Al_{0.2}Ga_{0.8}N$ samples (see Sec. 3.3.3) were investigated at the SCD beamline at ANKA(Karlsruhe, Germany). The illustration of the sample sketch is depicted in Fig. 6.9. We used high-resolution x-ray reciprocal space mapping in coplanar symmetrical and noncoplanar grazing-incidence geometries.

Sample	σ^{rms}_{GaN} (nm), (s)	t_{oxide} (nm), ($10^8 cm^{-2}$)	σ^{rms}_{oxide} (nm)
S1	0.774	0.825	0.285
S2	0.671	0.662	0.304
S3	0.648	0.761	0.188
S4	0.448	0.614	0.166

Table 6.2: The roughness of GaN and oxide layers revealed from XRR. The third column contains the thickness of thin oxide layer.

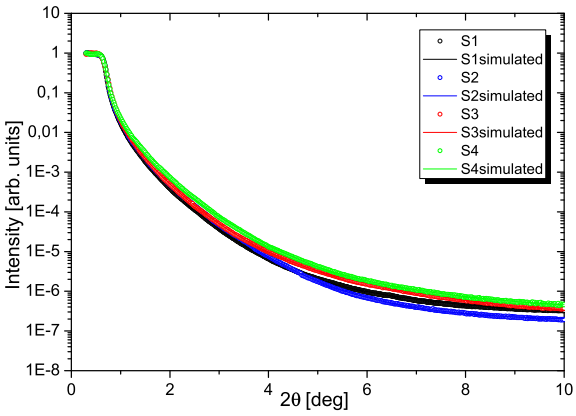

Figure 6.8: The x-ray reflectivities of the samples S1-S4.

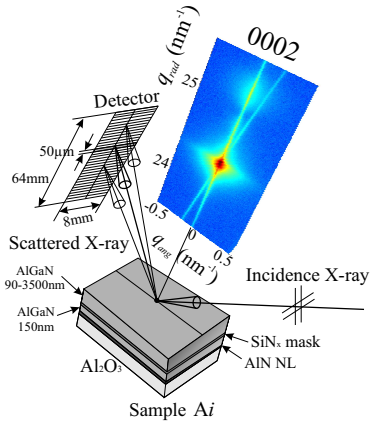

Figure 6.9: Schematic representation of the high-resolution symmetrical diffraction setup and the samples sketch.

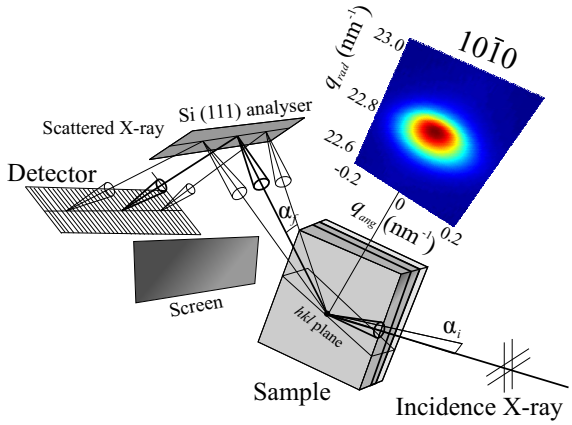

Figure 6.10: The setup of the GID geometry.

For each sample we recorded RSMs in coplanar 0002 diffraction. The measurements were performed with energy 8keV using Mythen 1K line detector. The angular resolution of the detector was predefined by the channel size 50 μm x 8 mm (full size of the detector was 6.4 mm that corresponded to 1280 pixels) and the distance between the center of diffractometer and the detector (700 mm). It was estimated as about 0.004 degrees per pixel. In coplanar symmetrical geometry, Mythen detector was placed in the scattering plane. In order to reduce the angular detector acceptance in direction perpendicular to the scattering plane, we used an 1 mm slit in front of the linear detector. This slit limited this acceptance to 0.08 deg. The experimental scheme of coplanar diffraction is shown in Fig. 6.9.

The examples of 0002 reciprocal space maps are depicted on Fig. 6.11. The narrow vertical streak over the maximum intensity corresponds to a crystal truncation rod and the inclined streak crossing the main peak from right top to left bottom is an artefact from monochromator. On each RSM several peaks of different intensities are visible. The penetration depth in coplanar geometry was estimated as about 5μm so all layers deposited on the sapphire substrate contributed to the RSM. It yields the presence of several peaks, which refer to several crystalline regions owing to different crystalline parameters in the growth direction [153].

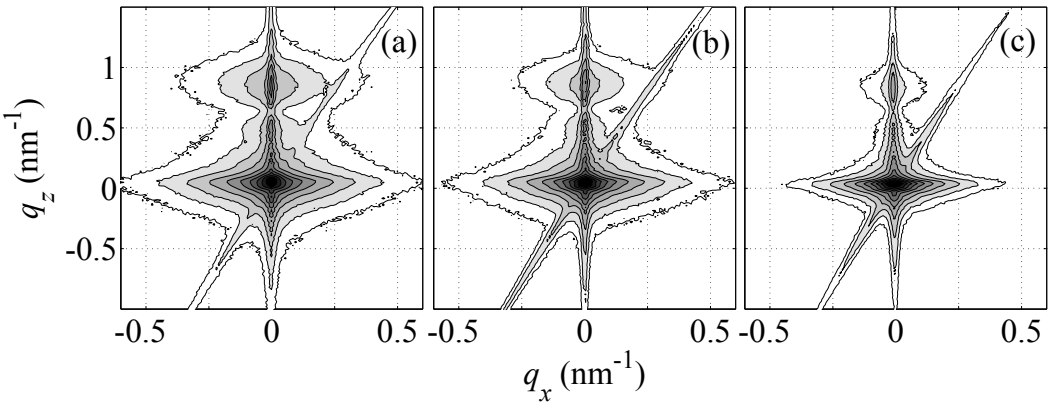

Figure 6.11: Measured 0002 RSMs of: (a) - A1, (b) - A3, and (c) - A5 samples.

The GID measurements were performed with energy 8keV using Mythen 1K line detector and Si (111) crystal analyzer. The samples were placed vertically and Mythen line detector with crystal analyzer was in horizontal positions (see Fig. 6.10). The in-plane resolution was organized by crystal analyzer and was about 0.003 degrees. In the out-of-plane direction the detector channels intensity was integrated from channel 400 up to 800. The examples of the experimental RSMs are shown on Fig. 6.12 and 6.13.

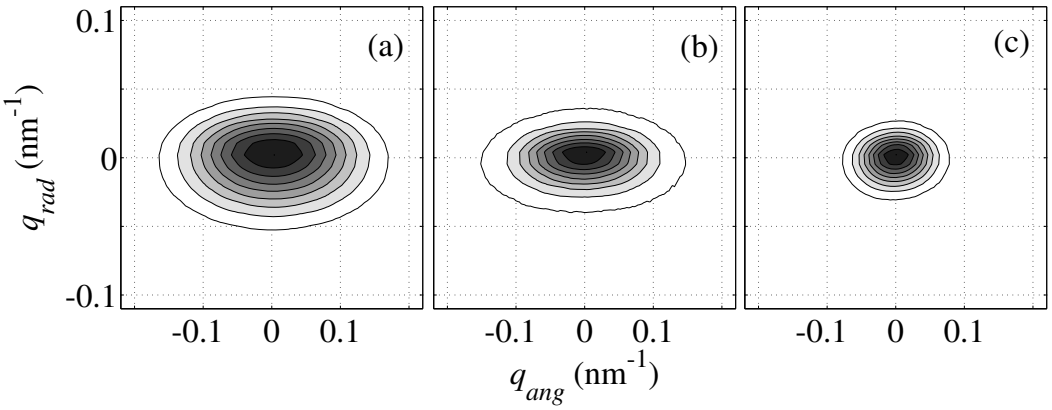

Figure 6.12: Measured $10\bar{1}0$ RSMs of: (a) - A1, (b) - A3, and (c) - A5 samples.

6.2.2 High-order coplanar symmetrical diffraction

The analysis of the coplanar 0002 RSMs showed elongated peak of AlGaN in q_z direction that gave us an idea to examine the series of samples in high-order diffractions. We performed preliminary measurements in the symmetrical diffractions from 0004 to 00010 for one sample. In contrast to RSMs of GaN, the overlap of two peaks denoted was found in the case of AlGaN. This fact indicated

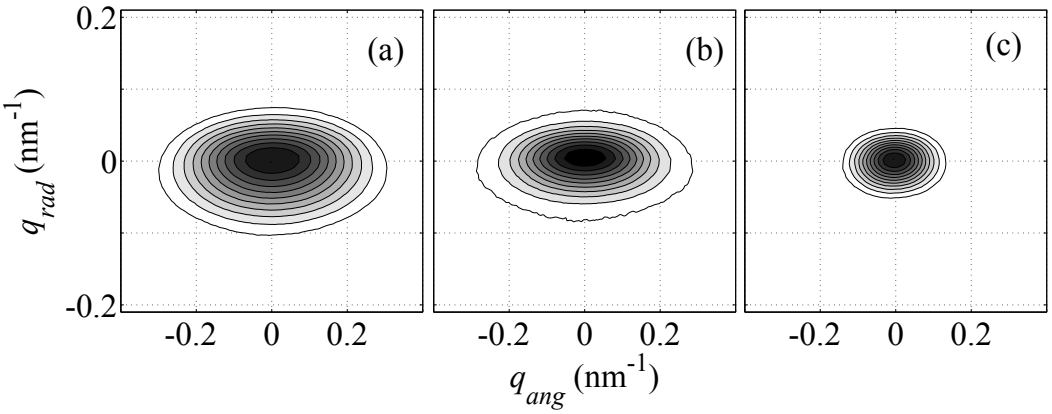

Figure 6.13: Measured $11\bar{2}0$ RSMs of: (a) - A1, (b) - A3, and (c) - A5 samples.

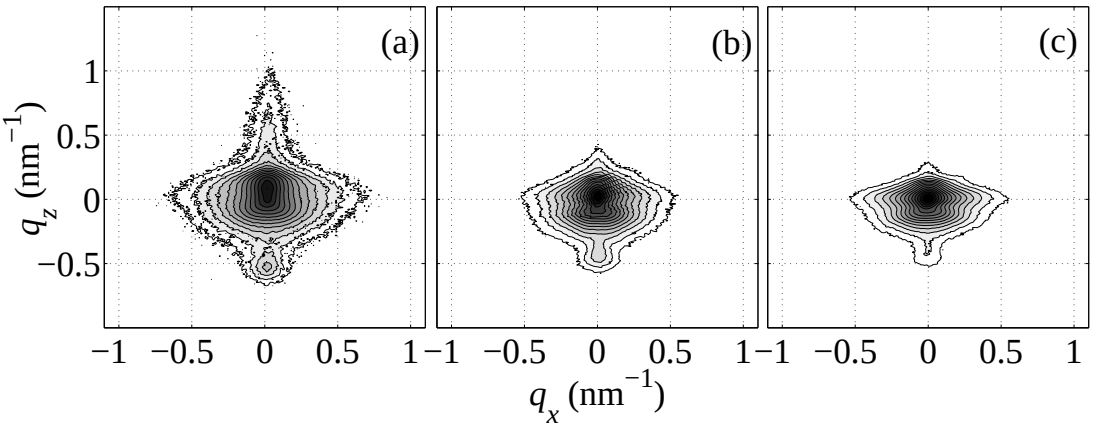

Figure 6.14: Measured 0008 RSMs of: (a) - A1, (b) - A3, and (c) - A5 samples.

the presence of two phases of AlGaN with different vertical lattice parameters. The best compromise between the diffracted intensity and the peak splitting was observed for 0008 diffraction, which was measured at energy of 12 keV. In order to analyse the double-peak phenomenon in detail, we recorded 0008 RSMs for all samples. They are shown in Fig. 6.14.

The detailed analysis of the 0008 RSM reveals four peaks, named as GaN rich peak, AlGaN bottom 150 nm peak, AlGaN main overgrowth peak and AlN rich peak in the symmetrical RSMs indicated in Fig. 6.15 for the sample A2. In our investigations, we are interested in AlGaN phase and neglect the influence of AlN and GaN phases.

The evolution of x-ray pattern as a function of the overgrowth was examined by recording the RSM of the refection 0008 for different samples. For completeness of our analyses we measured 0008 RSM for the sample A0. The cuts along the CTR were derived from the RSMs and plotted in Fig. 6.16. The different profiles were scaled vertically to demonstrate the change in peak position and intensity as the function of the overgrowth thicknesses.

In order to identify the origin of the different peaks and to show accurately the resulting changes in peak position and broadening, a deconvolution procedure was

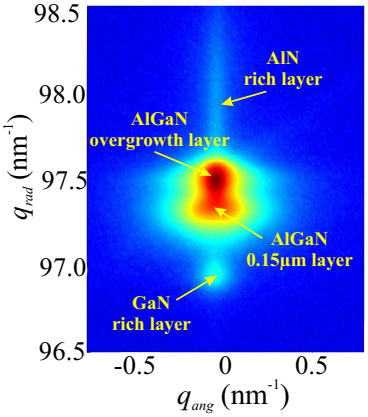

Figure 6.15: RSM of the sample A2 in 0008 diffraction. The main peaks are indicated.

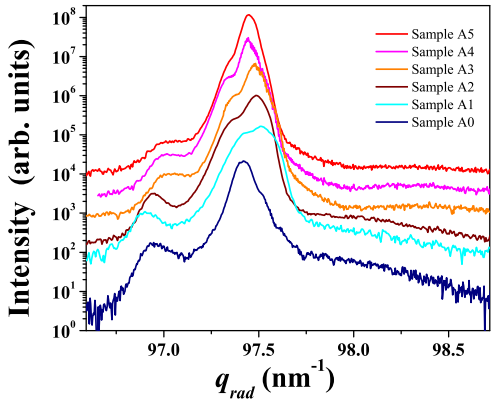

Figure 6.16: CTR cuts derived from the 0008 RSMs for all samples.

applied systematically for all samples. We depicted the results of deconvolution by five Lorentzian peaks in Fig. 6.17 and 6.18 for the samples A0 and A5 with the lowest and the highest overgrowth thicknesses respectively. The peaks are named Peak 1 - Peak 5 for simplicity as it is shown in the figures. The choice of Lorentzians for the individual peaks led to a good fit of the measured x-ray profiles.

We propose to follow the change in the peaks by increasing the overgrowth thickness. For this purpose, we introduced h_0 as the thickness of the AlGaN layer below SiN_X mask having a fixed thickness of 150nm and h as the thickness of the overgrowth layer varying from 0.09 μm to 3.5μm. It should be noted that only for sample A0 the overgrowth thickness h=89 nm is less than the thickness of AlGaN interlayer with h_0=150 nm deposited below the SiN nano-mask, whereas for the samples of our series $h > h_0$.

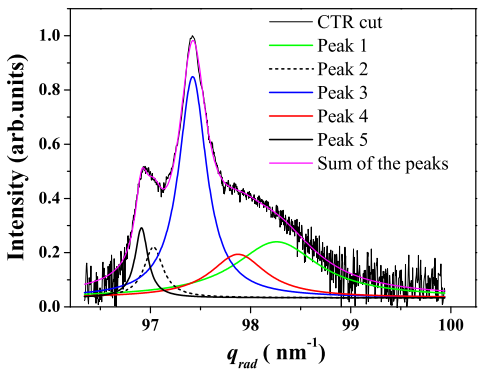

Figure 6.17: CTR cut of the sample A0 for the 0008 diffraction and the corresponding decomposed peaks.

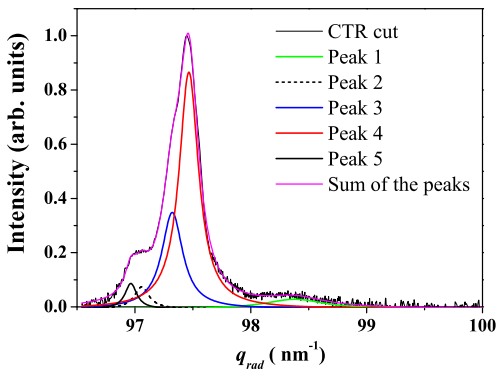

Figure 6.18: CTR cut of the sample A5 for the 0008 diffraction and the corresponding decomposed peaks.

Considering the Fig. 6.17 and 6.18 one should note that the Peak 3 as well

as the Peak 4 are appeared at comparable scattering vectors q for both samples. The Peak 3 is located at $q = 0.9742\text{nm}^{-1}$ for A0 and $q = 0.9732\text{nm}^{-1}$ for A5, while the Peak 4 is observed at $q = 0.9787\text{nm}^{-1}$ for A0 and $q = 0.9746\text{nm}^{-1}$ for A5. For the sample A0 the intensity of the Peak 3 is higher than of the Peak 4. For the sample A5 the intensity behaviour for the Peaks 3 and 4 is opposite. From Fig. 6.16 it is seen that the gradual change in the overgrowth thickness h enhances the visibility of the Peak 4 with respect to the Peak 3.

This allows us to conclude that the Peak 3 is originating from the AlGaN layer below the SiN_X mask with the constant thickness $h0 = 150$ nm while the Peak 4 is strongly related to the overgrowth layer. The other peaks obtained from the fitting are attributed to the pure AlN (Peak 5 at $q = 0.9787\text{nm}$) and GaN (Peaks 1 and 2) crystalline structures.

Thus we have demonstrated with the measurement of RSMs in high diffractions the presence of two distinguishable AlGaN phases with different crystalline parameters. The results of our advanced analyses enable to allocate these two crystalline phases to the AlGaN layers below and above the SiN_X mask.

7. Monte Carlo method for threading dislocation densities determination in c-plane nitride-based layers

7.1 Theoretical background for model application

Diffuse x-ray scattering from defects can be described by the standard theory of Krivoglaz [2]. However, in our case this approach is not convenient because the ensemble averaging of the scattered intensity cannot be calculated directly, since the dislocations are perpendicular to the sample surface. The background of our theoretical model is based on the preceding works of Holý, Daniš and Kaganer [3, 29, 141, 154]. Our calculations make it possible to include the surface stress relaxation in the formulae for the displacement field caused by edge and screw TDs. Therefore the ensemble averaging is expressed by a two-dimensional integral over the sample surface that is difficult to evaluate numerically. We perform the ensemble averaging using a Monte-Carlo method instead. A comparison of simulated and measured reciprocal space maps allows us finally to determine the densities of particular types of threading dislocations.

For the simulation of the reciprocal-space distribution of scattered intensity we assume two points:

- the measured intensity is averaged over a statistical ensemble of all configurations of the dislocations;
- the distance sample-detector is large so that the far-field limit can be used.

The validity of the first assumption depends on the density of dislocations, on the coherently irradiated sample surface S_{coh} of the primary radiation and on the total size of the irradiated sample surface S_s [141]. According to our estimations of coherently irradiated area the value of S_{coh} is approximately 200×300 nm in coplanar diffraction and about 250×900 nm in GID. At that time the total illuminated area may reach 1×5 mm. Practically this means that for realistic modelling of scattering experiment one should make use of incoherent accumulation of the scattering pattern over the small ensemble of coherently irradiated areas. In our particular case, we have modelled a unique dislocation distribution for each coherent surface element, which, taken into account the total amount of elements, means averaging over representative selection of all possible configurations.

The far-field approximation is valid if the diameter of the coherently irradiated sample surface S_{coh} is much smaller than the diameter of the first Fresnel zone. The later can be approximated by the expression $\sqrt{R\lambda}$, where R is the sample-detector distance and λ is the wavelength. For a standard laboratory setup and moreover for synchrotron beamlines this condition is fulfilled.

7.2 Algorithm of Monte Carlo simulation

V. Holý et al. developed a new software enabling to compute the reciprocal space maps of the scattered intensities in different geometries. The calculation strategy can be represented as follows [148].

- In a coherently irradiated area we generate the positions and types of the threading dislocations using a random generator.
- We calculate the displacement field caused by dislocations defined in the previous step.
- We compute the amplitude of the diffracted wave E_j and the diffracted intensity $I_j = |E_j|^2$.
- We repeat the items 1-3 M times and obtain the intensities I_j, $j = 1, \ldots, M$. Each intensity distribution I_j corresponds to the intensity scattered for a single coherently irradiated area, M is the number of these areas in the totally irradiated sample area.
- We calculate the average intensity distribution in $q_x q_z$ plane

$$I(q_x, q_z) = \frac{1}{M} \sum_{j-1}^{M} I_j(q_x, q_z) \tag{7.1}$$

- We convolute the intensity from Eq. 7.1 with the resolution function of our experimental setup.

In this section, we give a detailed description for each of these steps and estimate the error of our method.

7.2.1 Generation of dislocation types and positions

Using a numerical generator of uniformly distributed random numbers we generate random positions of given numbers of dislocations of different types in the square patch that corresponded to the coherently irradiated area S_{coh}. The mean number of dislocations of a given type in this area is deduced from its particular dislocation density that was used as an input parameter. The numbers of dislocations in one coherent area S_{coh} are random and they are distributed according to the binomial distribution with given mean value. The size of the coherently irradiated area L_{coh} is given by experimental setup. In our program it is inversely proportional to step in reciprocal space in accordance with the sampling theorem, which is a consequence of the Fourier transformation used in RSMs calculations [155]. Let a reciprocal-space map was simulated in N_x points separated by dq_x intervals along q_x axis. The corresponding real-space sampling intervals (or the steps in real space) can be written as $dx = \frac{2\pi}{N_x dq_x}$. The value $N_x dx$ is equal to the size L_{coh} of the coherently irradiated area, in which the dislocations are simulated. The similar expressions are valid for q_z direction.

We included five types of dislocations in two dislocation "families": two types of screw dislocations with the Burgers vectors $\boldsymbol{b}_s = \pm[0001]$ (so-called

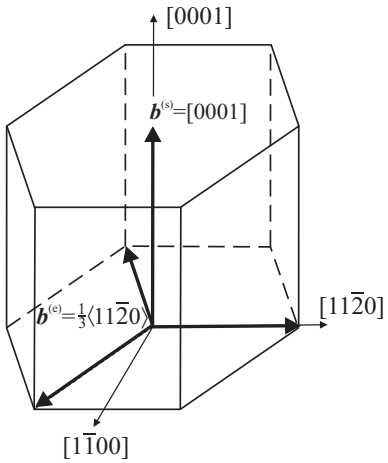

Figure 7.1: Burgers vectors of the dominant dislocation types in the GaN epitaxial layers.

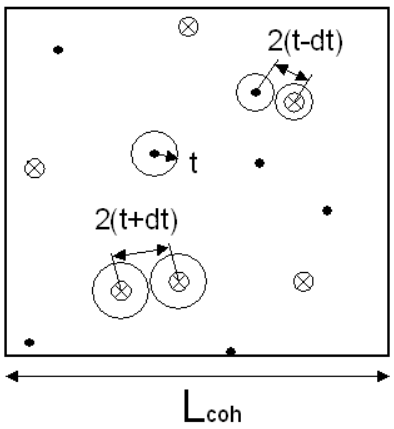

Figure 7.2: The sketch of the depleted zones between screw dislocations with Burgers vectors [0001] (dots) and [000$\bar{1}$] (crosses).

c-dislocations), and three types of edge dislocations with the Burgers vectors $\boldsymbol{b}_e = \frac{1}{3}\langle 11\bar{1}0\rangle$ (a-dislocations)[156] shown on Fig. 7.1. We assume that the densities of different dislocation types belonging to the same family are equal. So, we use only two dislocation densities ρ_s and ρ_e (total densities of screw and edge dislocations, respectively) as input parameters.

We performed a number of simulation in which the correlation in dislocation positions were included. For non-correlated the mean distance R_m between two dislocation of the same type can be estimated from expression $R_m \sim \frac{1}{\sqrt{\rho}}$. We assumed that there was a depleted zone around each dislocation, where no other dislocation of the same type could occur. The radius t of this zone was constant for edge threading dislocations and depended on the dislocation types for screw ones. We considered 10-% decrease $-dt$ of this radius between opposite directed screw dislocations placed in close vicinity to each other and 10-% increase $+dt$ for dislocations of the same direction (see Fig. 7.2). We simulated RSMs in 0004 diffraction keeping all input parameters constant except the radius of depleted zone. The dislocation densities for these estimations were taken from EPD (see Sec. 3.3.1). We extracted the cuts through diffraction maxima along the q_x axis and plotted them on the same graph 7.3. It is seen that the value of depletion radius does not strongly affect the intensity distributions. Therefore for our samples, where the total dislocation density is of order 10^8 cm^{-2} the correlation in dislocation position can be neglected in order not to slow down time consuming calculations.

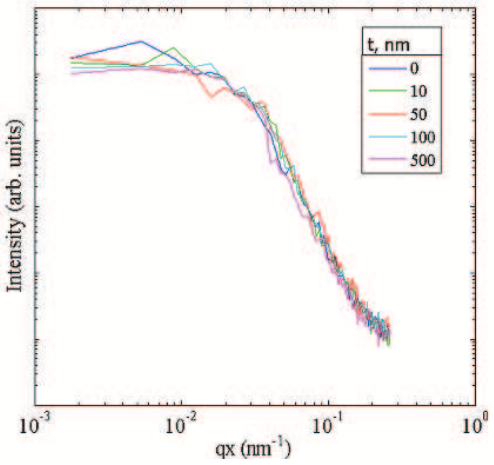

Figure 7.3: The intensity profiles along q_x axis calculated with different values of depletion radius.

7.2.2 Displacement field calculation

From positions of individual dislocation types generated in S_{coh} we calculate the total displacement field of all dislocations assuming a linear superposition.

$$\boldsymbol{u}(x,y,z) = \sum_{\alpha=1}^{5}\sum_{j=1}^{N_\alpha}(u)^{(\alpha)}(x-x_j^{(\alpha)}, y-y_j^{\alpha}, z), \tag{7.2}$$

where $(u)^{\alpha}(x,y,z)$ is the displacement vector in point (x,y,z) due to a dislocation of type α ending at the sample surface in point $(x,y)=(0,0)$, and $x_j^{(\alpha)}, y_j^{(\alpha)}$ is the intersection point of the j-th dislocation of type α with the sample surface. The expression for $(u)^{\alpha}(\boldsymbol{r})$ are taken from [25]. For TDs with dislocation lines perpendicular to the sample surface these formulae are significantly simplified. They can be found in Sec. 2.2.1 and in the text of our program in Appendix A for RSMs simulation.

The main advantage to use these cumbrous expressions for displacement field caused by TDs is that they include surface relaxation of internal stresses. This fact enhances the precision of determined dislocation densities by our Monte Carlo simulation comparable to another methods.

The examples of displacements produced by a pure screw and a pure edge dislocations placed in the middle of the patch is shown on Fig. 7.4. Here we plot the stress distribution in the plane parallel to the sample surface.

In general, the scattered intensity depends only on the component of the total displacement field parallel to the diffraction vector $\boldsymbol{h}$. Therefore in symmetrical diffraction only the vertical component $u_z(\boldsymbol{r})$ matters. The expressions for $u_z^{s,e}(\boldsymbol{r})$ become simple:

$$\begin{aligned} u_z^{(s)}(\boldsymbol{r}) &= \frac{b_z^{(s)}}{2\pi}\arctan\frac{y}{x}, \\ u_z^{(e)}(\boldsymbol{r}) &= \frac{\nu}{1-\nu}\frac{\boldsymbol{r}\boldsymbol{b}^{(e)}}{2\pi}\frac{z+2r(\nu-1)}{r(r-z)}, \end{aligned} \tag{7.3}$$

where ν is the Poisson ratio assumed for simplicity as isotropic elasticity.

In GID simulations we did not take into account screw dislocations, since their presence did not bear any influence on RSMs shapes.

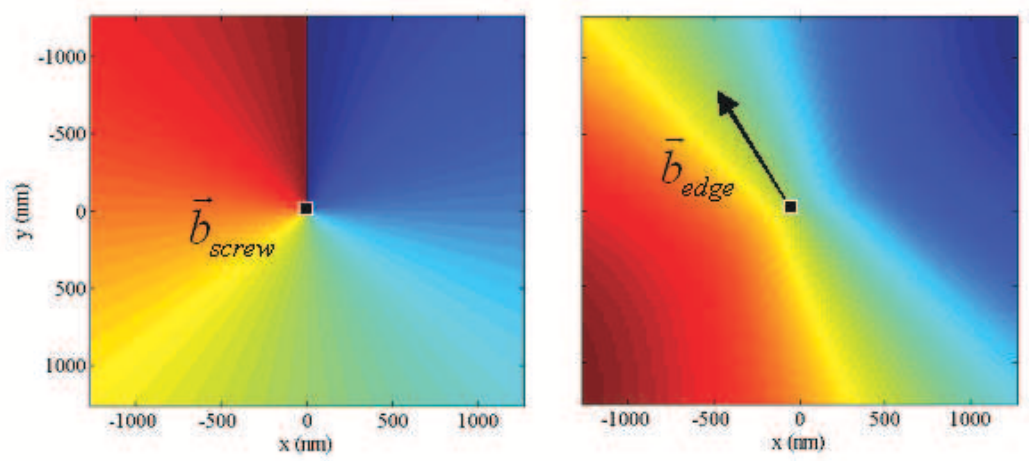

Figure 7.4: The displacement field distribution for single screw (left) and edge threading dislocations (right) in the depth z=1μm.

7.2.3 Reciprocal space maps calculation

The intensity of x-ray wave scattered by dislocation generated in S_{coh} is proportional to the second power of the diffracted wave amplitude. Using the far-field limit and kinematical approximation the intensity diffuse scattering in the point $\boldsymbol{q}$ in reciprocal space can be written as: :

$$I(\boldsymbol{q}) = \left\langle \left[A \iint\limits_{S_{coh}} \mathrm{d}x\mathrm{d}y \int\limits_{-T}^{0} \mathrm{d}z e^{-i\boldsymbol{h}.\boldsymbol{u}(\boldsymbol{r})} e^{-i\boldsymbol{q}\boldsymbol{r}} \right]^2 \right\rangle, \tag{7.4}$$

where T is the sample thickness and the averaging is performed over random dislocation positions and types. In Eq. 7.4 A is a constant containing the amplitude of the primary wave, the polarizability coefficient $\chi_{\boldsymbol{h}}$,$\boldsymbol{q} = \boldsymbol{K}_f - \boldsymbol{K}_i - \boldsymbol{h}$ is the reduced scattering vector and $\boldsymbol{K}_{i,f}$ are vectors of the primary and scattered vectors respectively.

The intensity in Eq. 7.4 has a form of Fourier transform of function $e^{-\boldsymbol{h}.\boldsymbol{u}(\boldsymbol{r})}$. This fact is used in our software to compute the integral in 7.4. However Fourier transform of a 3-d function determined in the limited ranges may cause artefacts. Let us consider the most obvious and annoying of them. The strong peaks in reciprocal space are accompanied by cross-like artefacts caused by the boundaries of the integration volume. Another words, these artefacts are truncation rods generated by the faces of the integration volume. Secondly, due to limited precision of computer number representation and limited number of fast Fourier transform nodes one can easily observe the digital noise, which looks like a rippling at the regions of low intensity. Thirdly, a moderate sampling dx of the model in Eq. 7.4 imposes the artificial periodicity $\dfrac{2\pi}{dx}$, which has no relation to the real reciprocal space periodicity and leads to the effects similar to mirroring of distinct linear features (truncation rods) at the borders of the reciprocal space zones.

All artefacts mentioned above should be certainly taken into account when the sampling rate and volume size is selected, and their minor existence - during the interpretation the simulated RSMs.

The averaging is performed over random dislocation positions and types. For this reason we repeat the steps described in the subsections above about $M = 1000$ times and the intensities scattered by different coherent areas S_{coh} are summed.

Finally, the simulated intensities are convoluted with the resolution function of our diffractometer setup(see Sec.6). For symmetrical diffraction its shape in the scattering plane ($q_x q_z$) was approximated by a two-dimensional Gaussian function $J(q_x, q_z)$ with the dispersions ΔQ_x and ΔQ_z defined in Eq. 4.15 that correspond to the sizes of the resolution elements in reciprocal space:

$$J(q_x, q_z) \approx \exp\left[-(\frac{(q_x - q_{x0})^2}{2\Delta Q_x^2} + \frac{(q_z - q_{z0})^2}{2\Delta Q_z^2})\right] \tag{7.5}$$

Due to analyzer placed in the reflected beam path, the resolution function along q_y axis is assumed to be infinitely broad. In GID the directions q_x and q_z correspond to q_{ang} and q_{rad} respectively and the dispersions of the Gaussian-shape resolution function is takes from 4.17.

7.3 Monte Carlo simulation in c-plane GaN

7.3.1 The analysis of simulated reciprocal space maps

On Fig. 7.5 we depicted calculated RSMs in symmetrical (0004), asymmetrical ($10\bar{1}4$) and grazing-incidence ($11\bar{2}0$) diffractions for sample S2. The simulated maps consists of narrow and intensive coherent peak and the diffuse part with decaying intensity. For a successful application of our method the mean distance R_m between the dislocations must be smaller than the coherence width of the primary radiation projected to the sample surface, i.e., the central coherent peak must be much narrower than the width of the diffuse maximum. In each geometry this condition is completely satisfied.

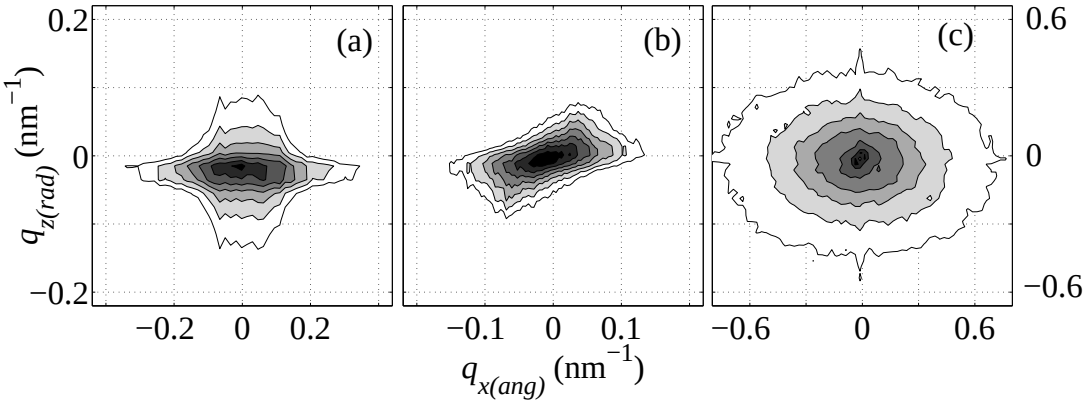

Figure 7.5: Calculated RSMs for sample S2: (a) - 0004, (b) - $10\bar{1}4$, and (c) - $11\bar{2}0$ diffractions.

In symmetrical geometry, we subtracted the crystal truncation rod going parallel to q_z direction in order better to fit experimental and simulated RSMs. However, it did not affect the diffuse part of the intensity distributions.

From the Eq. 7.2.2 for $u_z^{(s)}(\boldsymbol{r})$ it follows that the vertical component of the displacement field around a screw threading dislocation does not depend on the vertical coordinate z. After Fourier transformation of the constant function defined in the interval $[0, T]$ we observe in symmetrical RSM a horizontal sheet with the width of $2\pi/T$, where T is the total thickness of the GaN layer.

Under GID conditions the surface roughness may seriously affect the results [2]. The ration of the diffuse scattering from dislocations and from the roughness can be approximately estimated to [157, 158]

$$\frac{I_{roughness}}{I_{dislocation}} \approx \frac{(\sigma\xi)^2}{(TL_{coh})^2}, \tag{7.6}$$

where σ is the root-mean square roughness of the substrate, and ξ is the roughness correlation length. From x-ray reflectivity measurements we determined $\sigma \approx$0.6 nm and $\xi <$100 nm. Since the sample thicknesses T are about 2000 nm and the coherence length $L_{coh} \approx$200 nm, the ratio in 7.6 is of order 10^{-8}, so the roughness contribution can be neglected.

The actual number of coherent areas in the irradiated sample surface S_s is of the order of $10^7 - 10^8$ in our experimental setup. However, the averaging was performed only 1000 times, since the numerical simulations were very time-consuming. Therefore the obtained RSMs are not fully ensemble-averaged and random fluctuations of the intensity are still visible but the main features of the calculated intensity distributions can be well resolved. The statistical error can also be estimated by the Monte Carlo method. The root-mean-square (rms) deviation σ_I of the average intensity is

$$\sigma_I^2 = \frac{1}{M}\left[\frac{1}{M}\sum_{j-1}^{M} I_j^2 - \left(\frac{1}{M}\sum_{j-1}^{M} I_j\right)^2\right] \tag{7.7}$$

When the number M of coherently irradiated volumes increases, the rms deviation σ_I decreases. The simulation procedure is rather time-consuming so we were not able to use the actual number M given by the experimental conditions. Instead, we chose M in such way that the maximum of $\sigma_I(q_x, q_z)$ did not exceed 10%.

7.3.2 The reciprocal space maps comparison

First, we started with simulation of RSMs in coplanar geometries, namely in 0004 symmetrical and $10\bar{1}4$ asymmetrical diffractions. In symmetrical diffraction, the diffraction vector $\boldsymbol{h} = 0004$ is perpendicular to the sample surface. Therefore it is parallel to the Burgers vector $\boldsymbol{b}^{(s)}$ of screw TDs and perpendicular to the Burgers vector $\boldsymbol{b}^{(e)}$ of edge TDs. In an infinite medium, the displacement field $\boldsymbol{u}(\boldsymbol{r})$ around a dislocation is almost parallel to its Burgers vector. Since the diffusely scattered x-ray intensity depends on the scalar product $\boldsymbol{h} \cdot \boldsymbol{u}(\boldsymbol{r})$, mainly screw threading dislocations contribute to the 0004 RSM. The influence of the edge threading dislocations is minor. It is caused by a surface relaxation of internal stresses around an edge threading dislocation, giving rise to a small non-zero vertical component $u_z(\boldsymbol{r})$ of the displacement vector.

In the asymmetrical diffraction the diffraction vector $\boldsymbol{h} = 10\bar{1}4$ has a non-zero angle to the Burgers vectors of both dislocation types. On asymmetrical RSM we see the intensity distribution caused by screw and edge threading dislocations.

For each sample we assumed the same density of pure screw and edge TDs in both geometries. With these input data we tried to achieve the best fits of experimental and simulated RSMs. We plotted them both at the same graph (see Fig. 7.6) and required the best possible coincidence of the shapes and intensity levels.

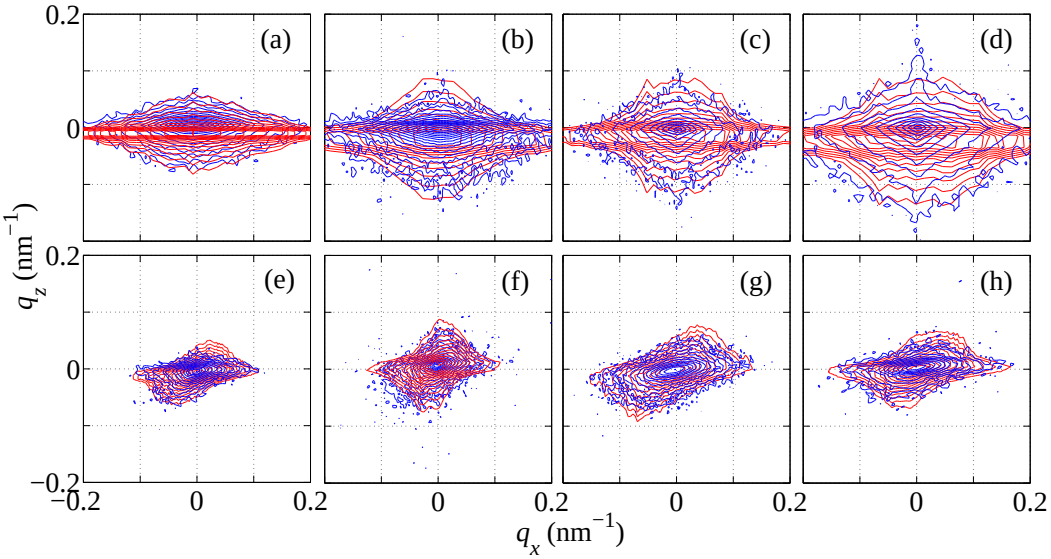

Figure 7.6: Measured (blue) and simulated (red) reciprocal space maps in 0004 (panels a-d) and $10\bar{1}4$ (panels e-h) diffractions of: (a,e) - S1, (b,f) - S2, (c,g) - S3, and (d,h) - S4 samples. The intensity step is $10^{0.5}$ in logarithmic scale.

The comparison of RSMs allowed us to determine the densities of screw and edge TDs with the error of $\pm 15\%$. However, due to surface relaxation and large number of edge TDs, their contribution into symmetrical diffraction remains substantial. In asymmetrical diffraction both types of TDs contribute likewise to the diffraction pattern. To estimate the prevailing type of dislocations and separate their influence we analyse the asymptotic part of two perpendicular cuts of the RSM that crosses the intensity maximum (see Sec. 7.3.3). Their slopes in log-log representation depend on the dislocation densities, types and experimental resolution. With known experimental resolution, they allow us to define quantitatively the ratio between densities of two dislocation types. Therefore the task to determine the density of screw and edge dislocations independently is not easy. The simulations with different input data can give the identical RSMs shapes i.e., the solution of our problem is not unique and some additional analyses are required.

One way to overcome the problem mentioned above is to measure and simulate the diffuse scattering in grazing-incidence geometry. In GID, the Burgers vectors of screw dislocations are perpendicular to the vector of diffraction. In contrast to edge dislocations in symmetrical diffraction, the contribution of screw dislocations to intensity distribution in GID is infinitesimal and can be neglected. It follows that we can measure, simulate and compare RSMs in GID. Hereby we find out the densities of pure edge TDs and then we consider them fixed in simulation of RSMs in symmetrical diffraction.

The best fit of the experimental and calculated maps in $10\bar{1}0$ and $11\bar{2}0$ diffrac-

tions are depicted on Fig. 7.7. All maps exhibit the central narrow maxima and wide diffuse parts. The size of the maximum $\sigma_1 \times \sigma_2$ corresponds to the coherently irradiated intensity and its width is inversely proportional of the coherently irradiated area at the sample surface.

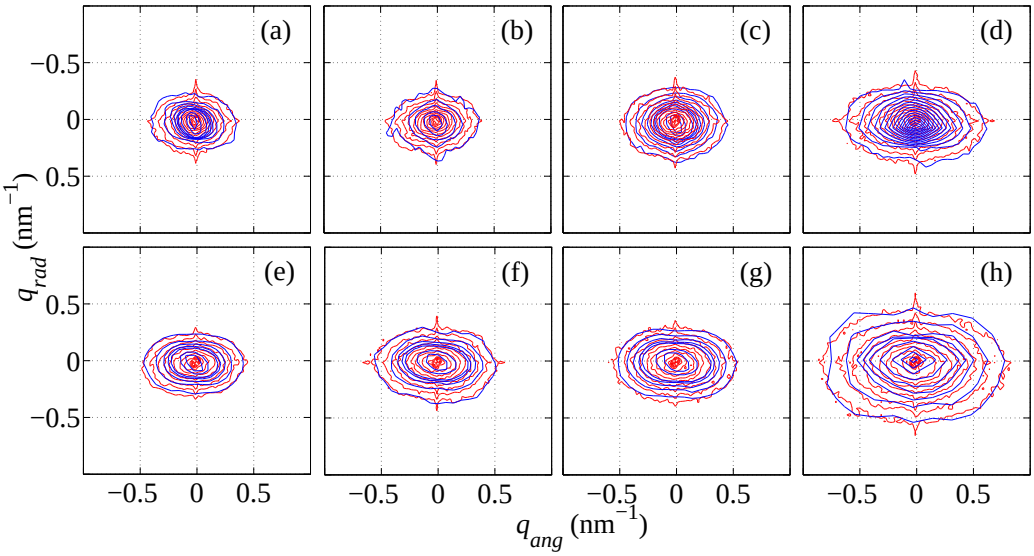

Figure 7.7: Measured (blue) and simulated (red) reciprocal space maps in $10\bar{1}0$ (panels a-d) and $11\bar{2}0$ (panels e-h) diffractions of: (a,e) - S1, (b,f) - S2, (c,g) - S3, and (d,h) - S4 samples. The intensity step is $10^{0.25}$ in logarithmic scale.

The densities of edge TDs determined from GID possess higher accuracy then the same ones obtained from asymmetrical diffraction (about 10%). Substituting them into input data for 0004 maps simulation we reduce the error in screw TDs determination.

7.3.3 The intensity profiles comparison

In order to compare the measured and simulated intensity distributions in details and to determine the effect of particular dislocation types, we analysed their cuts along both axes of RSM (Fig. 7.8, 7.9). From log-log representation of these cuts we obtained the slopes in the asymptotic dependences:

$$\begin{aligned} I(q_x, 0) \propto |q_x|^{-n} \quad , \quad I(0, q_z) \propto |q_z|^{-n}, \\ I(q_{ang}, 0) \propto |q_{ang}|^{-n} \quad , \quad I(0, q_{rad}) \propto |q_{rad}|^{-n} \end{aligned} \tag{7.8}$$

for coplanar and grazing-incidence geometries, respectively. To avoid possible influence of the crystal truncation rod in symmetrical diffraction, we extracted the linear intensity distributions along q_z for a small non-zero value of q_x.

From discussion published in [3] it follows that the slopes of the asymptotic dependence $I(q_x, 0)$ are $n = 4$ for screw and $n = 3$ for edge TDs. In our analysis they lie between 2 and 3. The difference can be explained by the q_y-integration included in our experimental resolution function.

In symmetrical geometry the diffraction curves $I(q_x, 0)$ follow rather q_x^{-3} dependences. It means that mostly screw threading dislocations contribute to the intensity distribution [141]. In the asymmetrical case the slopes are between 2 and

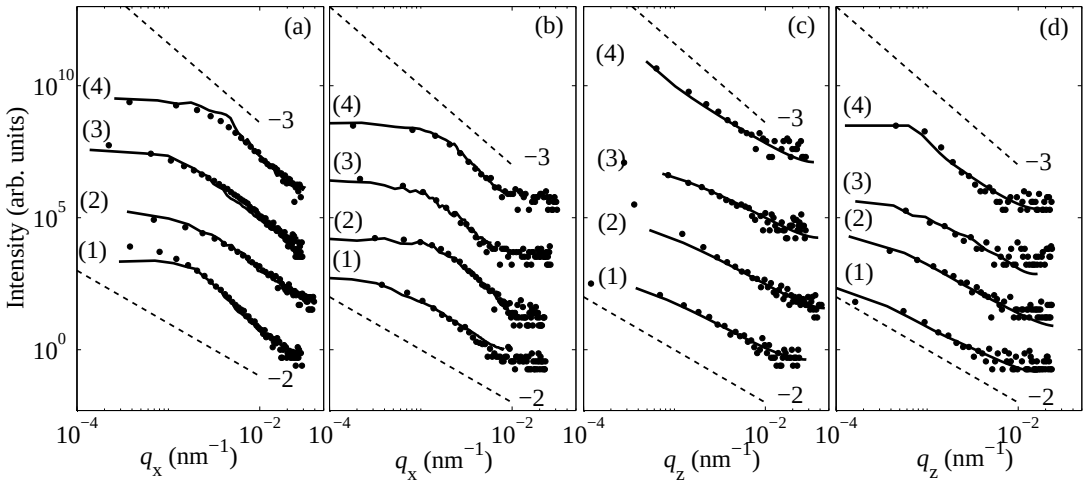

Figure 7.8: Experimental (dots) and simulated (solid lines) angular (a,b) and radial (c,d) cuts in 0004 (a,c) and $10\bar{1}4$ (b,d) diffractions for all samples.

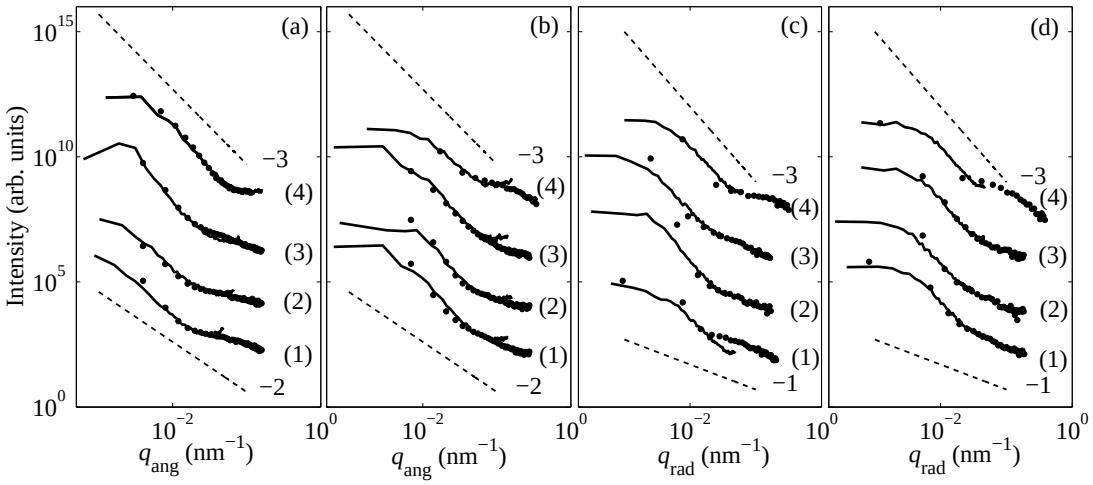

Figure 7.9: Experimental (dots) and simulated (solid lines) angular (a,b) and radial (c,d) cuts in $10\bar{1}0$ (a,c) and $11\bar{2}0$ (b,d) diffractions for all samples.

3, since both screw and edge components contribute to the scattered intensity. The closer a diffraction curve approximates to the q_x^{-3}, the more screw TDs are presented within the sample. And on the contrary the q_x^{-2} asymptotic behaviour indicates the prevailing type of edge TDs.

The asymptotic intensity decay along the q_z axis is not as well pronounced. It is seen that for different samples it varies roughly between q_z^{-1} and q_z^{-3}. Both from the experimental data and from our simulations it follows that the width of the diffraction maxima along the q_z axis are almost independent of the dislocation density. On the other hand, the dislocation density affects the slope of the q_z-dependence. Increasing of dislocation density leads to the slope increases from 1 (for sample S1) to 3 (for sample S4). This fact can be used as a rough estimation of the dislocation density.

The similar slopes behaviour is observed in GID. In the angular direction, the asymptotic tails of the diffraction curves drop as q_{ang}^{-2}-q_{ang}^{-3}. In the radial direction

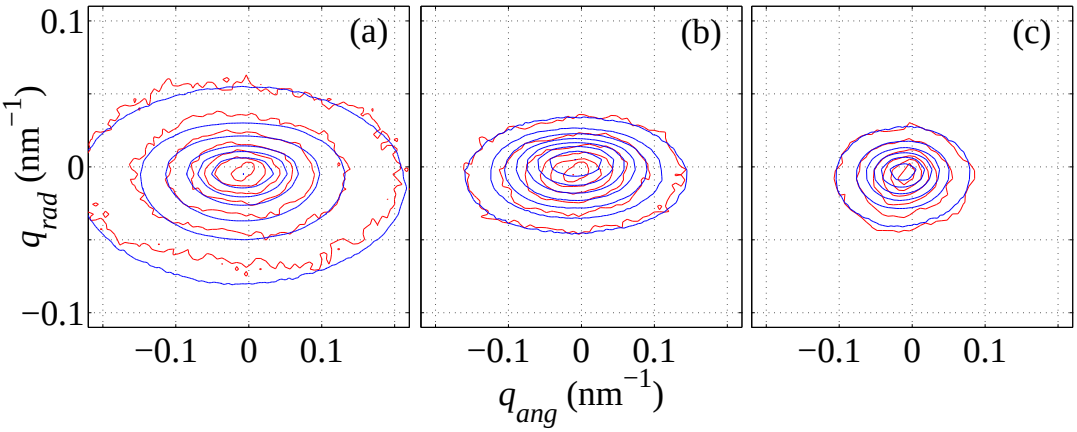

Figure 7.10: Measured (blue) and simulated (red) $10\bar{1}0$ RSMs of: (a) - A1, (b) - A3, and (c) - A5 samples.

the slope of the asymptotic part depends on the density of the edge dislocations. The lower dislocation density, the higher the slope is, ranging from q_{rad}^{-1} to q_{rad}^{-3}.

7.4 Monte Carlo simulation in c-plane $Al_{0.2}Ga_{0.8}N$

Our developed method can be used not only to GaN layers. The condition for its application is that the dislocations in the material should be perpendicular to the sample surface. A good example of such material is AlGaN heteroepitaxial layer grown of sapphire substrate.

A series of 5 c-plane $Al_{0.2}Ga_{0.8}N$ samples was grown by our colleagues from Ulm University (see Sec. 3.3.1). The samples differed in AlGaN layer thicknesses from 0.5μm for the thinnest to 3.5μm for the thickest one. The goal of our study is to determine the density of TDs and to figure out its dependence on the layer thickness.

7.4.1 Reciprocal space maps calculation

In order to solve the problem mentioned above we decided to apply our developed method based on Monte Carlo simulation [159]. However, it is necessary to note that the bundling of edge TDs revealed by TEM (see Fig. 3.8) creates the limitations for application of our method. In our model, the dislocation lines are considered to be perpendicular to the sample surface, which is true only in the near-surface region. Therefore we can combine our simulations with grazing-incidence diffraction technique probing the top of the main layer of the AlGaN film, while the RSMs in the asymmetrical diffraction that contain the integrated signal over the whole layer thickness cannot be used within our model.

The lattice parameters of two AlGaN phases were determined for each sample by S. Lazarev from symmetrical and asymmetrical coplanar diffraction measurements [153, 160]. The average parameters used in our calculations are the following: a_{main}=0.3177nm, a_{bottom}=3.1788nm; c_{main}=0.5154nm, c_{bottom}=5.1587nm.

We started from determination of the edge TDs densities in the near-surface region of the overgrown AlGaN layer. In our GID experiment, the penetration

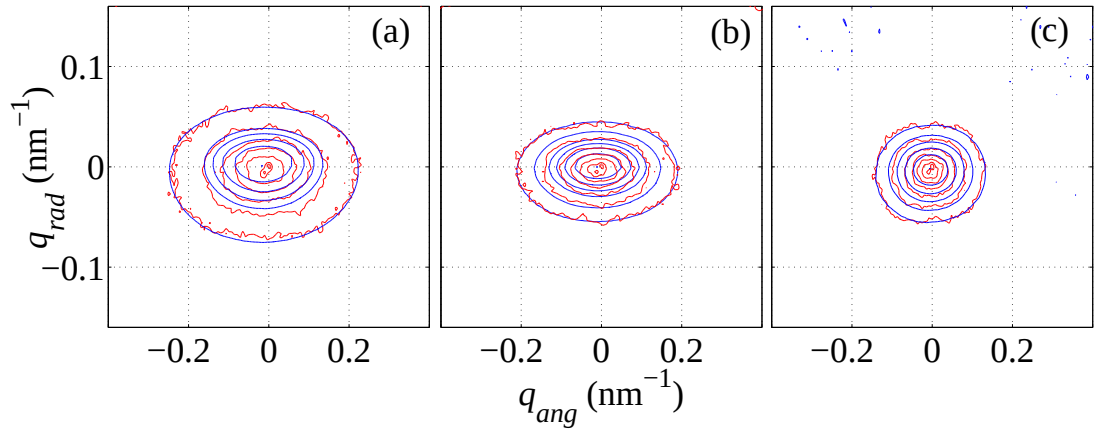

Figure 7.11: Measured (blue) and simulated (red) $11\bar{2}0$ RSMs of: (a) - A1, (b) - A3, and (c) - A5 samples.

depth was estimated to be less than 150nm meaning that the x-ray beam probed solely the near-surface region of AlGaN films. In our calculations, we neglected the presence of the bottom layer and for each sample we simulated RSMs in two $10\bar{1}0$ and $11\bar{2}0$ GID reflections. We did not include the influence screw dislocations due to surface relaxation effect and correlation in positions of edge dislocations in our calculation. The simulated RSMs were convoluted by resolution function to achieve a finite experimental resolution. The resolution function was selected as two-dimensional Gaussian with $\sigma \approx 0.02\text{nm}^{-1}$ corresponding to the coherently irradiated area of the sample surface estimated for our experimental setup. The similar procedure for GaN films is described in Sec. 7.2.

Our next step was to determine the density of screw TDs in the samples. In our model the expressions for displacement field caused by extended defects include surface relaxation, therefore edge dislocations play an important role in general intensity distribution in case of symmetrical diffraction [148]. The densities of edge TDs obtained from GID correspond to the overgrown layer of AlGaN. They were taken as fixed parameters for symmetrical RSMs simulations. For 0002 diffraction we did not take into account AlGaN peak splitting that is revealed only at high-order reflexes. We neglected the contributions of AlN interlayer as well as GaN phase into intesity distribution. AlN and GaN rich peaks are shifted with respect to the AlGaN peak in q_z direction so they have almost no impact on diffuse part scattered from AlGaN. In our simulations, we included the crystal truncation rod but omitted the monochromator streak. However, the intensity distribution along the CTR is strongly affected by oscillations from AlN and AlGaN 150nm layer. Therefore our main issue in symmetrical diffraction was to reproduce the intensity levels of AlGaN peak mainly in q_x direction. As a result of the RSMs simulation in 0002 symmetrical diffraction, we obtained an averaged density of screw TDs attributed to both main and 150 nm layers of AlGaN.

The 0008 RSMs consists of two signals coming from two AlGaN layers. They were simulated independently and then the intensity distributions were superposed. The densities of edge TDs known from GID were included as a fixed parameter in the main AlGaN layer simulation. The bottom layer of AlGaN is not affected by the surface relaxation so the density of screw dislocations was

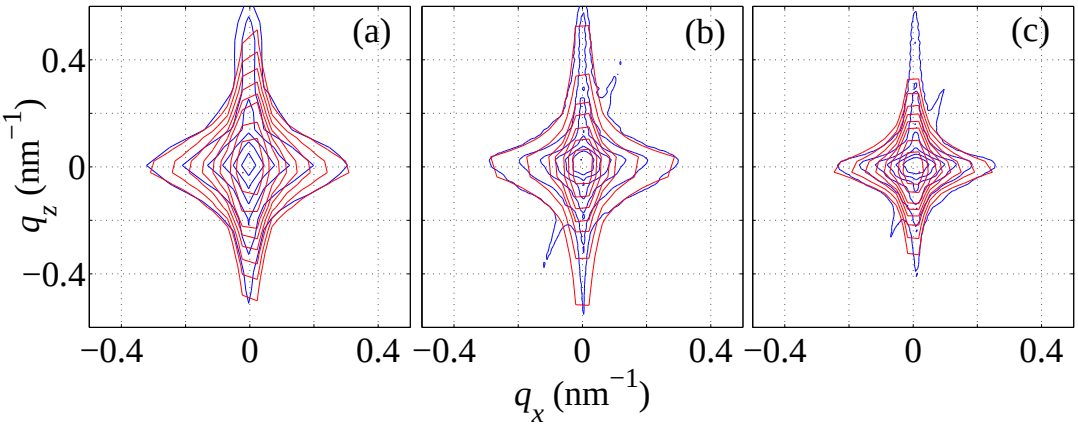

Figure 7.12: Measured (blue) and simulated (red) 0002 RSMs of: (a) - A1, (b) - A3, and (c) - A5 samples.

taken as a single parameter responsible for the diffuse scattering from this region. Varying the densities of screw dislocations we achieved the best agreement between experimental and simulated RSMs and thus we determined the densities of screw TDs in both layers. We required the best agreement between experimental and simulated maps in the diffuse part as well as the coincidence the amplitudes of the main peak.

7.4.2 Reciprocal space maps and intensity profiles comparison

The comparison of experimental and simulated GID RSMs are shown at Fig. 7.10 and 7.11. The notation q_{ang} corresponds to $[1\bar{2}10]$ direction, whereas q_{rad} coincides with the direction of the diffraction vector. On $11\bar{2}0$ experimental RSMs one can see an asymmetry in radial direction. This asymmetry cannot be affected by the misfit dislocations located at the interface because of relatively large thickness of the AlGaN layer with respect to the penetration depth in GID. Moreover HRTEM investigation on growth interrupted AlGaN deposited on SiN_X interlayers has confirmed the large density of TDs, while the MDs were hardly observed. The most probable explanation of this fact is non-constant concentration of Al in the AlGaN alloy. This effect has no influence on TDs density determination, nevertheless for detailed analysis we required good fitting of experimental and simulated maps in angular direction.

The comparison of coplanar maps in 0002 and 0008 diffractions are presented in Fig. 7.12 and 7.13 respectively. The parts of experimental RSMs that belong to pure GaN phase were out of our interest, therefore one can observe some disagreement in experimental and calculated maps in that region.

We compared cuts over the intensity maxima along q_x and q_{ang} directions on symmetrical and GID maps respectively (see Fig. 7.14). For symmetrical 0008 diffraction we compared the cuts over the main and the bottom peaks. Some disagreement is found in the coherent part of the bottom peak. It is attributed to influence of GaN phase that was neglected in our simulations.

The asymptotic behaviour of profiles in symmetrical diffraction obeys $q_x^{-2}-q_x^{-3}$

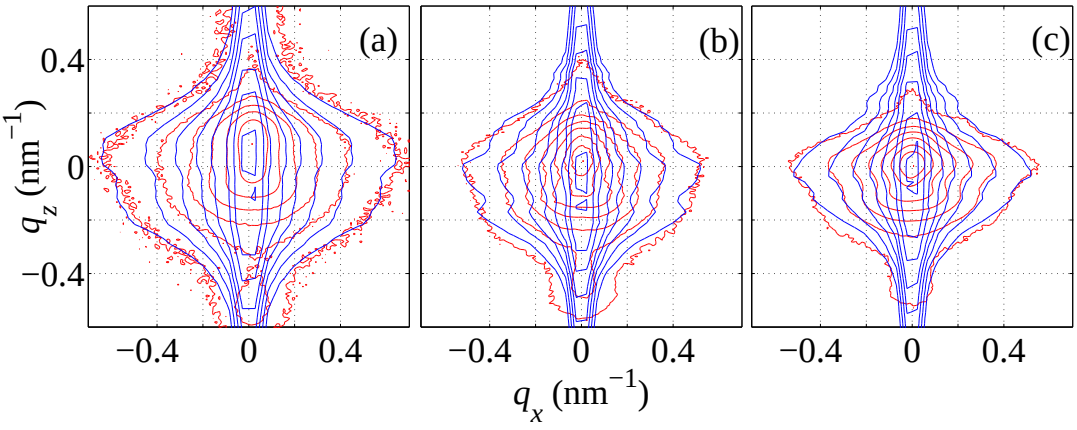

Figure 7.13: Measured (blue) and simulated (red) 0008 RSMs of: (a) - A1, (b) - A3, and (c) - A5 samples.

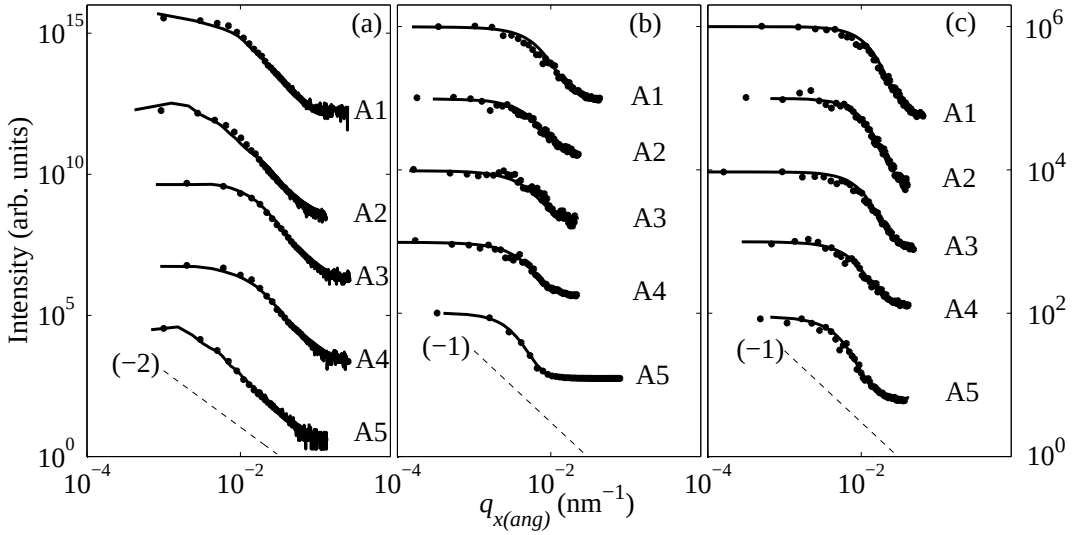

Figure 7.14: Experimental (dots) and simulated (solid lines) angular cuts in 0002 (a), $10\bar{1}0$ (b) and $11\bar{2}0$ (c) diffractions for all samples. The number of samples are indicated.

lows, which indicates a presence of both, screw and edge types of dislocations. In GID, the tales of curves decay as $q_{ang}^{-1} - q_{ang}^{-2}$ due to large number of edge TDs [141].

8. X-ray measurements of a-plane GaN layers.

8.1 Measurements of a-plane GaN films

A-plane GaN with the (11-20) surface orientation is very useful in various technological applications. The main its advantage is the absence of the quantum confined Stark effect typical for c-oriented material [30]. However, a-plane GaN layers possess a large number of defects, especially stacking faults, so that a reliable method for the determination of the defect densities is of high importance.

The object of our investigation is a series of 4 non-polar a-plane oriented GaN epitaxial layers grown on the r-oriented sapphire template by MOVPE technique (See Sec.3.3.2). We selected non-destructive x-ray diffraction as a tool of our investigation and combined it with Monte Carlo method of diffuse scattering simulation.

8.1.1 Noncoplanar Bragg diffraction as a tool of SFs detection

In a-plane GaN, two types of stacking faults have been reported in literature [31, 145], namely basal-plane (or basal) SFs and prismatic SFs.

The prismatic SFs with the displacement vectors $\boldsymbol{R} = \frac{1}{2}\langle 10\bar{1}1\rangle$ are located along $\langle \bar{1}2\bar{1}0\rangle$ planes. The energy of prismatic SFs activation is relatively high [33], their densities in GaN are estimated of order 10^2 cm^{-1}. In general, they are almost not detectable by methods based on x-ray diffraction and we can neglect their presence in our samples.

The SFs in the (0001) basal planes give rise to a narrow streak in reciprocal space along [0001]. For the determination of the SF density it is necessary to measure the intensity distribution along this streak. Therefore the [0001] direction must be parallel to the scattering plane, in which the wave vectors $\boldsymbol{K}_{i,f}$ of the primary and scattered waves lie. In a coplanar scattering geometry the

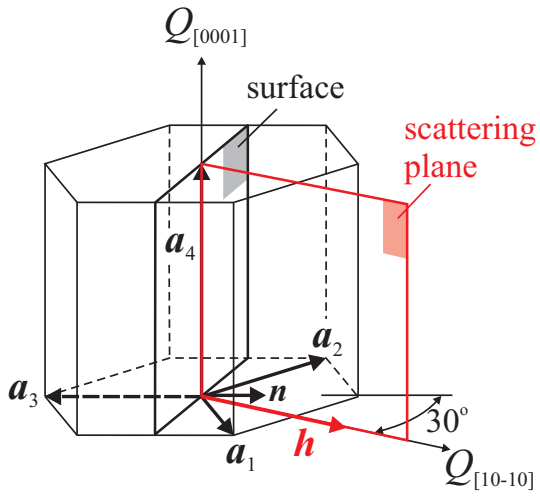

Figure 8.1: The sketch of the elementary unit cell of wurtzite GaN with the orientation of the a-plane (grey) and scattering plane (red). The scattering plane makes an angle of 30 deg with the surface normal $\boldsymbol{n}$. The picture is taken from [32].

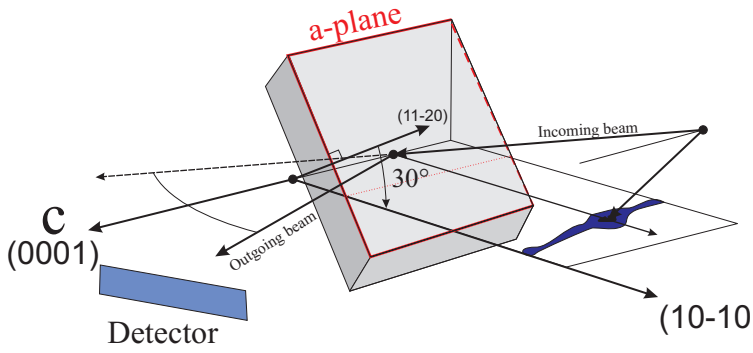

Figure 8.2: The scheme of symmetrical non-coplanar measurements at rotating anode.

scattering plane is perpendicular to the sample surface, i.e. to $(11\bar{2}0)$ plane in case of a-plane GaN. All coplanar diffractions in this scattering plane are of the type $11\bar{2}L$, however, all basal-SFs do not produce any diffuse scattering in these diffractions. Therefore we used an inclined geometry (see Fig. 8.1) in which the scattering plane makes an angle of 30 deg with the surface normal $\boldsymbol{n} = \frac{1}{3}[11\bar{2}0]$ and symmetric diffractions $H0\bar{H}0$.

The criterion used in TEM for stacking faults visibility can be applied in x-ray diffraction [161]:

$$\boldsymbol{h} \cdot \boldsymbol{R} \neq n, \tag{8.1}$$

where $\boldsymbol{h}$ is vector of diffraction, $\boldsymbol{R}$ is the SFs displacement vector and n is integer including zero. The condition 8.1 makes it easier to select appropriate diffractions in order to detect SFs with known displacement vectors.

8.1.2 Experimental setup

The x-ray diffraction experiments were performed in Institute of Semiconductor and Solid State Physics (Johannes Kepler University, Linz, Austria). The diffractometer was equipped by custom-built rotating-anode setup with a small focus (Cu anode, 2 kW output). A double-bent parabolic multilayer mirror and a Ge(220) channel cut monochromator were used to produce a well-collimated beam of CuKα_1 radiation with the divergences of about 12 arcsec and less than 0.1 deg in the scattering plane and across it respectively. The primary beam was shaped by slits down to the cross-section of 1×1 mm^2, the source-sample distance was about 1.6 m. For data collection a vertically oriented linear multichannel detector with the pixel size of about 50 μm at a distance of 0.8 m to the sample was used. The scheme of our setup is drawn on Figure 8.2.

The inclined geometry was the reason for the collimation of the primary beam in two orthogonal directions described above. For each sample we measured RSMs in diffractions $H0\bar{H}0$ with $H = 1, 2, 3$. In our experimental setup, a linear detector enabled fast data acquisition. It was necessary to perform only one rocking scan to record a reciprocal-space map.

The resolution in reciprocal plane is determined by the divergence of the primary x-ray beam both in the scattering plane and perpendicular to it by the pixel size of the detector and its distance from the sample. For the experimental conditions listed above we achieved a resolution better than 0.05 nm^{-1} for all measured diffractions in both directions in the scattering plane.

All the measured Bragg peaks were broader than expected from the instrumental broadening. The experimental broadening can therefore be neglected in

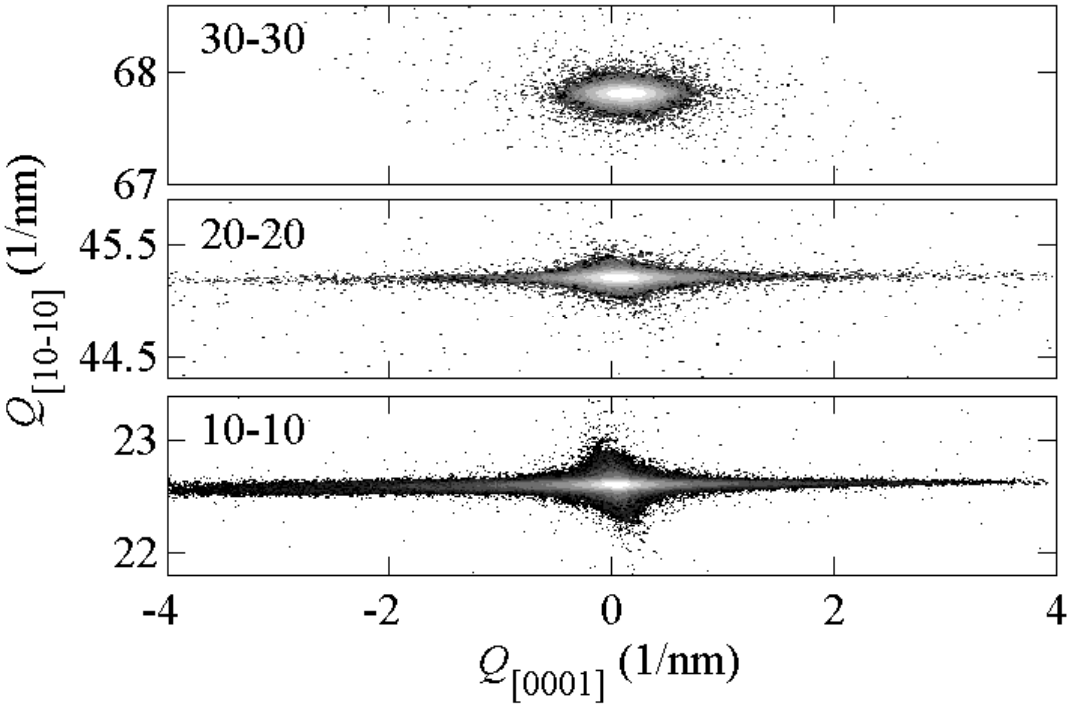

Figure 8.3: Examples of the reciprocal space maps of x-ray diffuse scattering measured in the symmetric non-coplanar diffractions $10\bar{1}0$, $20\bar{2}0$ and $30\bar{3}0$ of the sample M3. The data are plotted in a logarithmic scale, the step of the iso-intensity levels is $10^{0.5}$. The picture is taken from [32].

the further analysis. Moreover, since we are interested in the shape of the peaks far from the sharp central peak, the resolution function does not influence our analysis.

8.1.3 Results of measurements

Figure 8.3 displays the RSMs of sample M3 measured in diffractions $10\bar{1}0$, $20\bar{2}0$, and $30\bar{3}0$; the RSMs of other samples are similar. The [0001]-oriented streak is visible in $10\bar{1}0$ and $20\bar{2}0$ diffractions, while the diffraction maximum in $30\bar{3}0$ is rather round. According to the theory listed in Sec.5, this feature indicates the presence of basal SFs.

To determine the density of SFs, from the RSMs we extracted intensity scans along the [0001]. We tested several procedures for extraction: a cut along SF-streak, an integration over $[10\bar{1}0]$ direction of the whole RSM etc. However, the best way was to integrate the measured RSM in a narrow stripe of the width $\Delta Q_{[10\bar{1}0]} = 0.1\ \mathrm{nm}^{-1}$ around the maximum. This integration effectively suppresses the experimental noise. The extracted scans for sample M3 are plotted in Fig. 8.4. The inset shows the intensity maxima in detail. From the inset it follows that the FWHM of the $20\bar{2}0$ and $30\bar{3}0$ are almost identical. That means the FWHM is affected mainly by a limited coherence of the primary beam, by other effects such as limited angular resolution of the detector and diffuse scattering from dislocations but not by the diffuse scattering from the SFs. Figure 8.4 demonstrates that the extracted intensity scans are slightly asymmetric, this

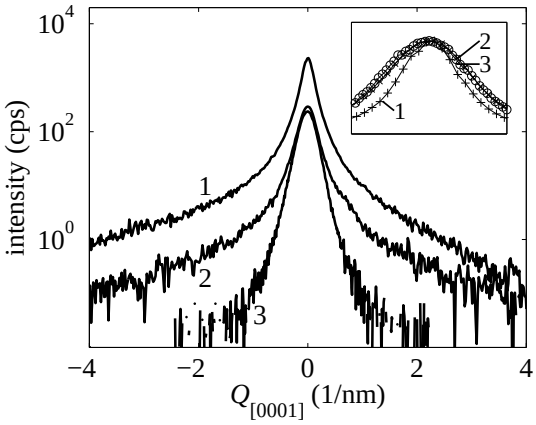

Figure 8.4: Linear scans in [0001] direction (i.e. along the SF-streak) extracted from the RSMs in Fig. 8.3. The inset shows the details of the scan around the maximum, normalized to maximum intensity. The numbers denote the orders H of the diffractions $H0\bar{H}0$.

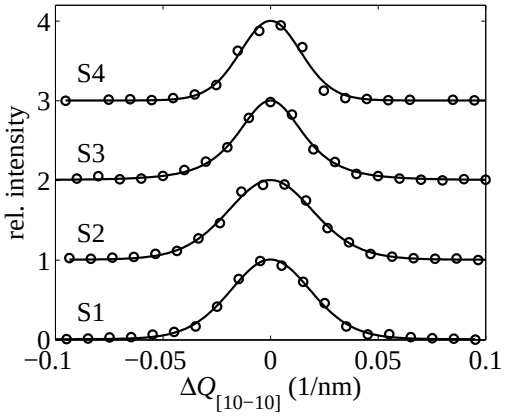

Figure 8.5: Linear scans in $[10\bar{1}0]$ direction (i.e across the SF streak) extracted from the RSMs of all samples in diffraction $10\bar{1}0$ for $Q_{[0001]} = 2$ nm^{-1} (dots) as well as their fits by Gaussian functions (lines). The scans are shifted vertically for clarity.

asymmetry is stronger for smaller H. This effect is of purely geometrical nature. For $Q_{[0001]} < 0$ the irradiated sample volume (and consequently the number of irradiated SFs) is larger than for $Q_{[0001]} > 0$. We included this effect in the intensity simulations by multiplying the intensity by the factor $1/\sin(\alpha_i)$, where α_i is the variable incidence angle of the primary x-ray beam.

We have also extracted scans across the SF streaks at $Q_{[0001]} = 2$ nm^{-1}. Figure 8.5 displays these scans for all samples in diffraction $10\bar{1}0$ and their fits by Gaussian functions. From the FWHM of these scans we determined the effective sizes S_{eff} of the SFs. These values represent the lower limits of the true lateral sizes S of SFs, since the linear scans are considerably broadened by the experimental resolution.

9. Method for stacking faults densities determination in a-plane GaN layers

9.1 Theoretical model

It is well-established nowadays that wurtzite a-GaN epitaxial layers contain a large amount of planar defects (stacking faults) in addition to dislocations of various types [22, 31, 144]. Three types of intrinsic (I1, I2 and I3) as well as one type of extrinsic (E) basal SFs occur in (0001) planes. Except them prismatic SFs in planes $\frac{1}{2}\{10\bar{1}1\}$ are also reported in the literature. However, the density of prismatic SFs in a-GaN material is relatively low [145]. In our work, we restrict ourselves to the most common basal SFs I1-I3 and E. The stacking of the (0001) basal planes in these defect types is displayed in Fig. 2.6.

Based on diffuse x-ray scattering and Monte Carlo approach V. Holý developed a theory enabling to determine the densities of basal stacking faults in a-plane GaN layers [32]. In contrast to the methods mentioned in Sec. 5.2.5, in our approach we analyse not only the widths of the diffraction peaks but also full shapes of the maxima in reciprocal space. It enables to distinguish the peak broadening due to SFs from the contribution of other defects. The full shape of the diffraction maximum makes it possible to determine not only the density but also the prevalent type of the SFs. However, as we show later, this task requires to measure the diffracted intensity very far from the diffraction maximum that was not measured due to the limitations of the diffractometer.

9.1.1 Mathematical description of stacking faults

Developing the formula for the intensity scattered from a random sequence of SFs we assume that the GaN layer diffracts kinematically, i.e. effects of dynamical x-ray diffraction including absorption and refraction are fully neglected. This simplification is fully justified if two conditions are valid:

- the GaN layer is much thinner than the x-ray extinction length in GaN (about 3 μm in diffraction $20\bar{2}0$ and CuKα_1 radiation) or the angular deviation from the diffraction maximum is larger than the width of the intrinsic Darwin curve;
- the incidence and/or exit angles of the x-ray beams are much larger than the critical angle of total external reflection (0.33 deg for CuKα_1).

The far-field limit approximation is validity, if the size of the coherently irradiated sample area (below 1 μm in a our experimental arrangement) is much smaller than the diameter of the first Fresnel zone. The positions of individual SFs are assumed random and the irradiated sample volume contains a large number of defects so that the measured x-ray signal can be considered averaged over a statistical ensemble of all configurations of the SFs.

If we have a perfect layer without any structural defects, the amplitude of the wave diffracted from the layer is a function of the scattering vector $\boldsymbol{Q} = \boldsymbol{K}_f - \boldsymbol{K}_i$, where $\boldsymbol{K}_f$ and $\boldsymbol{K}_i$ are the wave vectors of the diffracted and primary beams respectively. Using the kinematical approximation and the far-field limit introduced above, this amplitude can be written as

$$E(\boldsymbol{Q}) = A\left[f_{\mathrm{Ga}}(Q) + f_{\mathrm{N}}(Q)e^{-i\boldsymbol{Q}\cdot\boldsymbol{d}}\right]\sum_{\boldsymbol{n}} e^{-i\boldsymbol{Q}\cdot\boldsymbol{R}_{\boldsymbol{n}}}. \tag{9.1}$$

Here we denoted $f_{\mathrm{Ga,N}}$ the form-factors of atoms Ga and N, and $\boldsymbol{d} = 3\boldsymbol{a}_4/8$ is the position vector of the N atom with respect to Ga in a GaN molecule. $\boldsymbol{n} \equiv (n_1, n_2, n_3)$ are the indexes of a GaN molecule with the position vector $\boldsymbol{R}_{\boldsymbol{n}}$. The hexagonal basis vectors are $\boldsymbol{a}_{1,2,4}$, the vectors $\boldsymbol{a}_{1,2}$ and $\boldsymbol{a}_3 = -\boldsymbol{a}_1 - \boldsymbol{a}_2$ lie in the basal plane (0001) and $\boldsymbol{a}_4$ is orthogonal to it (see Fig. 8.1). A is a constant containing the amplitude of the primary beam, the classical electron radius, and the polarization factor, among others.

Since two GaN molecules constitute one GaN elementary unit cell, the molecule position vectors can be presented in such way:

$$\boldsymbol{R}_{\boldsymbol{n}} = n_1\boldsymbol{a}_1 + n_2\boldsymbol{a}_2 + n_3\boldsymbol{a}_4/2 + \sigma_{n_3}\boldsymbol{p}, \tag{9.2}$$

where $\boldsymbol{p} = \frac{2}{3}\boldsymbol{a}_1 + \frac{1}{3}\boldsymbol{a}_2$ is the lateral shift of the second Ga-N bilayer in the elementary unit cell with respect to the first one; we denote these bilayers by Bb and Aa, respectively. The ideal hcp stacking of bilayers is therefore denoted as ...AaBbAaBb..., the fcc stacking of the bilayers would be ...AaBbCcAaBbCc... . Here, $n_3 \equiv \sigma_{n_3}\mathrm{mod}(2)$, i.e. σ_{n_3} equals 0 (1) for even (odd) values of n_3. It yields $\sigma_{n_3} = \sigma_{n_3-2}$. For a general stacking sequence of bilayers Aa, Bb and Cc, σ_{n_3} values create a general sequence of 0, 1 and 2. The case $\sigma_{n_3} = 3$ is equivalent to $\sigma_{n_3} = 0$, since $3\boldsymbol{p}$ is an integer linear combination of basis vectors $\boldsymbol{a}_{1,2}$. Therefore all the σ values are considered modulo 3.

For the layer that contains a single SF of type I1 in position $n_3 = n_{\mathrm{def}}$ the actual stacking sequence is then ...ABABCBCB... for n_{def} even or ...ABACACA... for n_{def} odd. We omitted the symbols abc for the N atoms in the unit cell. The corresponding sequences of the σ_{n_3} values are ...01012121... or ...0102020... . In both cases,

$$\sigma_{n_{\mathrm{def}}} \equiv (2\sigma_{n_{\mathrm{def}}-1} - \sigma_{n_{\mathrm{def}}-2})\mathrm{mod}(3). \tag{9.3}$$

Using the same procedure we find that the SF I2 in position n_{def} is described by the formulas

$$\begin{aligned} \sigma_{n_{\mathrm{def}}} &\equiv (2\sigma_{n_{\mathrm{def}}-1} - \sigma_{n_{\mathrm{def}}-2})\mathrm{mod}(3), \\ \sigma_{n_{\mathrm{def}}+1} &\equiv (2\sigma_{n_{\mathrm{def}}} - \sigma_{n_{\mathrm{def}}-1})\mathrm{mod}(3). \end{aligned} \tag{9.4}$$

The formulas for the type I3 are

$$\begin{aligned} \sigma_{n_{\mathrm{def}}} &\equiv (2\sigma_{n_{\mathrm{def}}-1} - \sigma_{n_{\mathrm{def}}-2})\mathrm{mod}(3), \\ \sigma_{n_{\mathrm{def}}+1} &\equiv \sigma_{n_{\mathrm{def}}-1}\mathrm{mod}(3), \\ \sigma_{n_{\mathrm{def}}+2} &\equiv (2\sigma_{n_{\mathrm{def}}+1} - \sigma_{n_{\mathrm{def}}})\mathrm{mod}(3). \end{aligned} \tag{9.5}$$

The SF of the extrinsic type (E) is described by

$$\begin{aligned} \sigma_{n_{\rm def}} &\equiv (2\sigma_{n_{\rm def}-1} - \sigma_{n_{\rm def}-2}) \mathrm{mod}(3), \\ \sigma_{n_{\rm def}+1} &\equiv (2\sigma_{n_{\rm def}} - \sigma_{n_{\rm def}-1}) \mathrm{mod}(3), \\ \sigma_{n_{\rm def}+2} &\equiv (2\sigma_{n_{\rm def}+1} - \sigma_{n_{\rm def}}) \mathrm{mod}(3). \end{aligned} \tag{9.6}$$

The stacking sequences of various SF types are represented graphically in Fig. 2.6, from which Eqs. 9.3-9.1.1 follow as well. From the figure it is seen that the SFs are represented by short fcc-like segments. In the case I1 the fcc segment contains one (0001) bilayer, in I2 and E the fcc segment consists of 2 and 3 bilayers respectively.

A given microscopic distribution of stacking faults is described by a certain sequence of the values of σ_{n_3}, from which the diffracted amplitude can be calculated

$$E(\boldsymbol{Q}) = \Phi(\boldsymbol{Q}) \sum_{n_3=0}^{N} \xi^{n_3} \kappa^{\sigma_{n_3}}, \tag{9.7}$$

where $\xi = e^{-i\boldsymbol{Q}\cdot\boldsymbol{a}_4/2}, \kappa = e^{-i\boldsymbol{Q}\cdot\boldsymbol{p}}$, and N is the number of coherently irradiated (0001) basal planes. In equation 9.7, $\Phi(\boldsymbol{Q})$ stands for

$$\Phi(\boldsymbol{Q}) = A\left[f_{\rm Ga}(Q) + f_{\rm N}(Q) e^{-i\boldsymbol{Q}\cdot\boldsymbol{d}}\right] \sum_{n_1,n_2} e^{-i\boldsymbol{Q}\cdot(n_1\boldsymbol{a}_1 + n_2\boldsymbol{a}_2)}. \tag{9.8}$$

The range of the double sum $\sum_{n_1,n_2}$ corresponds to the lateral size S of the stacking faults and we assume that this size is comparable to the layer thickness. Then, the function $\Phi(\boldsymbol{Q})$ gives rise to a narrow streak in reciprocal space along [0001], i.e. perpendicular to the SF planes (0001). The width of the cross-section of this streak can be estimated to $2\pi/S$ and it is usually comparable to the resolution limit of the experimental setup. Therefore it is enough to deal with the reciprocal-space distribution of diffracted intensity $I(Q_{[0001]})$ along the SF-streak.

The reciprocal-space distribution of the intensity stemming from one coherently irradiated volume is given by a convolution of the function $|E(Q_{[0001]})|^2$ with the resolution function $\Gamma(Q)$ of the experimental device

$$\begin{aligned} I(Q) &= \int dQ' |E(Q-Q')|^2 \Gamma(Q'), \\ \Gamma(Q) &= \int_{-\infty}^{\infty} dx \Gamma(x) e^{-iQx}. \end{aligned} \tag{9.9}$$

The resolution function is the Fourier transformation of the mutual coherence function of the primary radiation $\Gamma(x)$ in two points in the distance x along the [0001] direction. However, the numerical calculation of the integral in Eq. 9.1.1 is time consuming and we used the following approximative approach instead. We define the function $\Psi(x) = \sqrt{\Gamma(x)}$ and the final equation for intensity distribution can be rewritten as follows:

$$\begin{aligned} E(\boldsymbol{Q}) &= \Phi(\boldsymbol{Q}) \sum_{n_3=0}^{N} \xi^{n_3} \kappa^{\sigma_{n_3}} \Psi(n_3 |\boldsymbol{a}_4|/2), \\ I(Q_{[0001]}) &= |E(Q_{[0001]})|^2. \end{aligned} \tag{9.10}$$

The function $\Psi(x)$ describes a broadening of the diffraction curve not only due to a limited coherence of the primary beam but also due to other effects such as limited angular resolution of the detector and diffuse scattering from other defect types, like dislocations. The form of this function can be determined from the diffraction curve measured around the reciprocal lattice point $\boldsymbol{h}$, where the SFs do not produce any diffuse scattering.

In the simulations we assumed that the function $\Psi(x)$ can be described by the well-known PearsonVII distribution function [162]

$$\Psi(x) = \left[1 + 4(2^{1/\alpha} - 1)\left(\frac{2x}{W}\right)^2\right]^{-\alpha}, \tag{9.11}$$

where W is the FWHM of the function and α is the shape parameter. For $\alpha \to \infty$ this function approaches the Gauss function, in the case of $\alpha = 1$ $\Psi(x)$ corresponds to the Lorentz function. The case $W \to \infty$ represents an ideally coherent and plane primary wave and no diffuse scattering from other defects (dislocations in particular). Decreasing W, the resulting diffraction curve changes its form and its FWHM increases. In order to discriminate the influence of this effect from the true intensity profile it is necessary to measure the intensity curves in various diffractions $H0\bar{H}0$.

The diffraction curve in $30\bar{3}0$ is not affected by the SFs at all, so from its form the parameters W and α of function $\Psi(x)$ can be determined. These values can be used for the analysis of diffraction curves in other diffractions. However, both the effect of transversal coherence and diffuse scattering from dislocations scale with the length of the diffraction vector $\boldsymbol{h}$. Therefore the FWHM W_H of the function $\Psi(x)$ in diffraction $H0\bar{H}0$ is

$$W_H = 3/H \times W_3, \tag{9.12}$$

where W_3 is the FWHM determined from diffraction $30\bar{3}0$. The shape parameter α does not depend on the diffraction order H.

9.1.2 Algorithm of calculation of the reciprocal space intensity distribution

The general strategy of Monte Carlo simulations for a-plane GaN is similar to one applied in case of c-plane layers as it was discussed in Sec. 7.2. However, since we are now interested in determination of SFs density, the algorithm is altered in accordance with the actual problem. The brief overview of simulation procedure is expounded below.

In a standard x-ray diffraction experiment, the irradiated sample volume is much larger than the coherence volume of the primary beam, so that the measured diffracted intensity is an incoherent superposition of intensities originating in various coherently irradiated volumes. In a coherently irradiated volume consisting of N (0001) Ga-N bilayers we define the positions and types of the SFs using a random generator.

For the definition of random positions of the SFs we assume that the sequence of the SFs of the same type creates a homogeneous Markov chain [163]. The distances D_n between the $n-1$-th and n-th SFs are expressed in integer multiples

of $|\boldsymbol{a}_4|/2 \equiv c/2$, where c is the vertical lattice parameter of wurtzite GaN, and they are assumed random and uncorrelated. In the simulations, we used the geometric distribution of the distances with the mean value $\langle D_0 \rangle = D_0$ and rms deviation $\sigma_D = \sqrt{\langle (D - D_0)^2 \rangle} = \sqrt{D_0(D_0 + 1)}$. For this distribution we obtained the best correspondence of the measured and simulated intensity profiles. We tried also the Poisson distribution, however, in this case we obtained broad but well-visible satellite maxima on the SF-streak with the mean distance of about $\Delta Q_{[0001]} = 2\pi/D_0$, which were not observed in our experimental data.

The geometric distribution is a discrete analog of the exponential distribution. The probability of finding the (dimensionless) distance D is $w(D) = p(1 - p)^D$, where the parameter p is the probability of finding the SF in a given position, connected with the mean value D_0 of D by $D_0 = (1 - p)/p$. The geometric distribution is the only discrete "memoryless" distribution, in which the probability of finding the SF in the given position does not depend on actual positions of other SFs [164].

We assumed that the mutual positions of the SFs of different types are statistically uncorrelated so that the total diffracted intensity is a sum of contributions of the Markov chains of various defect types.

From the positions and types of the SFs defined in the previous step we construct the sequence of σ's using Eqs. 9.3-9.1.1. The amplitude of the diffracted wave and the diffracted intensity are calculated directly according to Eq. 9.1.1. The generation of SFs and subsequent computation of the diffracted intensity I_j are repeated M times. Each intensity distribution I_j corresponds to the intensity scattered for a single coherently irradiated volume, M is the number of these volumes in the irradiated sample volume.

Finally we calculate the average intensity profile

$$I(Q_{[0001]}) = \frac{1}{M} \sum_{j-1}^{M} I_j(Q_{[0001]}) \tag{9.13}$$

and the root-mean-square (rms) deviation σ_I of the average intensity (see Eq. 7.7)

The number of configurations M is chosen so that the maximum of $\sigma_I(Q_{[0001]})$ did not exceed 5%. The resulting computation time was few minutes for a scan of about 10^3 values of $Q_{[0001]}$.

9.1.3 Possibility to distinguish between types of stacking faults with x-ray diffuse scattering

We have performed an extensive series of simulations for various defect types and densities and for various diffractions $\boldsymbol{h} = H0\bar{H}0,\ H = 1, 2, 3$ in symmetrical inclined scattering geometry. In diffraction $H0\bar{H}0$ the factor κ occurring in Eq. 9.7 and 9.1.1 for diffracted intensity is $\kappa = e^{-4\pi i H/3}$, which equals $(-1 \pm i\sqrt{3})/2$ for $H = 1, 2$, respectively and $\kappa = 1$ for $H = 3$. Therefore in diffraction $\boldsymbol{h} = 30\bar{3}0$ the SFs of all types do not produce diffuse scattering. The broadening of the diffraction maximum along the SF-streak is caused either by experimental resolution or by diffuse scattering from other defect types. Thus, the $30\bar{3}0$ diffraction can be used for the determination of the function $\Psi(x)$ defined above.

It is worthy to note that in asymmetrical coplanar diffractions $11\bar{2}L$ $\kappa = 1$ holds as well, so that these diffractions are not suitable for the measurement. The condition of the "visibility" of a basal SF is $\kappa \neq 1$ is equivalent to the condition $\boldsymbol{h} \cdot \boldsymbol{R} \neq n$ (see Eq. 8.1), where $\boldsymbol{R}$ is the stacking fault displacement vector and n is integer [22, 161]. In the sum $\sum_{n_3}$ for the diffraction amplitude, the

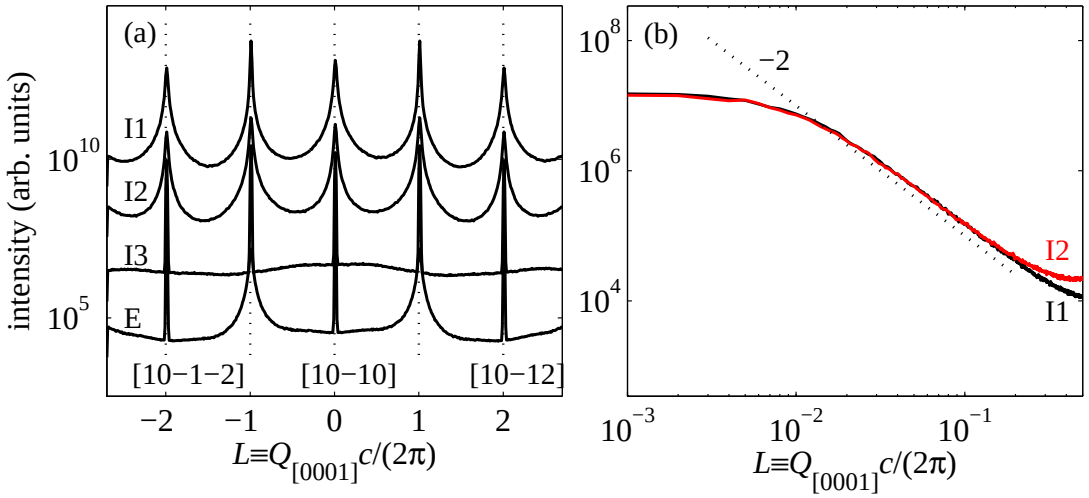

Figure 9.1: (a) Intensity distributions along the SF-streak calculated in diffraction $10\bar{1}0$ for various types of the SFs and the same mean distance $D_0 = 50$ between the SFs; the curves are shifted vertically for clarity and an ideally coherent primary beam was assumed ($W \to \infty$). Diffraction maxima along the $[10\bar{1}L]$ rod are indicated by vertical dotted lines. (b) Detail of the diffraction maximum of defects I1 and I2 in log-log scale, the dotted line represents the slope -2.

segments with $\kappa^{\sigma_{n_3}} = (-1 + i\sqrt{3})/2$ and $(-1 - i\sqrt{3})/2$ appear in average with the same occurrence for $H = 1$ and $H = 2$. Therefore the intensity distributions in diffractions $10\bar{1}0$ and $20\bar{2}0$ differ only due to different values of atomic form-factors $f_{\mathrm{Ga,N}}(Q)$. Fig. 9.1 presents the intensity distributions along the SF-streak calculated for different SF types depicted in Fig. 2.6. In the simulations we used the same mean distance between the fault planes $D_0 = 50$ (expressed in mutliples of $c/2$) and we put $\Psi(x) = 1$, i.e. we assumed a perfectly plane incident wave and no diffuse scattering from other defect types. Fig. 9.1 displays the intensity distributions calculated along the $[10\bar{1}L]$ rod crossing also the diffraction maxima $[10\bar{1}\bar{2}]$, $[10\bar{1}\bar{1}]$, $[10\bar{1}1]$ and $[10\bar{1}2]$.

From the Fig. 9.1(b) it follows that the shapes of the diffuse scattering maxima from the defects of types I1 and I2 are almost identical in the vicinity of the reciprocal lattice points and these defect types can be distinguished only from the intensity distributions around the anti-Bragg points $L = n + \frac{1}{2}$. Close to a reciprocal lattice point, the intensities from both defect types are proportional to $Q_{[0001]}^{-2}$. This behaviour follows from the geometric distribution of the SF distances. From Fig. 2.6 it is obvious that the sequence ...ABAB... is inverted to ...CBCB... in the case of I1, and the sequence ...ABAB... is shifted to ...CACA... for I2. This inversion or shift of the lattice gives rise to a shift in phase of the scattered wave and the diffuse scattering along the SF-streak is produced by the interference of the phase-shifted waves originating from various hcp segments divided by the SFs. On the other hand, in the case of the I3 defect, the hcp

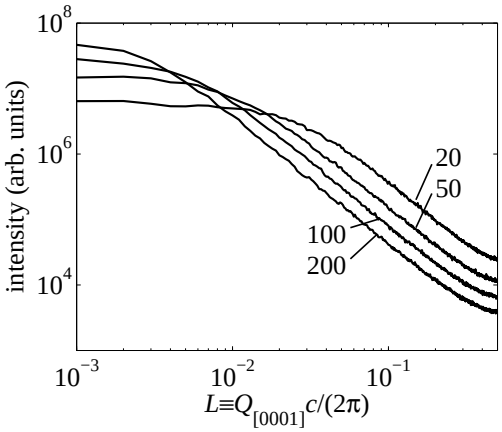

Figure 9.2: Intensity distributions along the SF-streak calculated in diffraction $10\bar{1}0$ for various mean distances D_0 expressed in integer multiples of $c/2$. Ideally coherent primary beam was assumed ($W \to \infty$).

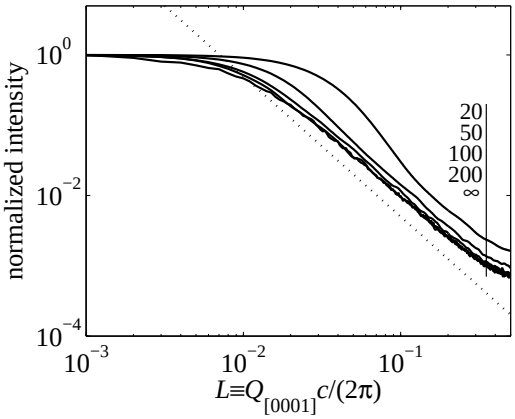

Figure 9.3: Intensity distributions along the SF-streak calculated in diffraction $10\bar{1}0$ for various widths W of the function $\Psi(x)$ expressed in integer multiples of $c/2$ and constant $D_0 = 50$. The dotted line represents the slope -2.

segments on both sides of the defect are in phase. Therefore diffuse scattering from I3 is caused only by pairs of very narrow fcc segments connected to each fault plane. This is the reason, why the intensity distribution along the $[10\bar{1}L]$ rod does not exhibit any maximum around the reciprocal lattice point (see Fig. 9.1(a)). In the case of defects E, the diffuse scattering along the $[10\bar{1}L]$ rod is concentrated around every second reciprocal lattice point, i.e. $[10\bar{1}\bar{3}], [10\bar{1}\bar{1}], [10\bar{1}1], [10\bar{1}3]$ etc.

The width of the intensity maximum along the SF-streak is inversely proportional to the mean distance D_0 between the SFs I1 or I2. This is demonstrated in Fig. 9.2, where we present the intensity curves calculated in diffraction $10\bar{1}0$ for various D_0. Nevertheless, the FWHM of the diffraction curve cannot be used for the determination of D_0, since the shape of the diffraction maximum and its FWHM in particular are affected by function $\Psi(x)$. This is shown in Fig. 9.2, where the diffraction curves calculated for various widths of $\Psi(x)$ are plotted.

9.2 Comparison of experimental and theoretical data

Based on theory listed above we created a software allowing us to calculate the intensity distribution scattered on basal SFs in a-plane GaN. The text of our program for simulation can be found in Appendix C. We fitted the measured [0001]-scans to the theory described in the previous section. First, we determined

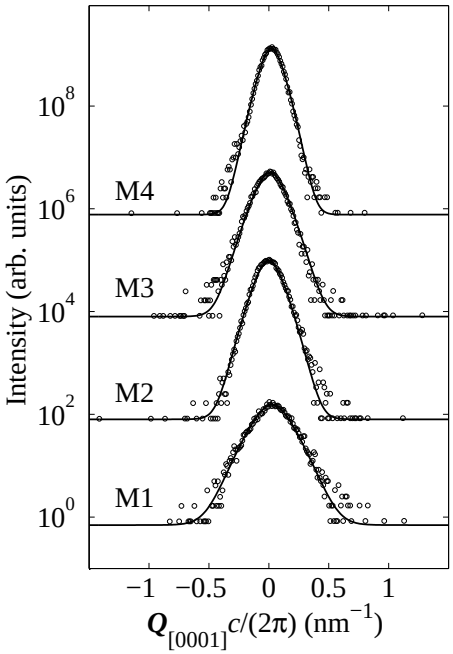

Figure 9.4: Experimental (circles) and theoretical (solid lines) intensity scans along the [0001] direction in $30\bar{3}0$ diffraction. The numbers of the samples are indicated, the curves are shifted vertically for clarity.

the FWHM W of function Ψ defined in Eq. 9.1.1 from the scans in diffraction $30\bar{3}0$, in which the SFs do not cause diffuse scattering (see Fig. 9.4).

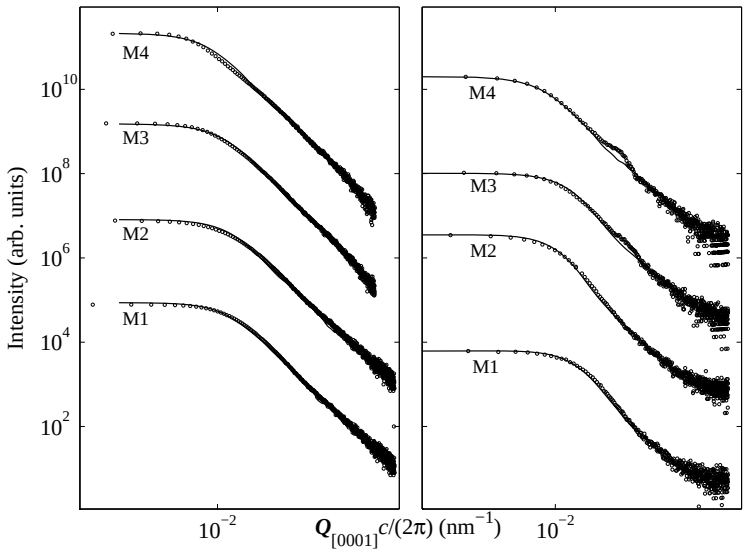

Figure 9.5: Experimental (circles) and theoretical (solid lines) intensity scans along the [0001] direction in $10\bar{1}0$ (left) and $20\bar{2}0$ (right) diffractions. The numbers of the samples are indicated, the curves are shifted vertically for clarity.

Then, using these values of W and taking into account the scaling property in Eq. 9.12 we fitted the intensity scans measured in diffractions $10\bar{1}0$ and $20\bar{2}0$. The experimental and fitted scans are plotted in Fig. 9.5. The measured and calculated intensity scans are in a very good agreement. From the fits we determined the dimensionless mean distances D_0 of the SFs and the SF density

$$\varrho = \frac{2}{cD_0}. \tag{9.14}$$

10. Discussion

10.1 Threading dislocation density in c-plane nitride-based materials

10.1.1 Monte Carlo simulation and EPD in c-plane GaN

The results of our Monte Carlo calculations are summarized in Table 10.1. Here, we compare the densities of screw and edge TDs obtained in different diffraction geometries with the total TDs density determined from the EPD method.

The results demonstrate that our method is able to give the densities of each type of threading dislocations separately. We found that total dislocation densities compare very well with the data obtained by standard etch pit density technique. The small but systematic difference between EPD and our results can be explained by the fact that we measured the superposition of the signals from two layers with different dislocation densities (below and above the SiN_x mask). Since the layer below the mask is comparatively thin (about 0.3 μm) its contribution does not exceed 10 % of the total diffraction. The higher dislocation density of this layer increases the density value determined from the fit.

From the Table 10.1 it follows that the resulting densities of edge threading dislocations determined from GID coincide within the error limits with the values obtained previously from coplanar x-ray diffraction, however, the accuracy of the GID data is approximately two times better. The application of our approach in GID requires the measurement of two RSMs in different grazing-incidence diffractions at synchrotron or diffractometer with rotating anode tube, where intensive high-collimated x-ray beam can be achieved and a couple of hours of computation but it gives a relatively high precision of the resulting density.

As was mentioned in Sec. 3.3.1 the SiN_x interlayer serves as a special barrier for mostly edge threading dislocations inhibiting them to extend over the whole thickness of the GaN layer. Our simulations confirm the total TDs density dependence on the depositing time of the SiN_x mask. The absence of this layer yields 3-10 times higher dislocation densities up to the order of $2 \times 10^9 cm^{-2}$ that makes such GaN films useless in industrial applications.

If we investigate a material possessing crystalline grains, the study of TDs can reveal the grain orientation within the epitaxial layers. The densities of

Sample	SiN_x deposition time, (s)	Total TDs density from EPD, (10^8cm^{-2})	ρ_{screw} from coplanar diffraction, (10^8cm^{-2})	ρ_{edge} from coplanar diffraction, (10^8cm^{-2})	ρ_{edge} from GID, (10^8cm^{-2})
S1	180	2.6	1.1±0.2	1.7±0.4	2.1±0.2
S2	150	4.8	1.3±0.2	4±0.7	4.1±0.4
S3	120	7.6	1.6±0.3	6.9±1	7±0.6
S4	0	20	2.1±0.3	20.6±2.5	20.6±1.9

Table 10.1: Densities of TDs with their errors determined from Monte Carlo simulation and EPD.

pure screw and edge dislocations are referred to a tilt and twist of the grains, respectively [165]. Thus, our method can be applied to estimate quantitatively the degree of grains disorientation.

10.1.2 Monte Carlo simulation in c-plane $Al_0.2Ga_0.8N$

The resulting densities of both types of TDs obtained by our simulations are summarized in Table 10.2.

As it is seen from the Fig. 7.10 and 7.10, RSMs in GID have the tendency to become broader with sample thickness decrease. It means that the increase of the film thickness is accompanied by the decrease of edge TDs density. For sample A5 with thicker layer of AlGaN we obtained the lowest density of edge threading dislocations ρ_{edge} and vice versa for sample A1 ρ_{edge} was the highest. It has been demonstrated by the weak-beam dark field (WBDF) and by the HRTEM methods that when the dislocation number is sufficiently high, the dislocation bending leads to the annihilation of the TDs by the formation of the dislocation loops. By increasing the overgrowth the edge TDs cannot interact after the bending and will continue to propagate parallel to the c-axis. Furthermore, the overgrowth will favour the coalescence of the two nearby islands leading to small areas with defect densities at the surface as it has been described in the growth model by O. Klein et al. [101].

The modelling of TDs reduction as function of the film thickness was developed by S.K. Mathis et al. [166] who have demonstrated that the dependence of the TDs for heteroepitaxial III-nitride layers does not follow the inverse proportional law of the film thickness $\sim \frac{1}{h}$ as it is known from the work of A. E. Romanov et al. in the case of fcc semiconductors [167]. The derived values of our ρ_{edge} were plotted in log-log scale as function of overgrowth thickness h (see Fig. 10.1). The fitting of the calculated densities of edge dislocations with a scaling law h^{-n} shows a good agreement with $n = 0.7$.

The average density of screw dislocations was determined from 0002 diffraction. It can be attributed to both main and bottom AlGaN layers. From Table 10.2 it is visible that the density of screw TDs is almost independent on the layer thickness. It is rather connected with the growing conditions and the presence of SiN_X interlayer. The densities of screw TDs obtained from 0008 diffraction correspond to from the main and bottom peaks. It is found that the density of screw TDs above the SiN_X mask is approximately twice lower that below

Sample	Thickness of AlGaN layer, (nm)	ρ_{edge} from GID, ($10^9 cm^{-2}$)	ρ_{screw} from 0002, ($10^9 cm^{-2}$)	ρ_{screw}^{main} from 0008, ($10^9 cm^{-2}$)	ρ_{screw}^{150nm} from 0008, ($10^9 cm^{-2}$)
A1	500	10.1±1	0.8±0.1	0.9±0.1	1.5±0.2
A2	1000	6.7±0.8	0.7±0.1	0.75±0.1	1.2±0.15
A3	1850	3.5±0.5	0.7±0.1	0.75±0.1	1.1±0.15
A4	2500	2.6±0.4	0.7±0.1	0.7±0.1	1.1±0.15
A5	3500	1.9±0.2	0.6±0.05	0.65±0.1	0.9±0.15

Table 10.2: Densities of TDs with their errors determined from Monte Carlo simulation.

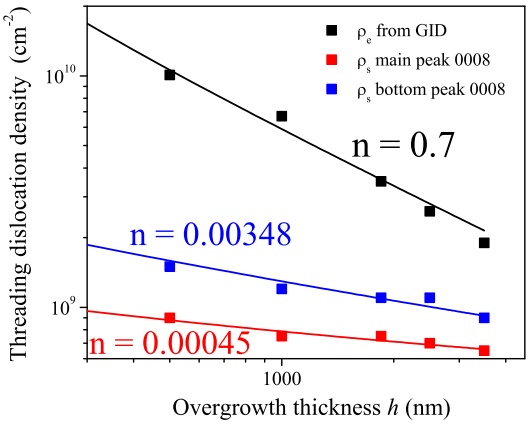

Figure 10.1: Variation of the TDs densities as a function function of the overgrowth thickness h.

the mask. That confirms the growers prediction that the SiN_X mask plays an important role in the reduction of screw TDs density. As it is shown in the Fig. 10.1, the fitting of the experimental data with a scaling law gives an exponent tending to zero. For the main and the bottom layers the parameter n is equal to 0.00045 and 0.0035 respectively.

10.1.3 Analysis of peaks broadening in c-plane $Al_0.2Ga_0.8N$

The series of 5 AlGaN samples was additionally studied by Lazarev et al. [153]. The aim of this study was to determine the screw and edge type threading dislocation densities and to derive the scaling law, which describes the dependency of TDs density on the layer thickness.

The density of TDs was determined by conventional analysis of the diffraction peaks broadening within the model of misoriented blocks [24, 131]. The average absolute values of the blocks tilt and twist are directly related with the full width half of maximum of the corresponding distributions of the crystallographic orientations. The tilt of the mosaic blocks causes the broadening of the symmetrical reflections in angular direction while the twist implies the broadening of the GID reflections.

The densities of screw and edge TDs was calculated using well known Eq. 5.7 and 5.8. The parameters α_Ω and α_Φ were determined from the slope of the Williamson–Hall (W-H) plot in symmetrical and GID geometry respectively [136]. For this reason a series of symmetrical (0002, 0004, 0006 and 0008) and

Sample	Thickness of AlGaN layer, (nm)	ρ_{edge}, (10^8cm^{-2})	ρ_{screw}^{main}, (10^8cm^{-2})	ρ_{screw}^{150nm}, (10^8cm^{-2})
A1	500	18.23	1.29	4.86
A2	1000	9.22	0.34	3.31
A3	1850	8.16	0.30	2.79
A4	2500	7.49	0.36	2.95
A5	3500	6.20	0.20	1.91

Table 10.3: Densities of TDs determined from peaks broadening analysis.

GID ($10\bar{1}0$, $20\bar{2}0$, $30\bar{3}0$) RSMs were measured using the setup described in Sec. 6.2. In symmetrical diffraction, the W-H plot was applied for the signals that come from the main and 150nm AlGaN layers. The TDs densities obtained with 30 % accuracy are listed in Table 10.3.

The densities of edge TDs found by Lazarev et al. are approximately 4-6 times lower than ones obtained with Monte Carlo method. The difference in screw TDs densities is about one order. The similar results for GaN films were obtained by Kaganer et al. comparing their advanced method with the conventional FWHM analysis [3]. This fact can be explained as follows. The TEM images showed that the films we study do not contain any misoriented grains. Therefore the application of FWHM analysis is not in general valid for our series of samples. The empiric coefficient 4.35 that stands in Eq. 5.7 and 5.8 is assumed to be constant. However, it is definitely not true because it should contain an information about the real individual dislocation ensembles. The diffuse part of x-ray scattering should be rather considered instead of broadening of rocking curves, which is one of the most important items of our Monte Carlo based approach.

Summarizing, we would like to mention that our method based on Monte Carlo simulation has proven to be a reliable method to simulate the RSM maps in coplanar and grazing-incidence geometries of two layers system. The experimental and simulated data were found to be in a good agreement, which allowed us to derive screw and edge treading dislocation densities with error less then 15% and compare the density of TDs for different thicknesses of the AlGaN layers. We found a dependence of edge TDs density in the top near-surface layer on the sample thickness, where the dislocation lines can be considered perpendicular to the sample surface. The thickness of the layer of AlGaN is affected mostly on the edge treading dislocations density, whereas the density of the screw treading dislocations is near constant and its deviation from the average value lies in the error region of our method.

10.2 Stacking faults density in a-plane GaN

The effective width of the SFs and density values obtained from the fits in $10\bar{1}0$ and $20\bar{2}0$ diffraction curves are presented in Tab. 10.4. The W values of the function Ψ defined in Eq. 9.1.1 are derived from the scans in diffraction $30\bar{3}0$. They are shown in Tab. 10.4 as well.

From the theory it follows that the FWHM of the [0001]-scans in diffractions $10\bar{1}0$ and $20\bar{2}0$ are equal and therefore the SF densities ϱ should not depend on the diffraction order H. However, the density values in Tab. 10.4 sometimes slightly differ. The reason of this difference is not completely clear yet. It could be caused by the difference in the information depths, from which the diffuse scattering is collected. The incidence and exit angles in $20\bar{2}0$ are larger than in $10\bar{1}0$, therefore the SF density determined from $20\bar{2}0$ is averaged over a layer thickness of about 14 μm, while $10\bar{1}0$ probes only an approx. 5 μm thick layer. The largest difference in the defect densities was observed in sample M2, where $\varrho_{20\bar{2}0} < \varrho_{10\bar{1}0}$. However, this sample contains a defect-reducing SiN layer buried in the GaN volume, so that the defect density in the surface layer is expected smaller than below the SiN layer. Therefore the effect of the information depth cannot explain this difference.

Sample	$\varrho_{10\bar{1}0}$ (10^5 cm^{-1})	$\varrho_{20\bar{2}0}$ (10^5 cm^{-1})	$\langle\varrho\rangle$ (10^5 cm^{-1})	S_{eff} (nm)	W (nm)
M1	4.1	4.1	4.1	140	8.6
M2	4.0	2.6	3.3	130	13.0
M3	3.2	3.8	3.5	180	11.7
M4	2.6	2.7	2.65	190	15.8

Table 10.4: Densities of the SFs determined from diffractions $10\bar{1}0$ and $20\bar{2}0$ for samples M1 to M4, the mean densities $\langle\varrho\rangle$ from both diffractions, the effective widths S_{eff} of the SFs and the widths W of the functions $\Psi(x)$ determined from diffraction $30\bar{3}0$. The density values are determined with an accuracy of approx. $\pm 10\%$, the errors of S_{eff} and W are approx. 10 nm and 0.1 nm, respectively.

Another possible explanation of the difference in the $\varrho_{10\bar{1}0,20\bar{2}0}$ values could be an inhomogeneous distribution of the defects in the layer volume (bunching of the defects), which has not been included in the theory. The irradiated sample surface in diffraction $10\bar{1}0$ is larger than in $20\bar{2}0$, so that the latter diffraction could be more sensitive to a possible bunching effect. Other structural imperfections like surface roughness or macroscopic sample bending cannot explain this difference.

Sample M4 exhibits the smallest SF density. This finding corresponds nicely to our expectations that any defects are reduced by overgrowing our samples with a thick high quality GaN layer. The FWHM W of the function $\Psi(x)$ include both the experimental resolution and diffuse x-ray scattering from other defects. The density of these defects can be hardly determined, qualitatively it increases with decreasing W.

In contrast to other works, our method determines the SF density from the whole intensity profiles of the SF streak. If the SF-streak is visible in the measured reciprocal-space intensity distribution, the influence of the stacking faults can be distinguished from other defects. Roughly speaking, the SF density is proportional to the FWHM of the SF streak, however, the whole intensity profile has to be taken into account. The minimum SF density (i.e. the maximum mean distance between adjacent fault planes) can be estimated from the minimum measurable broadening of the diffraction maximum in [0001] direction, which in our case is determined mainly by the angular resolution of the detector. For our geometry the minimum detectable SF density is about 10^4 cm^{-1}.

We have restricted our experiments to a small vicinity of the reciprocal lattice points $H0\bar{H}0$, this restriction did not allow us to distinguish between the types I1 and I2 of the SFs; the SF types I3 and E can be excluded. The resolution of the defect type from the [0001]-scans could be possible if we measure the scans around the anti-Bragg points $L = n + 1/2$. Nevertheless, the SF densities in Tab. 10.4 most likely apply to the I1 defects, since about 90% of all defects are of type I1 [22] because of their lower formation energy than the other defect types [31, 168].

We have developed a theoretical description of diffuse scattering from a random set of basal stacking faults in a-plane GaN epitaxial layers. We have simulated the distributions of the diffusely scattered x-ray intensity in direction perpendicular to the fault planes, i.e. along the [0001]-lines in reciprocal space crossing the reciprocal lattice points $H0\bar{H}0$ ($H = 1, 2, 3$). From the comparison

of the simulations with experimental data on a series of GaN samples we determined the density of basal stacking faults. The method makes it possible to distinguish between the diffuse scattering from stacking faults and the effects of other structural defects.

Conclusions

The results presented in the thesis cover a wide spectrum of knowledge concerning growth, defect structure and methods of its investigation of nitride-based semiconductors. They can be divided into several major items and summarized as follows.

- We developed a new Monte Carlo method allowing us to simulate a diffuse scattering from randomly distributed threading dislocations with dislocation lines perpendicular to the sample surface. As an object of our investigation we chose c-plane GaN heteroepitaxial layers with different dislocation densities. Our simulation technique was firstly applied to coplanar symmetrical and asymmetrical diffraction. The comparison of theoretical and experimental RSMs shapes as well as analysis of the diffraction curves slopes enabled to obtain separately densities of screw and edge threading dislocations in each sample with accuracy of $\pm$ 15 %.

- In order to improve the precision of TDs density determination we modified our software that resulted in the development of technique appropriate for RSMs simulation in GID geometry. The experimental GID data obtained by the use of synchrotron radiation were compared with GID simulations. This study gave us the density of pure edge TDs that can be taken as fixed parameter in the screw TDs density determination from symmetrical coplanar diffraction. The use of GID geometry increased the accuracy of our method by 5 %. As to our knowledge the simulation of diffuse scattering from defects in GID geometry has not been performed before us.

- Our developed Monte Carlo technique for GaN material was used for AlGaN c-plane films consisted of two layers with different thicknesses and Al concentration. Since the dislocation lines of edge TDs in AlGaN are not exactly perpendicular to the sample surface, the application of our GID-based method was limited to the determination of edge TDs density in the near-surface region. The use of synchrotron radiation allowed us to go to higher symmetrical reflections such as 0008 in order to resolve the peaks stemming from two AlGaN layers. These two peaks were independently simulated and summed up in the single RSM that enabled us to obtain the densities of screw TDs in each of these layers. This part of our work showed that our method could characterize more complicated objects than GaN films and give herewith high precision.

- The basal stacking planes in a-plane GaN and method of their density determination layers are of a high interest. Prof. RNDr Václav Holý developed the theory describing the diffuse scattering from BSFs within Monte Carlo approach. The software based on this theory was used to calculate the intensity distribution along the SF-streak, which was compared with the experimental data measured for a series of a-plane GaN. We achieved an accurate quantitative estimation of I_1 and I_2 SFs density in a-plane GaN. These results can be treated as unique since the determination of SFs

density in a-plane GaN layers by means of x-ray technique was reported the first time.

The software presented in this PhD thesis can be used for diagnostics of the most important defects in III-nitride group of materials. The combination of non-destructive technique with our Monte Carlo simulation gives a powerful tool to examine the quality of relatively thin heteroepitaxial nitride-based layers. Our method can be used during the epitaxial growth of GaN material providing its in-situ characterization.

However, every model has its limitation. In our case it is worth to mention that very thin films (less than 50 nm) cannot be investigated by our method. Due to influence of misfit dislocations located at the substrate/film interface, the diffuse scattering from threading dislocation ceases to be dominant. The MDs are not considered within our model and their impact to the total intensity distribution cannot be distinguished. Another important remark is that the dislocation lines of dislocations under study have to be perpendicular or near-perpendicular to the sample surface, therefore the defects in for example cubic GaN cannot be described by our approach. In order to use the GID geometry for reciprocal space mapping, the surface roughness is required to be minimal.

The topics discussed in the present work can serve as a theoretical background for further developing:

- The knowledge and the experience gained during the work on the thesis can be extended to other various sample systems of nitride-based semiconductors.

- The introduction of correlation in the position of randomly generated dislocations can possibly increase the accuracy of our approach as well as the software optimization can significantly reduce the time of computation.

- The determination of the SFs density in m-plane and semipolar GaN films is of high importance. Making minimal changes in our software and choosing the appropriate diffraction geometry it is possible to perform a computation of SFs density in these materials.

Bibliography

[1] Hadis Morkoc. *Handbook of Nitride Semiconductors and Devices: Materials Properties, Physics and Growth*, volume 1. Wiley-VCH Verlag GmbH & Co. KGaA, 2008, ►.

[2] M.A. Krivoglaz, O.H. Glebov, V.G. Bar'yakhtar, M.A. Ivanov, S.C. Moss, and J.C. Peisl. *X-Ray and Neutron Diffraction in Nonideal Crystals*. Springer, 1996, ►.

[3] V. M. Kaganer, O. Brandt, A. Trampert, and K. H. Ploog. X-ray diffraction peak profiles from threading dislocations in GaN epitaxial films. *Phys. Rev. B*, 72:045423, Jul 2005. doi: 10.1103/PhysRevB.72.045423, ►.

[4] Roy Szweda. *Gallium Nitride and Related Wide Bandgap Materials and Devices. A Market and Technology Overview 1998-2003*. ELSEVIER LTD, 2000, ►.

[5] Zhe Chuan Feng. *III-nitride Semiconductor Materials*. World Scientific Publishing Company, 2006, ►.

[6] Xu Lin Nguyen, Thi Ngoc Nhien Nguyen, Vinh Thang Chau, and Mau Chien Dang. The fabrication of GaN-based light emitting diodes (LEDs). *Advances in Natural Sciences: Nanoscience and Nanotechnology*, 1(2):025015, 2010, ►.

[7] Omkar Jani, Ian Ferguson, Christiana Honsberg, and Sarah Kurtz. Design and characterization of GaN/InGaN solar cells. *Applied Physics Letters*, 91 (13):132117, 2007. doi: 10.1063/1.2793180, ►.

[8] John Price Hirth. *Theory of dislocations*. Wiley, 2 edition, 1982.

[9] John Price Hirth and Jens Lothe. *Theory of dislocations*. Krieger Pub Co, 1992, ►.

[10] D. J. Bacon Derek Hull. *Introduction to Dislocations*. Elsevier, 5 edition, 2011, ►.

[11] Ramiro Pareja Pareja. Experimental Techniques in Materials Science (Mechanical Properties) , 2010-2011. Lecture course.

[12] Helmut Foell. Defects in Crystals, ►. Lecture course.

[13] M. Murayama, J. M. Howe, H. Hidaka, and S. Takaki. Atomic-Level Observation of Disclination Dipoles in Mechanically Milled, Nanocrystalline Fe. *Science*, 295(5564):2433–2435, 2002. doi: 10.1126/science.1067430, ►.

[14] M. Hatherly F. J. Humphreys. *Recrystallization and Related Annealing Phenomena*. Elsevier, 2 edition, 2003, ►.

[15] J.W. Christian and S. Mahajan. Deformation twinning. *Progress in Materials Science*, 39(1-2):1 – 157, 1995. ISSN 0079-6425. doi: 10.1016/0079-6425(94)00007-7, ►.

[16] *Vacancies and interstitials in metals and alloys*, volume 14-19, September 1986. Trans Tech Publications, ►.

[17] A. J. Morton. Point defects and defect interactions in metals, edited by J.-I. Takamura, M. Doyama and M. Kiritani. *Acta Crystallographica Section A*, 40(3):310, May 1984. doi: 10.1107/S0108767384000647, ►.

[18] T. Mattila and R. M. Nieminen. Direct Antisite Formation in Electron Irradiation of GaAs. *Phys. Rev. Lett.*, 74:2721–2724, Apr 1995. doi: 10.1103/PhysRevLett.74.2721, ►.

[19] Alan D. Adler, Frederick R. Longo, Frank Kampas, and Jean Kim. On the preparation of metalloporphyrins. *Journal of Inorganic and Nuclear Chemistry*, 32(7):2443 – 2445, 1970. ISSN 0022-1902. doi: 10.1016/0022-1902(70)80535-8, ►.

[20] Kapolnek D. Tarsa E.J. Heying B. Keller S. Keller B.P. Mishra U.K. Denbaars S.P. Speck J.S. Wu, X.H. Nucleation layer evolution in metal-organic chemical vapor deposition grown GaN. *Applied Physics Letters*, 68 (10):1371–1373, 1996, ►. cited By (since 1996) 144.

[21] J.S. Speck and S.J. Rosner. The role of threading dislocations in the physical properties of GaN and its alloys. *Physica B: Condensed Matter*, 273-274 (0):24 – 32, 1999. ISSN 0921-4526. doi: 10.1016/S0921-4526(99)00399-3, ►.

[22] M A Moram and M E Vickers. X-ray diffraction of III-nitrides. *Reports on Progress in Physics*, 72(3):036502, 2009, ►.

[23] M E Vickers, M J Kappers, R Datta, C McAleese, T M Smeeton, F D G Rayment, and C J Humphreys. In-plane imperfections in GaN studied by x-ray diffraction. *Journal of Physics D: Applied Physics*, 38(10A):A99, 2005, ►.

[24] T. Metzger, R. Hoepler, E. Born, O. Ambacher, M. Stutzmann, R. Stoemmer, M. Schuster, H. Goebel, S. Christiansen, M. Albrecht, and H. P. Strunk. Defect structure of epitaxial GaN films determined by transmission electron microscopy and triple-axis X-ray diffractometry. *Philosophical Magazine A*, 77(4):1013–1025, 1998. doi: 10.1080/01418619808221225, ►.

[25] S. J. Shaibani and P. M. Hazzledine. The displacement and stress fields of a general dislocation close to a free surface of an isotropic solid. *Philosophical Magazine A*, 44(3):657–665, 1981. doi: 10.1080/01418618108236168, ►.

[26] V. M. Kaganer, R. Köhler, M. Schmidbauer, R. Opitz, and B. Jenichen. X-ray diffraction peaks due to misfit dislocations in heteroepitaxial structures. *Phys. Rev. B*, 55:1793–1810, Jan 1997. doi: 10.1103/PhysRevB.55.1793, ►.

[27] J. Bai, T. Wang, K.B. Lee, P.J. Parbrook, Q. Wang, and A.G. Cullis. Generation of misfit dislocations in highly mismatched GaN/AlN layers. *Surface Science*, 602(15):2643 – 2646, 2008. ISSN 0039-6028. doi: 10.1016/j.susc.2008.06.027, ►.

[28] J. Lothe Vladimir L. Indenbom. *Elastic Strain Fields and Dislocation Mobility (Modern Problems in Condensed Matter Sciences)*. North-Holland, 1992, ►.

[29] Vladimir M. Kaganer, Oliver Brandt, Henning Riechert, and Karl K. Sabelfeld. X-ray diffraction of epitaxial films with arbitrarily correlated dislocations: Monte Carlo calculation and experiment. *Phys. Rev. B*, 80: 033306, Jul 2009. doi: 10.1103/PhysRevB.80.033306, ►.

[30] Fabio Bernardini, Vincenzo Fiorentini, and David Vanderbilt. Spontaneous polarization and piezoelectric constants of III-V nitrides. *Phys. Rev. B*, 56: R10024–R10027, Oct 1997. doi: 10.1103/PhysRevB.56.R10024, ►.

[31] Dmitri N. Zakharov, Zuzanna Liliental-Weber, Brian Wagner, Zachary J. Reitmeier, Edward A. Preble, and Robert F. Davis. Structural TEM study of nonpolar a-plane gallium nitride grown on 4H-SiC by organometallic vapor phase epitaxy. *Phys. Rev. B*, 71:235334, Jun 2005. doi: 10.1103/PhysRevB.71.235334, ►.

[32] M. Barchuk, V. Holý, D. Kriegner, J. Stangl, S. Schwaiger, and F. Scholz. Diffuse x-ray scattering from stacking faults in *a*-plane GaN epitaxial layers. *Phys. Rev. B*, 84:094113, Sep 2011. doi: 10.1103/PhysRevB.84.094113, ►.

[33] C. Stampfl and Chris G. Van de Walle. Energetics and electronic structure of stacking faults in AlN, GaN, and InN. *Phys. Rev. B*, 57:R15052–R15055, Jun 1998. doi: 10.1103/PhysRevB.57.R15052, ►.

[34] Tanya Paskova. *Nitrides with Nonpolar Surfaces*. Wiley-VCH, 2008, ►.

[35] Pierre Gibart. Metal organic vapour phase epitaxy of GaN and lateral overgrowth. *Reports on Progress in Physics*, 67(5):667, 2004, ►.

[36] J W Orton and C T Foxon. Group III nitride semiconductors for short wavelength light-emitting devices. *Reports on Progress in Physics*, 61(1):1, 1998, ►.

[37] H. Okumura, K. Ohta, G. Feuillet, K. Balakrishnan, S. Chichibu, H. Hamaguchi, P. Hacke, and S. Yoshida. Growth and characterization of cubic GaN. *Journal of Crystal Growth*, 178(1-2):113 – 133, 1997. ISSN 0022-0248. doi: 10.1016/S0022-0248(97)00084-5, ►.

[38] Ryuhei Kimura, Yutaka Gotoh, Takeo Matsuzawa, and Kiyoshi Takahashi. High-purity cubic gan grown on a algaas buffer layer by molecular beam epitaxy. *Journal of Crystal Growth*, 209(2-3):382 – 386, 2000. ISSN 0022-0248. doi: 10.1016/S0022-0248(99)00575-8, ►.

[39] A Philippe, C Bru-Chevallier, M Vernay, G Guillot, J HĂĽbner, B Daudin, and G Feuillet. Optical properties of cubic GaN grown on SiC/Si substrates. *Materials Science and Engineering: B*, 59(1-3):168 – 172, 1999. ISSN 0921-5107. doi: 10.1016/S0921-5107(98)00413-9, ►.

[40] Oliver Brandt, Hui Yang, Jochen R. Müllhäuser, Achim Trampert, and Klaus H. Ploog. Properties of cubic GaN grown by MBE. *Materials Science and Engineering: B*, 43(1-3):215–221, 1997. ISSN 0921-5107. doi: 10.1016/S0921-5107(96)01871-5, ►. E-MRS 1996 Spring Meeting, Symposium C: UV, Blue and Green Light Emission from Semi-conductor Materials.

[41] Mario Gonsalves, Wook Kim, Vijay Narayanan, and S. Mahajan. Influence of aln nucleation layer growth conditions on quality of gan layers deposited on (0001) sapphire. *Journal of Crystal Growth*, 240(3-4):347 – 354, 2002. ISSN 0022-0248. doi: 10.1016/S0022-0248(02)00906-5, ►.

[42] Stephan Schwaiger, Sebastian Metzner, Thomas Wunderer, Ilona Argut, Johannes Thalmair, Frank Lipski, Matthias Wieneke, Jürgen Bläsing, Frank Bertram, Josef Zweck, Alois Krost, Jürgen Christen, and Ferdinand Scholz. Growth and coalescence behavior of semipolar (11-22) GaN on pre-structured r-plane sapphire substrates. *physica status solidi (b)*, 248(3):588–593, 2011. ISSN 1521-3951. doi: 10.1002/pssb.201046336, ►.

[43] J. S. Speck and S. F. Chichibu. Nonpolar and Semipolar Group III Nitride-Based Materials. *MRS Bulletin*, 34:304–312, 2009. doi: 10.1557/mrs2009.91, ►.

[44] F Scholz. Semipolar GaN grown on foreign substrates: a review. *Semiconductor Science and Technology*, 27(2):024002, 2012, ►.

[45] M. D. Craven, F. Wu, A. Chakraborty, B. Imer, U. K. Mishra, S. P. DenBaars, and J. S. Speck. Microstructural evolution of a-plane GaN grown on a-plane SiC by metalorganic chemical vapor deposition. *Applied Physics Letters*, 84(8):1281–1283, 2004. doi: 10.1063/1.1650545, ►.

[46] Jun Zou and Weidong Xiang. Nonpolar m- and a-plane GaN thin films grown on gamma-LiAlO2 substrates. *Journal of Crystal Growth*, 311(12):3285 – 3288, 2009. ISSN 0022-0248. doi: 10.1016/j.jcrysgro.2009.03.015, ►.

[47] X. Ni, Ü. Özgür, H. Morkoç, Z. Liliental-Weber, and H. O. Everitt. Epitaxial lateral overgrowth of a-plane GaN by metalorganic chemical vapor deposition. *Journal of Applied Physics*, 102(5):053506, 2007. doi: 10.1063/1.2773692, ►.

[48] Y. S. Cho, Q. Sun, I.-H. Lee, T.-S. Ko, C. D. Yerino, J. Han, B. H. Kong, H. K. Cho, and S. Wang. Reduction of stacking fault density in m-plane GaN grown on SiC. *Applied Physics Letters*, 93(11):111904, 2008. doi: 10.1063/1.2985816, ►.

[49] Kwang-Choong Kim, Mathew C. Schmidt, Feng Wu, Melvin B. McLaurin, Asako Hirai, Shuji Nakamura, Steven P. DenBaars, and James S. Speck. Low extended defect density nonpolar m-plane GaN by sidewall lateral epitaxial overgrowth. *Applied Physics Letters*, 93(14):142108, 2008. doi: 10.1063/1.2908978, ►.

[50] R. Armitage and H. Hirayama. M-plane GaN grown on m-sapphire by metalorganic vapor phase epitaxy. *Applied Physics Letters*, 92(9):092121, 2008. doi: 10.1063/1.2894509, ►.

[51] Ulrich T. Schwarz and Michael Kneissl. Nitride emitters go nonpolar. *physica status solidi (RRL) - Rapid Research Letters*, 1(3):A44–A46, 2007. ISSN 1862-6270. doi: 10.1002/pssr.200750018, ►.

[52] Roghaiyeh Ravash, Juergen Blaesing, Armin Dadgar, and Alois Krost. Semipolar single component GaN on planar high index Si(11h) substrates. *Applied Physics Letters*, 97(14):142102, 2010. doi: 10.1063/1.3492835, ►.

[53] Stephan Schwaiger, Ilona Argut, Thomas Wunderer, Rudolf Rösch, Frank Lipski, Johannes Biskupek, Ute Kaiser, and Ferdinand Scholz. Planar semipolar (10-11) GaN on (11-23) sapphire. *Applied Physics Letters*, 96 (23):231905, 2010. doi: 10.1063/1.3442484, ►.

[54] Klavs F. Jensen, Dimitrios I. Fotiadis, and Triantafillos J. Mountziaris. Detailed models of the movpe process. *Journal of Crystal Growth*, 107 (1-4):1 – 11, 1991. ISSN 0022-0248. doi: 10.1016/0022-0248(91)90428-8, ►.

[55] Dimitrios I. Fotiadis, Shigekazu Kieda, and Klavs F. Jensen. Transport phenomena in vertical reactors for metalorganic vapor phase epitaxy: I. effects of heat transfer characteristics, reactor geometry, and operating conditions. *Journal of Crystal Growth*, 102(3):441 – 470, 1990. ISSN 0022-0248. doi: 10.1016/0022-0248(90)90403-8, ►.

[56] R.P Pawlowski, C Theodoropoulos, A.G Salinger, T.J Mountziaris, H.K Moffat, J.N Shadid, and E.J Thrush. Fundamental models of the metalorganic vapor-phase epitaxy of gallium nitride and their use in reactor design. *Journal of Crystal Growth*, 221(1-4):622 – 628, 2000. ISSN 0022-0248. doi: 10.1016/S0022-0248(00)00789-2, ►.

[57] J. Hertkorn, P. Brueckner, S.B. Thapa, T. Wunderer, F. Scholz, M. Feneberg, K. Thonke, R. Sauer, M. Beer, and J. Zweck. Optimization of nucleation and buffer layer growth for improved GaN quality. *Journal of Crystal Growth*, 308(1):30 – 36, 2007. ISSN 0022-0248. doi: 10.1016/j.jcrysgro.2007.07.056, ►.

[58] O Ambacher. Growth and applications of Group III-nitrides. *Journal of Physics D: Applied Physics*, 31(20):2653, 1998, ►.

[59] Baranowski J. M. Pakula, K. and J. Borysiuk. Two- and three-dimensional growth modes of nitride layers. *Cryst. Res. Technol.*, 42(12):1176–1184, 2007. doi: 10.1002/crat.200711003, ►.

[60] H.Z Xu, K Takahashi, C.X Wang, Z.G Wang, Y Okada, M Kawabe, I Harrison, and C.T Foxon. Effect of in situ thermal treatment during growth on crystal quality of GaN epilayer grown on sapphire substrate by MOVPE. *Journal of Crystal Growth*, 222(1-2):110 – 117, 2001. ISSN 0022-0248. doi: 10.1016/S0022-0248(00)00935-0, ►.

[61] Kazumasa Hiramatsu. Epitaxial lateral overgrowth techniques used in group III nitride epitaxy. *Journal of Physics: Condensed Matter*, 13(32): 6961, 2001, ►.

[62] J. Hertkorn, F. Lipski, P. Brueckner, T. Wunderer, S.B. Thapa, F. Scholz, A. Chuvilin, U. Kaiser, M. Beer, and J. Zweck. Process optimization for the effective reduction of threading dislocations in MOVPE grown GaN using in situ deposited masks. *Journal of Crystal Growth*, 310(23):4867 – 4870, 2008. ISSN 0022-0248. doi: 10.1016/j.jcrysgro.2008.07.075, ►.

[63] S. Gradečak, P. Stadelmann, V. Wagner, and M. Ilegems. Bending of dislocations in GaN during epitaxial lateral overgrowth. *Applied Physics Letters*, 85(20):4648–4650, 2004. doi: 10.1063/1.1823593, ►.

[64] B. Beaumont, M. Vaille, T. Boufaden, B. el Jani, and P. Gibart. High quality GaN grown by MOVPE. *Journal of Crystal Growth*, 170(1-4):316 – 320, 1997. ISSN 0022-0248. doi: 10.1016/S0022-0248(96)00635-5, ►.

[65] R.J. Molnar, W. GĂ¶tz, L.T. Romano, and N.M. Johnson. Growth of gallium nitride by hydride vapor-phase epitaxy. *Journal of Crystal Growth*, 178(1-2):147 – 156, 1997. ISSN 0022-0248. doi: 10.1016/S0022-0248(97)00075-4, ►.

[66] C. Hemmingsson, P.P. Paskov, G. Pozina, M. Heuken, B. Schineller, and B. Monemar. Hydride vapour phase epitaxy growth and characterization of thick GaN using a vertical HVPE reactor. *Journal of Crystal Growth*, 300(1):32 – 36, 2007. ISSN 0022-0248. doi: 10.1016/j.jcrysgro.2006.10.223, ►.

[67] C Klemenz and H.J Scheel. Crystal growth and liquid-phase epitaxy of gallium nitride. *Journal of Crystal Growth*, 211(1-4):62 – 67, 2000. ISSN 0022-0248. doi: 10.1016/S0022-0248(99)00831-3, ►.

[68] W. Seifert, G. Fitzl, and E. Butter. Study on the growth rate in VPE of GaN. *Journal of Crystal Growth*, 52, Part 1(0):257 – 262, 1981. ISSN 0022-0248. doi: 10.1016/0022-0248(81)90201-3, ►.

[69] H. Morkoc. Comprehensive characterization of hydride VPE grown GaN layers and templates. *Materials Science and Engineering: R: Reports*, 33(5-6):135 – 207, 2001. ISSN 0927-796X. doi: 10.1016/S0927-796X(01)00031-6, ►.

[70] Xueping Xu, R.P Vaudo, C Loria, A Salant, G.R Brandes, and J Chaudhuri. Growth and characterization of low defect GaN by hydride vapor phase epitaxy. *Journal of Crystal Growth*, 246(3-4):223 – 229, 2002. ISSN 0022-0248. doi: 10.1016/S0022-0248(02)01745-1, ►.

[71] G. Lukin, C. Röder, E. Niederschlag, Y. Shashev, U. Mühle, O. Pätzold, J. Kortus, D. Rafaja, and M. Stelter. Nucleation of GaN on sapphire substrates at intermediate temperatures by Hydride Vapor Phase Epitaxy. *Crystal Research and Technology*, 47(2):121–130, 2012. ISSN 1521-4079. doi: 10.1002/crat.201100461, ►.

[72] E. Kuphal. Liquid phase epitaxy. *Applied Physics A: Materials Science & Processing*, 52:380–409, 1991. ISSN 0947-8396, ►. 10.1007/BF00323650.

[73] M. Azizi, E. Meissner, J. Friedrich, and G. Müller. Liquid phase epitaxy (LPE) of GaN on c- and r-faces of AlN substrates. *Journal of Crystal Growth*, 322(1):74 – 77, 2011. ISSN 0022-0248. doi: 10.1016/j.jcrysgro.2011.03.014, ►.

[74] G. Sun, E. Meissner, P. Berwian, G. Müller, and J. Friedrich. Study on the kinetics of the formation reaction of GaN from Ga-solutions under ammonia atmosphere. *Journal of Crystal Growth*, 305(2):326 – 334, 2007. ISSN 0022-0248. doi: 10.1016/j.jcrysgro.2007.04.007, ►.

[75] M. Bockowski, P. Strak, P. Kempisty, I. Grzegory, B. Lucznik, S. Krukowski, and S. Porowski. Liquid phase epitaxy of GaN on MOCVD GaN/sapphire and HVPE free-standing substrates under high nitrogen pressure. *physica status solidi (c)*, 5(6):1539–1542, 2008. ISSN 1610-1642. doi: 10.1002/pssc.200778462, ►.

[76] Yasuhiro Isobe, Daisuke Iida, Tatsuyuki Sakakibara, Motoaki Iwaya, Tetsuya Takeuchi, Satoshi Kamiyama, Isamu Akasaki, Hiroshi Amano, Mamoru Imade, Yasuo Kitaoka, and Yusuke Mori. Optimization of initial movpe growth of non-polar m- and a-plane gan on na flux grown lpe-gan substrates. *physica status solidi (c)*, 8(7-8):2095–2097, 2011. ISSN 1610-1642. doi: 10.1002/pssc.201001144, ►.

[77] S. Hussy, E. Meissner, P. Berwian, J. Friedrich, and G. MĂĽller. Low-pressure solution growth (LPSG) of GaN templates with diameters up to 3 inch. *Journal of Crystal Growth*, 310(4):738 – 747, 2008. ISSN 0022-0248. doi: 10.1016/j.jcrysgro.2007.11.115, ►.

[78] R. F. C. Farrow. *Molecular beam epitaxy: applications to key materials*. William Andrew, 1995, ►.

[79] Fernando Rinaldi. Basics of molecular beam epitaxy (MBE). Technical report, Optoelectronics Department, University of Ulm, 2002.

[80] John Wauchope Matthews. *Epitaxial Growth, Part A*. Academic Pr, 1975, ►.

[81] B.A. Joyce, J. Zhang, T. Shitara, J.H. Neave, A. Taylor, S. Armstrong, M.E. Pemble, and C.T. Foxon. Dynamics and kinetics of mbe growth. *Journal of Crystal Growth*, 115(1-4):338 – 347, 1991. ISSN 0022-0248. doi: 10.1016/0022-0248(91)90765-W, ►.

[82] Bill Boggess. Mass Spectrometry Desk Reference (Sparkman, O. David). *Journal of Chemical Education*, 78(2):168, 2001. doi: 10.1021/ed078p168.2, ►.

[83] P.I. Cohen A. Ichimiya. *Reflection High Energy Electron Diffraction*. Cambridge University Press, Cambridge, 2004, ►.

[84] David C. Joy Charles E. Lyman Patrick Echlin Eric Lifshin Linda Sawyer J.R. Michael Joseph Goldstein, Dale E. Newbury. *Scanning Electron Microscopy and X-ray Microanalysis*. Springer US, 2007, ►.

[85] M. P. Seahl David Briggs. *Practical Surface Analysis, Auger and X-ray Photoelectron Spectroscopy*, volume 1. John Wiley and Sons Ltd, 1996, ►.

[86] S Fernandez, F B Naranjo, F Calle, M A Sanchez-Garcia, E Calleja, P Vennegues, A Trampert, and K H Ploog. MBE-grown high-quality (Al,Ga)N/GaN distributed Bragg reflectors for resonant cavity LEDs. *Semiconductor Science and Technology*, 16(11):913, 2001, ►.

[87] Ashutosh Sagar, C. D. Lee, R. M. Feenstra, C. K. Inoki, and T. S. Kuan. Plasma-assisted molecular beam epitaxy of GaN on porous SiC substrates with varying porosity. volume 21, pages 1812–1817. AVS, 2003. doi: 10.1116/1.1589513, ►.

[88] C. K. Inoki T. S. Kuan Ashutosh Sagar, R. M. Feenstra and D. D. Koleske. Combined MOCVD and MBE growth of GaN on porous SiC. *MRS Proceedings*, 798, 2003. doi: 10.1557/PROC-798-Y9.6.

[89] Michael Lindeborg. Surface morphology and electrical properties of GaN layers and AlGaN/GaN high electron mobility transistor (HEMT) structures grown by molecular beam epitaxy. *The Harvard Undergraduate Research Journal, Material science*, 3(2), 2011, ►.

[90] M.A di Forte-Poisson, F Huet, A Romann, M Tordjman, D Lancefield, E Pereira, J Di Persio, and B Pecz. Relationship between physical properties and gas purification in gan grown by metalorganic vapor phase epitaxy. *Journal of Crystal Growth*, 195(1 - 4):314 – 318, 1998. ISSN 0022-0248. doi: 10.1016/S0022-0248(98)00584-3, ►.

[91] Peter Brueckner, Frank Habel, and Ferdinand Scholz. HVPE growth of high quality GaN layers. *physica status solidi (c)*, 3(6):1471–1474, 2006. ISSN 1610-1642. doi: 10.1002/pssc.200565160, ►.

[92] Itaya-K. Nishio J. Fujimoto H. Kokubun Y. Sugiura, L. Effects of thermal treatment of low-temperature GaN buffer layers on the quality of subsequent GaN layers. *Journal of Applied Physics*, 82(10):4877–4882, 1997, ►.

[93] Joachim Hertkorn. *Verbesserung der lateralen Stromfuehrung in hocheffizienten Halbleiterlichtquellen*. PhD thesis, Institut fuer Optoelektronik, Universitaet Ulm, 2009, ►.

[94] Z. Bougrioua, M. Azize, A. Jimenez, A.-F. Brana, P. Lorenzini, B. Beaumont, E. Munoz, and P. Gibart. Fe doping for making resistive GaN layers with low dislocation density; consequence on HEMTs. *physica status solidi (c)*, 2(7):2424–2428, 2005. ISSN 1610-1642. doi: 10.1002/pssc.200461588, ►.

[95] Stephan Schwaiger, Frank Lipski, Thomas Wunderer, and Ferdinand Scholz. Influence of slight misorientations of r -plane sapphire substrates on the growth of nonpolar a -plane GaN layers via HVPE. *physica status solidi (c)*, 7(7-8):2069–2072, 2010. ISSN 1610-1642. doi: 10.1002/pssc.200983514, ►.

[96] T. Paskova, V. Darakchieva, P.P. Paskov, J. Birch, E. Valcheva, P.O.A. Persson, B. Arnaudov, S. Tungasmitta, and B. Monemar. Properties of nonpolar a-plane GaN films grown by HVPE with AlN buffers. *Journal of Crystal Growth*, 281(1):55 – 61, 2005. ISSN 0022-0248. doi: 10.1016/j.jcrysgro.2005.03.013, ►.

[97] J.F. Yan, L.W. Guo, J. Zhang, X.L. Zhu, G.J. Ding, Z.G. Xing, Z.T. Zhou, X.J. Pei, Y. Wang, H.Q. Jia, H. Chen, and J.M. Zhou. Characteristics of the improved a-plane GaN films grown on r-plane sapphire with two-step AlN buffer layer. *Journal of Crystal Growth*, 307(1):35 – 39, 2007. ISSN 0022-0248. doi: 10.1016/j.jcrysgro.2007.06.019, ►.

[98] K. Forghani, M. Klein, F. Lipski, S. Schwaiger, J. Hertkorn, R.A.R. Leute, F. Scholz, M. Feneberg, B. Neuschl, K. Thonke, O. Klein, U. Kaiser, R. Gutt, and T. Passow. High quality AlGaN epilayers grown on sapphire using SiNx interlayers. *Journal of Crystal Growth*, 315(1):216 – 219, 2011. ISSN 0022-0248. doi: 10.1016/j.jcrysgro.2010.08.044, ►.

[99] B. Neuschl, K. J. Fujan, M. Feneberg, I. Tischer, K. Thonke, K. Forghani, M. Klein, and F. Scholz. Cathodoluminescence and photoluminescence study on AlGaN layers grown with SiNx interlayers. *Applied Physics Letters*, 97(19):192108, 2010. doi: 10.1063/1.3515865, ►.

[100] K. Engl, M. Beer, N. Gmeinwieser, U.T. Schwarz, J. Zweck, W. Wegscheider, S. Miller, A. Miler, H.-J. Lugauer, G. Bruederl, A. Lell, and V. Haerle. Influence of an in situ-deposited intermediate layer inside GaN and AlGaN layers on SiC substrates. *Journal of Crystal Growth*, 289 (1):6 – 13, 2006. ISSN 0022-0248. doi: 10.1016/j.jcrysgro.2005.10.115, ►.

[101] O. Klein, J. Biskupek, K. Forghani, F. Scholz, and U. Kaiser. TEM investigations on growth interrupted samples for the correlation of the dislocation propagation and growth mode variations in AlGaN deposited on SiNx interlayers. *Journal of Crystal Growth*, 324(1):63 – 72, 2011. ISSN 0022-0248. doi: 10.1016/j.jcrysgro.2011.03.050, ►.

[102] Tsukihara-M. Kataoka K. Kato A. Nishino K. Sakai S. Okimoto, T. GaN- and AlGaN-based UV-LEDs on sapphire by metal-organic chemical vapor deposition. *Physica Status Solidi (C) Current Topics in Solid State Physics*, 5(9):3066–3068, 2008, ►.

[103] U. Pietsch, V. Holý, and T. Baumbach. *High Resolution X-ray Scattering from Thin Films to Lateral Nanostructures*. Springer, 2004, ►.

[104] J. Als-Nielsen and D. McMorrow. *Elements of modern x-ray physics*. New York: J. Wiley and Sons, 2008, ►.

[105] Martin Schmidbauer. *X-Ray Diffuse Scattering from Self-Organized Mesoscopic Semiconductor Structures*. Springer, 2004, ►.

[106] Helmut Kohl Ludwig Reimer. *Transmission Electron Microscopy: Physics of Image Formation*. Springer US, 5 edition, 2008, ►.

[107] C. Barry Carterl David B. Williams. *Transmission Electron Microscopy. A Textbook for Materials Science*. Springer US, 6 edition, 2005, ►.

[108] James Howe Brent Fultz. *Transmission Electron Microscopy and Diffractometry of Materials*. Springer Berlin Heidelberg, 2 edition, 2002, ►.

[109] H H Rose. Optics of high-performance electron microscopes. *Science and Technology of Advanced Materials*, 9(1):014107, 2008, ►.

[110] S. K. Chapman. *Maintaining and Monitoring the Transmission Electron Microscope*. Oxford University Press, 1986, ►.

[111] Louis de Broglie. The wave nature of the electron, 12 1929. Nobel Lecture.

[112] M. Baram and W.D Kaplan. Quantitative HRTEM analysis of FIB prepared specimens. *Journal of Microscopy*, 232(3):395–405, 2008. ISSN 1365-2818. doi: 10.1111/j.1365-2818.2008.02134.x, ►.

[113] Leonid A. Bendersky and Frank W. Gayle. Electron Diffraction Using Transmission Electron Microscopy. *Journal of Research of the National Institute of Standards and Technology*, 106(6):997–1012, 2001.

[114] Kamran Forghani, Mohammadreza Gharavipour, Martin Klein, Ferdinand Scholz, Oliver Klein, Ute Kaiser, Martin Feneberg, Benjamin Neuschl, and Klaus Thonke. In-situ deposited SiNx nanomask for crystal quality improvement in AlGaN. *physica status solidi (c)*, 8(7-8):2063–2065, 2011. ISSN 1610-1642. doi: 10.1002/pssc.201001074, ►.

[115] Helmut Foell. Defects in Crystals. Lectures. Technical report, University of Kiel, 2009, ►.

[116] M. Gandais, A. Hihi, C. Willaime, and Y. Efelboin. Dislocation contrast by transmission electron microscopy A method for Burgers vector characterization if the invisibility criterion is not valid. *Philosophical Magazine A*, 45(3):387–400, 1982. doi: 10.1080/01418618208236178, ►.

[117] Keshra Sangwal. *Etching of Crystals: Theory, Experiment and Application*. Elsevier Science Ltd, 1987, ►.

[118] B.C. Cai, A. Dasgupta, and Y.T. Chou. Etch pits on single crystals and bicrystals of niobium. *Journal of the Less Common Metals*, 90(1):37 – 47, 1983. ISSN 0022-5088. doi: 10.1016/0022-5088(83)90114-5, ►.

[119] J.L. Weyher, S. Lazar, L. Macht, Z. Liliental-Weber, R.J. Molnar, S. Müller, V.G.M. Sivel, G. Nowak, and I. Grzegory. Orthodox etching of HVPE-grown GaN. *Journal of Crystal Growth*, 305(2):384 – 392, 2007. ISSN 0022-0248. doi: 10.1016/j.jcrysgro.2007.03.030, ►.

[120] G Kamler, J.L Weyher, I Grzegory, E Jezierska, and T Wosinski. Defect-selective etching of GaN in a modified molten bases system. *Journal of Crystal Growth*, 246(1-2):21 – 24, 2002. ISSN 0022-0248. doi: 10.1016/S0022-0248(02)01786-4, ►.

[121] J.E. Ayers. The measurement of threading dislocation densities in semiconductor crystals by X-ray diffraction. *Journal of Crystal Growth*, 135 (1-2):71 – 77, 1994. ISSN 0022-0248. doi: 10.1016/0022-0248(94)90727-7, ►.

[122] Lyuji Ozawa. *Cathodoluminescence: theory and applications*. Kodansha, 1990, ►.

[123] Naoki Yamamoto. *Cathodoluminescence*. InTech, 2012, ►.

[124] M.R. Brozel, L. Breivik, D.J. Stirland, G.M. Williams, and A.G. Cullis. Dislocation density, infrared absorption and cathodoluminescence mapping of microstructure associated with dislocation cells in semi-insulating LEC GaAs. *Applied Surface Science*, 50(1-4):475 – 479, 1991. ISSN 0169-4332. doi: 10.1016/0169-4332(91)90221-5, ►.

[125] E. Meissner, S. Schweigard, J. Friedrich, T. Paskova, K. Udwary, G. Leibiger, and F. Habel. Cathodoluminescence imaging for the determination of dislocation density in differently doped HVPE GaN. *Journal of Crystal Growth*, 340(1):78 – 82, 2012. ISSN 0022-0248. doi: 10.1016/j.jcrysgro.2011.12.043, ►.

[126] B. G. Yacobi D. B. Holt. *Extended Defects in Semiconductors: Electronic Properties, Device Effects and Structures* . Cambridge University Press, 2007, ►.

[127] Hai Lu, X.A. Cao, S.F. LeBoeuf, H.C. Hong, E.B. Kaminsky, and S.D. Arthur. Cathodoluminescence mapping and selective etching of defects in bulk GaN. *Journal of Crystal Growth*, 291(1):82 – 85, 2006. ISSN 0022-0248. doi: 10.1016/j.jcrysgro.2006.02.026, ►.

[128] S Dassonneville, A Amokrane, B Sieber, J.-L Farvacque, B Beaumont, V Bousquet, P Gibart, K Leifer, and J.-D Ganiere. Cathodoluminescence intensity and dislocation contrast evolutions under electron beam excitation in epitaxial GaN laterally overgrown on (0001) sapphire. *Physica B: Condensed Matter*, 273-274(0):148 – 151, 1999. ISSN 0921-4526. doi: 10.1016/S0921-4526(99)00434-2, ►.

[129] T. Paskova, E.M. Goldys, and B. Monemar. Hydride vapour-phase epitaxy growth and cathodoluminescence characterisation of thick GaN films. *Journal of Crystal Growth*, 203(1-2):1 – 11, 1999. ISSN 0022-0248. doi: 10.1016/S0022-0248(99)00088-3, ►.

[130] Amelinckx S. and Dekeyser W. The structure and properties of grain boundaries. *Solid State Physics*, 8:325 – 499, 1959.

[131] R. Chierchia, T. Böttcher, H. Heinke, S. Einfeldt, S. Figge, and D. Hommel. Microstructure of heteroepitaxial GaN revealed by x-ray diffraction. *Journal of Applied Physics*, 93(11):8918–8925, 2003. doi: 10.1063/1.1571217, ►.

[132] Th. de Keijser, E. J. Mittemeijer, and H. C. F. Rozendaal. The determination of crystallite-size and lattice-strain parameters in conjunction with the profile-refinement method for the determination of crystal structures. *Journal of Applied Crystallography*, 16(3):309–316, Jun 1983. doi: 10.1107/S0021889883010493, ►.

[133] Ozturk M., Yu Hongbo, B. Sarikavak, S. Korcak, S. Ozcelik, and E. Ozbay. Structural analysis of an InGaN/GaN based light emitting diode by X-ray diffraction. *Journal of Materials Science: Materials in Electronics*, 21:185–191, 2010. ISSN 0957-4522, ►. 10.1007/s10854-009-9891-6.

[134] P.B. Hirsch P. Gay and A. Kelly. The estimation of dislocation densities in metals from X-ray data. *Acta Metallurgica*, 1(3):315 – 319, 1953, ►.

[135] Syed B. Qadri and J. H. Dinan. X-ray determination of dislocation density in epitaxial ZnCdTe. *Applied Physics Letters*, 47(10):1066–1068, 1985. doi: 10.1063/1.96381, ►.

[136] Hall W.H. Williamson, G.K. X-ray line broadening from filed aluminium and wolfram. *Acta Metallurgica*, 1(1):22–31, 1953, ►. cited By (since 1996) 2020.

[137] R. Kyutt, V. Ratnikov, G. Mosina, and M. Shcheglov. Structural perfection of GaN epitaxial layers according to x-ray diffraction measurements. *Physics of the Solid State*, 41:25–31, 1999. ISSN 1063-7834, ►. 10.1134/1.1130722.

[138] V. Ratnikov, R. Kyutt, T. Shubina, T. Paskova, E. Valcheva, and B. Monemar. Bragg and Laue x-ray diffraction study of dislocations in thick hydride vapor phase epitaxy GaN films. *Journal of Applied Physics*, 88(11):6252–6259, 2000. doi: 10.1063/1.1321021, ►.

[139] C.G Dunn and E.F Koch. Comparison of dislocation densities of primary and secondary recrystallization grains of Si-Fe. *Acta Metallurgica*, 5(10): 548 – 554, 1957. ISSN 0001-6160. doi: 10.1016/0001-6160(57)90122-0, ►.

[140] M. A. Krivoglaz and K. P. Ryboshapka. Theory of x-ray scattering by crystals containing dislocations. Case of random distribution of screw and edge dislocations in the crystal. *Fizika Metallov i Metallovedenie*, 15(18), 1963.

[141] V. Holý, T. Baumbach, D. Lubbert, L. Helfen, M. Ellyan, P. Mikulík, S. Keller, S. P. DenBaars, and J. Speck. Diffuse x-ray scattering from statistically inhomogeneous distributions of threading dislocations beyond the ergodic hypothesis. *Phys. Rev. B*, 77:094102, Mar 2008. doi: 10.1103/PhysRevB.77.094102, ►.

[142] Vladimir M. Kaganer and Karl K. Sabelfeld. X-ray diffraction peaks from correlated dislocations: Monte Carlo study of dislocation screening. *Acta Crystallographica Section A*, 66(6):703–716, Nov 2010. doi: 10.1107/S0108767310033544, ►.

[143] B. E. Warren. *X-Ray Diffraction*. Dover Pubn Inc, 1991, ►.

[144] M.A. Moram, C.F. Johnston, M.J. Kappers, and C.J. Humphreys. Investigating stacking faults in nonpolar gallium nitride films using x-ray diffraction. *Physica B: Condensed Matter*, 404(16):2189 – 2191, 2009. ISSN 0921-4526. doi: 10.1016/j.physb.2009.04.010, ►.

[145] M. A. Moram, C. F. Johnston, J. L. Hollander, M. J. Kappers, and C. J. Humphreys. Understanding x-ray diffraction of nonpolar gallium nitride films. *Journal of Applied Physics*, 105(11):113501, 2009. doi: 10.1063/1.3129307, ►.

[146] Melvin B McLaurin, Asako Hirai, Erin Young, Feng Wu, and James S Speck. Communication Basal Plane Stacking-Fault Related Anisotropy in X-ray Rocking Curve Widths of m-Plane GaN. *Japanese Journal of Applied Physics*, 47(7):5429–5431, 2008, ►.

[147] Qing S. Paduano, David W. Weyburne, and Alvin J. Drehman. An X-ray diffraction technique for analyzing basal-plane stacking faults in GaN. *physica status solidi (a)*, 207(11):2446–2455, 2010. ISSN 1862-6319. doi: 10.1002/pssa.201026258, ►.

[148] M. Barchuk, V. Holy, B. Miljevic, B. Krause, T. Baumbach, J. Hertkorn, and F. Scholz. X-ray diffuse scattering from threading dislocations in epitaxial GaN layers. *Journal of Applied Physics*, 108(4):043521, 2010. doi: 10.1063/1.3460803, ►.

[149] *X'Pert PRO User's Guide*, 2002.

[150] M. Barchuk, V. Holý, B. Miljević, B. Krause, and T. Baumbach. Grazing-incidence x-ray diffraction from GaN epitaxial layers with threading dislocations. *Applied Physics Letters*, 98(2):021912, 2011. doi: 10.1063/1.3543842, ►.

[151] Glenn F. Knoll. *Radiation Detection and Measurement* . John Wiley & Sons, 2000, ►.

[152] Bojan Miljevic. *Characterization of Growth and Real Structure of Nitride Based Semiconductor Devices by Use of Synchrotron Radiation*. PhD thesis, Karlsruher Instituts fuer Technologie, 2012.

[153] S. Lazarev, S. Bauer, K. Forghani, M. Barchuk, F. Scholz, and T. Baumbach. High resolution synchrotron X-ray studies of phase separation phenomena and the scaling law for the threading dislocation densities reduction in high quality AlGaN heterostructure. *Journal of Crystal Growth*, 2012. ISSN 0022-0248. doi: 10.1016/j.jcrysgro.2012.07.033, ►.

[154] S. Daniš, V. Holý, Z. Zhong, G. Bauer, and O. Ambacher. High-resolution diffuse x-ray scattering from threading dislocations in heteroepitaxial layers. *Applied Physics Letters*, 85(15):3065–3067, 2004. doi: 10.1063/1.1806279, ►.

[155] Friso van der Veen and Franz Pfeiffer. Coherent x-ray scattering. *Journal of Physics: Condensed Matter*, 16(28):5003, 2004, ►.

[156] M. Twigg, Y. Picard, J. Caldwell, C. Eddy, M. Mastro, R. Holm, P. Neudeck, A. Trunek, and J. Powell. Diffraction Contrast of Threading Dislocations in GaN and 4H-SiC Epitaxial Layers Using Electron Channeling Contrast Imaging. *Journal of Electronic Materials*, 39:743–746, 2010. ISSN 0361-5235, ►. 10.1007/s11664-010-1143-2.

[157] S. K. Sinha, E. B. Sirota, S. Garoff, and H. B. Stanley. X-ray and neutron scattering from rough surfaces. *Phys. Rev. B*, 38:2297–2311, Aug 1988. doi: 10.1103/PhysRevB.38.2297, ►.

[158] S.K. Sinha. Complementarity of neutrons and x-rays as probes of surfaces and interfaces. *Physica B: Condensed Matter*, 174(1-4):499 – 505, 1991. ISSN 0921-4526. doi: 10.1016/0921-4526(91)90648-X, ►.

[159] S. Lazarev, M. Barchuk, S. Bauer, K. Forghani, V. Holý, F. Scholz, and T. Baumbach. Study of threading dislocation density reduction in AlGaN epilayers by Monte Carlo simulation of high resolution reciprocal space maps of a two layer system. *Advanced Functional Materials*, 2012. submitted.

[160] Z Dridi, B Bouhafs, and P Ruterana. First-principles investigation of lattice constants and bowing parameters in wurtzite AlGaN, InGaN and InAlN alloys. *Semiconductor Science and Technology*, 18(9):850, 2003. doi: 10.1088/0268-1242/18/9/307, ►.

[161] C. Barry Carter David Bernard Williams. *Transmission electron microscopy*. Springer, 1996, ►.

[162] M. M. Hall, Jnr, V. G. Veeraraghavan, H. Rubin, and P. G. Winchell. The approximation of symmetric X-ray peaks by Pearson type VII distributions. *Journal of Applied Crystallography*, 10(1):66–68, Feb 1977. doi: 10.1107/S0021889877012849, ►.

[163] Daniel T. Gillespie. *Markov Processes: An Introduction for Physical Scientists*. Academic Press, San Diego, 1992, ►.

[164] Albert N. Shiryaev. *Probability*. Springer, 1996, ►.

[165] V. Srikant, J. S. Speck, and D. R. Clarke. Mosaic structure in epitaxial thin films having large lattice mismatch. *Journal of Applied Physics*, 82(9):4286–4295, 1997. doi: 10.1063/1.366235, ►.

[166] S.K. Mathis, A.E. Romanov, L.F. Chen, G.E. Beltz, W. Pompe, and J.S. Speck. Modeling of Threading Dislocation Reduction in Growing

GaN Layers. *physica status solidi (a)*, 179(1):125–145, 2000. ISSN 1521-396X. doi: 10.1002/1521-396X(200005)179:1<125::AID-PSSA125>3.0.CO;2-2, ►.

[167] A. E. Romanov, W. Pompe, G. E. Beltz, and J. S. Speck. An approach to threading dislocation reaction kinetics'. *Applied Physics Letters*, 69(22): 3342–3344, 1996. doi: 10.1063/1.117300, ►.

[168] R. Liu, A. Bell, F. A. Ponce, C. Q. Chen, J. W. Yang, and M. A. Khan. Luminescence from stacking faults in gallium nitride. *Applied Physics Letters*, 86(2):021908, 2005. doi: 10.1063/1.1852085, ►.

List of scientific outputs

Articles

1. Barchuk, M., Holý, V., Miljević, B., Krause, B., Baumbach, T., Hertkorn, J., and Scholz, F. X-ray diffuse scattering from threading dislocations in epitaxial GaN layers. *Journal of Applied Physics*, **108(4)**, 034521 (2010).

2. Barchuk, M., Holý, V., Miljević, B., Krause, B., and Baumbach, T. Grazing-incidence x-ray diffraction from GaN epitaxial layers with threading dislocations. *Applied Physics Letters*, **98**, 021912 (2011).

3. Barchuk, M., Holý, V., Kriegner, D.,Strangl, J., Schwaiger, S., and Scholz F. Diffuse x-ray scattering from stacking faults in a-plane GaN epitaxial layers. *Physical Review B*, **84**, 094113 (2011).

4. Lazarev, S., Bauer, S., Forghani, K., Barchuk, M., Scholz, F., and Baumbach, T. High resolution synchrotron X-ray studies of phase separation phenomena and the scaling law for the threading dislocation densities reduction in high quality AlGaN heterostructure. *Journal of Crystal Growth*, (2012), published online.

5. Lazarev, S., Barchuk, M., Bauer, S., Forghani, K., Holý, V., Scholz, F., and Baumbach, T. Study of threading dislocation density reduction in AlGaN epilayers by Monte Carlo simulation of high resolution reciprocal space maps of a two layer system. *Advanced Functional Materials*, (2012), submitted.

Conference participations with posters

1. International conference X-TOP 2008,
   Diffuse x-ray scattering from dislocations in relaxed semiconductor epitaxial layers - a Monte Carlo simulation.
   Linz, Austria, September 2008.

2. EW-MOVPE XIII Conference,
   Influence of the in-situ deposited SiN_X interlayer on the crystalline quality of MOVPE grown thin GaN layers.
   Ulm, Germany, September 2009.

3. International conference X-TOP 2010,
   Monte Carlo simulation of diffuse scattering from threading dislocations in epitaxial GaN layers in GID geometry.
   Coventry, Great Britain, September 2010.

4. International Union of Crystallography XXII Congress and General Assembly,
   Determination of the defects in the a-plane GaN heteroepitaxial layers.
   Madrid, Spain, August 2011.

5. 8th Autumn School on X-ray Scattering from Surfaces and Thin Layers,
   Determination of the defects in a-plane GaN and c-plane AlGaN heteroepitaxial layers.
   Smolenice, Slovakia, October 2011.

6. ANKA Users Meetings, Karlsruhe, Germany, 2008-2011.

Conference participations with oral talks

1. Week of Doctoral Study,
   Diffuse x-ray scattering from dislocations in relaxed semiconductor epitaxial layers - a Monte Carlo simulation.
   Charles University in Prague, Czech Republic, June 2008.

2. The VI Pinch Photonics School,
   X-ray scattering on GaN thin films, Monte Carlo simulation.
   Karlsruhe, Germany, May 2009.

3. Crystallographic Association Colloquiums, Czech Republic, 2008, 2009, 2011.

List of Tables

List of Acronyms

AFM atomic force microscopy
ANKA Angströmquelle Karlsruhe
BSF basal stacking fault
CCD charge-coupled device
CL cathodoluminescence
ELO epitaxial lateral overgrowth
EPD etch pit density
ESRF European Synchrotron Radiation Facility
fcc face-centered cubic
FWHM full width at half maximum
GID grazin-incidence diffraction
hcp hexagonal close packed
HRTEM high-resolution transmission electron microscopy
HVPE hydride vapour phase epitaxy
LDMOS laterally diffused metal oxide semiconductors
LED light emitting diodes
LPE liquid phase epitaxy
LR laser reflectometry
MBE molecular beam epitaxy
MD misfit dislocation
MOVPE metalorganic vapour phase epitaxy
NL nucleation layer
PSF prismatic stacking fault
RCI rocking-curve imaging
RHEED reflection high energy electron diffraction
rms root-mean-square
RSM reciprocal-space map
SCD single crystal diffractometer
SEM scanning electron microscopy
SF stacking fault
TEM transmission electron microscopy
TD threading dislocation
TMAl trimethyl-aluminium
TMGa trimethyl-gallium
UHV ultra high vacuum
XRR x-ray reflectivity
WBDF weak-beam dark field

A. Appendix

In this appendix, we present the program for simulation of the reciprocal-space maps of a two-dimensional random set of threading dislocations perpendicular to the surface in *coplanar* x-ray diffraction geometry. The computations are based on validity of far-field limit and kinematical theory of diffraction. The program is written in Fortran 90 programming language and it uses the International Mathematics and Statistics Library (ISML) provided by software developers. The comments referring the subsequent parts of code are emphasized as *italic* text.

```
Inclusion of the ISML
use numerical_libraries
Definition of variables
implicit complex*16 (c)
implicit real*8 (a,b)
implicit real*8 (d-h)
implicit real*8 (o-z)
character*20 aaa
parameter (nxdim=256)
parameter (nzdim=128)
dimension a(3,3),b(3,3),en(3),tau(3),xi(3),rho(10),bv(10,3),h(3),
& bvx(10),bvy(10),bvz(10),pp(10),ityp(10000),xd(10000),yd(10000)
dimension c(nxdim,nxdim,nzdim),vv(nxdim,nzdim),va(nxdim,nzdim)
Definition of π and i constants
pi=4*datan(1d0)
cj=(0.,1.)
Files with input and output data
open(14,file='input.dat')
open(11,file='output.dat')
write(*,*)'lattice parameters'
read(14,*)a1,a2,a3
write(*,*)'lattice angles in deg'
read(14,*)u1d,u2d,u3d
write(*,*)'wave length'
read(14,*)dlam
u1=u1d*pi/180.
u2=u2d*pi/180.
u3=u3d*pi/180.
Cartesian coordinates of the basis vectors of the direct lattice
pom=dsqrt(1.-dcos(u1)**2-dcos(u2)**2-dcos(u3)**2+
& 2.*dcos(u1)*dcos(u2)*dcos(u3))
a(1,1)=a1
a(1,2)=0.
a(1,3)=0.
a(2,1)=a2*dcos(u3)
a(2,2)=a2*dsin(u3)
a(2,3)=0.
```

```
a(3,1)=a3*dcos(u2)
a(3,2)=a3*(dcos(u1)-dcos(u2)*dcos(u3))/dsin(u3)
a(3,3)=a3*pom/dsin(u3)
Cartesian coordinates of the basis vectors of the reciprocal lattice
b(1,1)=2.*pi/a1
b(1,2)=-2.*pi*dcos(u3)/a1/dsin(u3)
b(1,3)=-2.*pi*(-dcos(u3)*dcos(u1)+dcos(u2))/dsin(u3)/a1/pom
b(2,1)=0.
b(2,2)=2.*pi/dsin(u3)/a2
b(2,3)=-2.*pi*(dcos(u1)-dcos(u2)*dcos(u3))/dsin(u3)/a2/pom
b(3,1)=0.
b(3,2)=0.
b(3,3)=2.*pi*dsin(u3)/a3/pom
write(*,*)'hkl of the surface'
read(14,*)en1,en2,en3
write(*,*)'hkl of the x-axis'
read(14,*)tau1,tau2,tau3
Cartesian coordinates of the surface normal and of the x-axis
enn=0.
tauu=0.
do j=1,3
en(j)=en1*a(1,j)+en2*a(2,j)+en3*a(3,j)
tau(j)=tau1*a(1,j)+tau2*a(2,j)+tau3*a(3,j)
enn=enn+en(j)**2
tauu=tauu+tau(j)**2
enddo
do j=1,3
en(j)=en(j)/dsqrt(enn)
tau(j)=tau(j)/dsqrt(tauu)
enddo
Cartesian coordinates of the y-axis
xi(1)=en(2)*tau(3)-en(3)*tau(2)
xi(2)=en(3)*tau(1)-en(1)*tau(3)
xi(3)=en(1)*tau(2)-en(2)*tau(1)
xii=xi(1)**2+xi(2)**2+xi(3)**2
do j=1,3
xi(j)=xi(j)/dsqrt(xii)
enddo
write(*,*)'number of dislocation types'
read(14,*)nb
do jb=1,nb
write(*,*)'the burgers vector'
read(14,*)bv1,bv2,bv3
write(*,*)'dislocation type',jb,'density'
read(14,*)rho(jb)
Cartesian coordinates of the Burgers vector
do j=1,3
bv(jb,j)=bv1*a(1,j)+bv2*a(2,j)+bv3*a(3,j)
```

```
enddo
Laboratory coordinates of the Burgers vector
bvx(jb)=bv(jb,1)*tau(1)+bv(jb,2)*tau(2)+bv(jb,3)*tau(3)
bvy(jb)=bv(jb,1)*xi(1)+bv(jb,2)*xi(2)+bv(jb,3)*xi(3)
bvz(jb)=bv(jb,1)*en(1)+bv(jb,2)*en(2)+bv(jb,3)*en(3)
write(*,*)'b:',jb,bvx(jb),bvy(jb),bvz(jb)
enddo
write(*,*)'the Poisson ratio'
read(14,*)poiss
write(*,*)'hkl of the diffraction vector'
read(14,*)h1,h2,h3
Cartesian coordinates of the diffraction vector
do j=1,3
h(j)=h1*b(1,j)+h2*b(2,j)+h3*b(3,j)
enddo
Laboratory coordinates of the diffraction vector
hx=h(1)*tau(1)+h(2)*tau(2)+h(3)*tau(3)
hy=h(1)*xi(1)+h(2)*xi(2)+h(3)*xi(3)
hz=h(1)*en(1)+h(2)*en(2)+h(3)*en(3)
write(*,*)'h:',hx,hy,hz
write(*,*)'step of qx'
read(14,*)dqx
write(*,*)'binary exponent of the step number along x'
read(14,*)mx
nx=2**mx
write(*,*)'step of qz'
read(14,*)dqz
write(*,*)'binary exponent of the step number along z'
read(14,*)mz
nz=2**mz
write(*,*)'step of qx and qz',dqx,dqz
The sampling theorem
dx=2.*pi/dqx/float(nx)
xmin=-float(nx-1)/float(nx)*pi/dqx
qxmin=-float(nx-1)/2.*dqx
dz=2*pi/dqz/float(nz)
zmin=-float(nz-1)/float(nz)*2.*pi/dqz
qzmin=-float(nz-1)/2.*dqz
write(*,*)'number of patches (averaging), expansion factor'
read(14,*)np,ef
write(*,*)'to subtract the CTR? [0..No,1..Yes]'
read(14,*)jsub
write(*,*)'x-dispersion of the resolution function'
read(14,*)gx
write(*,*)'z-dispersion of the resolution function'
read(14,*)gz
Size of the patch
eL=-2*xmin*ef
```

```
*Number of the dislocations in one patch*
nd=0
pps=0
do jb=1,nb
nd=nd+int(eL**2*rho(jb))
pps=pps+rho(jb)
enddo
pp(1)=rho(1)/pps
do jb=2,nb
pp(jb)=pp(jb-1)+rho(jb)/pps
enddo
do jz=1,nz
do jx=1,nx
vv(jx,jz)=0
enddo
enddo
write(*,*)'xmin=',xmin,' zmin=',zmin
write(*,*)'qxmin=',qxmin,' qzmin=',qzmin
write(*,*)'size of the patch=',eL
write(*,*)'total number of dislocations in one patch=',nd
*The loop over the patches*
do jp=1,np
write(*,*)'patch no=',jp
*Generation of the dislocation positions*
call drnun(nd,xd)
call drnun(nd,yd)
do jd=1,nd
ityp(jd)=0
call drnun(1,rtyp)
if(rtyp.le.pp(1))then
ityp(jd)=1
else
do jb=2,nb
if(rtyp.gt.pp(jb-1).and.rtyp.le.pp(jb))then
ityp(jd)=jb
endif
enddo
endif
if(ityp(jd).eq.0)ityp(jd)=nb
xd(jd)=(xd(jd)-1./2.)*eL
yd(jd)=(yd(jd)-1./2.)*eL
enddo
*Generation of the displacement field*
do jz=1,nz
if(mod(jz,10).eq.0)then
write(*,*)'generating the displacement field',jz,nz
endif
z=zmin+(jz-1)*dz
```

```
do jy=1,nx
y=xmin+(jy-1)*dx
do jx=1,nx
x=xmin+(jx-1)*dx
hu=0.
do jd=1,nd
call displac(x-xd(jd),y-yd(jd),z,bvx(ityp(jd)),
& bvy(ityp(jd)),bvz(ityp(jd)),poiss,ux,uy,uz)
hu=hu+hx*ux+hy*uy+hz*uz
enddo
if(jsub.eq.0)then
cpom=cdexp(-cj*hu)
else
cpom=cdexp(-cj*hu)-1.
endif
c(jx,jy,jz)=cpom*cdexp(cj*pi*(nx-1)/float(nx)*
& (jx-1))*cdexp(cj*pi*(nx-1)/float(nx)*(jy-1))*
& cdexp(cj*pi*(nz-1)/float(nz)*(jz-1))
enddo
enddo
enddo
```

Three-dimensional fast Fourier transform

```
call dfft3f(nx,nx,nz,c,nxdim,nxdim,c,nxdim,nxdim)
do jqz=1,nz
do jqx=1,nx
dinty=0
do jqy=1, nx
dinty=dinty+cdabs(c(jqx,jqy,jqz))**2
enddo
vv(jqx,jqz)=vv(jqx,jqz)+dinty
enddo
enddo
enddo
```

Convolution with the resolution function

```
thet=dasin(dlam/2*dsqrt(4/3*(h1**2+h2**2+h1*h2)/a1**2+h3**2/a3**2))
delt=datan(hz/hx)
theta=thet-delt
ya=dcos(theta)**2/2/gx**2+dsin(theta)**2/2/gz**2
yb=-dsin(2*theta)/4/gx**2+dsin(2*theta)/4/gz**2
yc=dsin(theta)**2/2/gx**2+dcos(theta)**2/2/gz**2
do jz=1,nz
qz=qzmin+(jz-1)*dqz
do jx=1, nx
qx=qxmin+(jx-1)*dqx
va(jx,jz)=0
do jzc=1,nz
qcz=qzmin+(jzc-1)*dqz
do jxc=1,nx
```

```
qcx=qxmin+(jxc-1)*dqx
va(jx,jz)=va(jx,jz)+vv(jxc,jzc)*
& dexp(-((qx-qcx)**2*ya+(qz-qcz)**2*yc+2*yb*(qz-qcz)*(qx-qcx)))
enddo
enddo
enddo
enddo
```

Saving of the calculated result

```
do jqz=1,nz
qz=qzmin+(jqz-1)*dqz
do jqx=1,nx
qx=qxmin+(jqx-1)*dqx
write(11,100)qx,qz,va(jqx,jqz)
enddo
enddo
100 format(3(1x,e12.6))
stop
end
```

The subroutine for displacement field calculation

```
subroutine displac(xx,yy,z,bx,by,bz,nu,ux,uy,uz)
implicit real*8 (a-h)
implicit real*8 (o-z)
real*8 nu
bs=bz
be=dsqrt(bx**2+by**2)
phi=datan2(by,bx)
x=xx*dsin(phi)-yy*dcos(phi)
y=xx*dcos(phi)+yy*dsin(phi)
```

The displacement field from a screw threading dislocation with the dislocation line perpendicular to the surface. The formulae are taken from [25] with the $\alpha \to 0$ *limit*

```
t1 = x**2
t2 = y**2
t3 = z**2
t5 = dsqrt(t1+t2+t3)
t7 = 1.D0/(-t5+z)
t9 = 1.D0/0.3141592653589793D1
t10 = bs*t9
t18 = datan2(y,x)
usx = -t10*t7*y/2.D0
usy = t7*x*t10/2.D0
usz = bs*t9*t18/2.D0
```

The displacement field from an edge threading dislocation with the dislocation line perpendicular to the surface. The Burgers vector of dislocation coincides with y-axis. The formulae are taken from [25] with the $\alpha \to 0$ *limit*

```
t1 = y**2
t3 = x**2
t4 = z**2
```

```
t6 = dsqrt(t3+t1+t4)
t7 = t6*z
t10 = nu**2
t11 = t6-z
t12 = dlog(t11)
t13 = t10*t12
t14 = t3*t4
t17 = t4*t1
t20 = t6+z
t21 = 1.D0/t11
t23 = dlog(t20*t21)
t24 = t23*nu
t29 = t3*t1
t32 = nu*t12
t40 = t23*z
t41 = t1*t6
t43 = t12*z
t44 = t3*t6
t47 = 6.D0*nu*t1*t7+4.D0*t13*t14+4.D0*t13*t17-2.D0*t24*t14-2.D0*t2
#4*t17+8.D0*t13*t29-12.D0*t32*t29-4.D0*t10*t1*t7-6.D0*t32*t17-t40*t
#41-2.D0*t43*t44
t55 = nu*t3
t68 = t1**2
t71 = t3**2
t76 = -2.D0*t43*t41-t40*t44-4.D0*t24*t29-6.D0*t32*t14-6.D0*t55*t4-
#2.D0*t55*t1+4.D0*t10*t3*t1+t23*t1*t4+4.D0*t10*t4*t3+4.D0*t13*t68+4
#.D0*t13*t71-6.D0*t32*t71
t80 = t23*t3
t84 = t3*z*t6
t89 = t12*t3
t100 = z*t1*t6
t107 = -6.D0*t32*t68+2.D0*t80*t1+2.D0*t84+2.D0*t12*t1*t4+4.D0*t89*
#t1+2.D0*t89*t4-2.D0*t24*t71-2.D0*t24*t68+t80*t4+6.D0*t32*t100+2.D0
#*t24*t100+2.D0*t24*t84
t127 = -4.D0*t13*t84-2.D0*t71-2.D0*t29+2.D0*t12*t71+t23*t71-2.D0*t
#14+t23*t68+2.D0*t12*t68-2.D0*nu*t71+6.D0*t32*t84-4.D0*t13*t100+4.D
#0*t10*t71
t131 = 1.D0/t6
t133 = 1.D0/t20
t134 = t11**2
t135 = 1.D0/t134
t137 = 1.D0/0.3141592653589793D1
t139 = 1.D0/(-1.D0+nu)
t140 = t137*t139
t144 = t10*x
t145 = y*t4
t148 = nu*x
t153 = datan2(y,x)
```

```
t160 = t153*nu
t163 = t3*t153
t175 = t3*x
t178 = t1*y
t182 = -2.D0*t144*t145+3.D0*t148*t145+2.D0*t153*z*t41-x*t6*y*z+2.D
#0*t160*t17+2.D0*t163*nu*t4+2.D0*t163*t7+4.D0*t160*t29+2.D0*t160*t6
#8-2.D0*t163*t4+nu*t175*y-2.D0*t144*t178+t148*t178
t200 = t6*y*z
t213 = -2.D0*t10*t175*y-4.D0*t163*t1+2.D0*t160*t71+y*x*t4-2.D0*t15
#3*t1*t4-2.D0*t163*nu*z*t6-2.D0*t144*t200+x*t178+t175*y-2.D0*t160*t
#100+3.D0*t148*t200-2.D0*t153*t68-2.D0*t153*t71
uex = -be*(t47+t76+t107+t127)*t131*t133*t135*t140/8.D0
uey = (t182+t213)*be*t139*t137*t135*t131*t133/4.D0
uez = -(-2.D0*t6+2.D0*nu*t6+z)*x*be*nu*t140*t131*t21/2.D0
The total displacement field in the laboratory system
ux=(usx+uex)*dsin(phi)+(usy+uey)*dcos(phi)
uy=-(usx+uex)*dcos(phi)+(usy+uey)*dsin(phi)
uz=usz+uez
return
end
```

B. Appendix

Here, we present the the modified program for simulation of the RSMs of a two-dimensional random set of threading dislocations perpendicular to the surface in *grazing-incidence* diffraction. The computations are based on validity of far-field limit and kinematical theory of diffraction. The plane of the RSM is ($q_x q_y$) and the diffraction vector is parallel to q)x axis. The program is written in Fortran 90 programming language and it uses the International Mathematics and Statistics Library (ISML) provided by software developers. The comments referring the subsequent parts of code are emphasized as *italic* text.

```
Inclusion of the ISML
use numerical_libraries
Definition of variables
implicit complex*16 (c)
implicit real*8 (a,b)
implicit real*8 (d-h)
implicit real*8 (o-z)
character*20 aaa
parameter (nxdim=256)
parameter (nzdim=128)
parameter (ntyp=10)
parameter (ndisl=10000)
dimension a(3,3),b(3,3),h(3),en(3),ex(3),ey(3),ez(3),bv(ntyp,3),
& bvx(ntyp),bvy(ntyp),bvz(ntyp),rho(ntyp),pp(ntyp),vv(nxdim,nxdim),
& ityp(ndisl),xd(ndisl),yd(ndisl),cv(nzdim),c(nxdim,nxdim)
Definition of π and i constants
pi=4*datan(1d0)
cj=(0.,1.)
Files with input and output data
open(14,file='input.dat')
open(11,file='output.dat')
write(*,*)'lattice parameters'
read(14,*)a1,a2,a3
write(*,*)'lattice angles in deg'
read(14,*)u1d,u2d,u3d
u1=u1d*pi/180.
u2=u2d*pi/180.
u3=u3d*pi/180.
Cartesian coordinates of the basis vectors of the direct lattice
pom=dsqrt(1.-dcos(u1)**2-dcos(u2)**2-dcos(u3)**2+
& 2.*dcos(u1)*dcos(u2)*dcos(u3))
a(1,1)=a1
a(1,2)=0.
a(1,3)=0.
a(2,1)=a2*dcos(u3)
a(2,2)=a2*dsin(u3)
```

```
a(2,3)=0.
a(3,1)=a3*dcos(u2)
a(3,2)=a3*(dcos(u1)-dcos(u2)*dcos(u3))/dsin(u3)
a(3,3)=a3*pom/dsin(u3)
```
Cartesian coordinates of the basis vectors of the reciprocal lattice
```
b(1,1)=2.*pi/a1
b(1,2)=-2.*pi*dcos(u3)/a1/dsin(u3)
b(1,3)=-2.*pi*(-dcos(u3)*dcos(u1)+dcos(u2))/dsin(u3)/a1/pom
b(2,1)=0.
b(2,2)=2.*pi/dsin(u3)/a2
b(2,3)=-2.*pi*(dcos(u1)-dcos(u2)*dcos(u3))/dsin(u3)/a2/pom
b(3,1)=0.
b(3,2)=0.
b(3,3)=2.*pi*dsin(u3)/a3/pom
write(*,*)'hkl of the surface'
read(14,*)en1,en2,en3
write(*,*)'diffraction indexes'
read(14,*)h1,h2,h3
```
Cartesian coordinates of the diffraction vector and the reciprocal normal vector
```
hh=0
enn=0
do j=1,3
h(j)=b(1,j)*h1+b(2,j)*h2+b(3,j)*h3
hh=hh+h(j)**2
en(j)=b(1,j)*en1+b(2,j)*en2+b(3,j)*en3
enn=enn+en(j)**2
enddo
```
Cartesian coordinates of the q_x and q_z axes
```
test=0
do j=1,3
ex(j)=h(j)/dsqrt(hh)
ez(j)=en(j)/enn
test=test+ex(j)*ez(j)
enddo
if(dabs(test).gt.1e-6)then
write(*,*)'vector h is not horizontal!!'
pause
endif
```
Cartesian coordinates of the q_y axis
```
ey(1)=ez(2)*ex(3)-ez(3)*ex(2)
ey(2)=ez(3)*ex(1)-ez(1)*ex(3)
ey(3)=ez(1)*ex(2)-ez(2)*ex(1)
write(*,*)'number of dislocation types'
read(14,*)nb
if(nb.gt.ntyp)then
write(*,*)'the number of dislocation types is too large!!'
stop
endif
```

```
do jb=1,nb
write(*,*)'the Burgers vector'
read(14,*)bv1,bv2,bv3
write(*,*)'dislocation type',jb,'density'
read(14,*)rho(jb)
Cartesian coordinates of the Burgers vector
do j=1,3
bv(jb,j)=bv1*a(1,j)+bv2*a(2,j)+bv3*a(3,j)
enddo
Laboratory coordinates of the Burgers vector
bvx(jb)=bv(jb,1)*tau(1)+bv(jb,2)*tau(2)+bv(jb,3)*tau(3)
bvy(jb)=bv(jb,1)*xi(1)+bv(jb,2)*xi(2)+bv(jb,3)*xi(3)
bvz(jb)=bv(jb,1)*en(1)+bv(jb,2)*en(2)+bv(jb,3)*en(3)
write(*,*)'b:',jb,bvx(jb),bvy(jb),bvz(jb)
enddo
write(*,*)'the Poisson ratio'
read(14,*)poiss
write(*,*)'layer thickness'
read(14,*)T
write(*,*)'step of qx'
read(14,*)dqx
write(*,*)'binary exponent of the step number along x'
read(14,*)mx
nx=2**mx
if(nx.ge.nxdim)then
write(*,*)'the number of steps along x,y is too large!!'
stop
endif
The sampling theorem
dx=2.*pi/dqx/float(nx)
xmin=-float(nx-1)/float(nx)*pi/dqx
qxmin=-float(nx-1)/2.*dqx
write(*,*)'angle of incidence, angle of exit in deg'
read(14,*)ajd,afd
aj=ajd*pi/180.
af=afd*pi/180.
write(*,*)'photon energy in eV'
read(14,*)ener
amda=12398.42/ener
ak=2*pi/amda
write(*,*)'1-n of the layer'
read(14,*)cd
aki=-ak*dsin(aj)
akf=ak*dsin(af)
cki=-ak*cdsqrt(dsin(aj)**2-2*cd)
ckf=ak*cdsqrt(dsin(af)**2-2*cd)
cqz=ckf-cki
titf=cdabs(2*aki/(aki+cki)*2*akf/(akf+ckf))**2
```

```
write(*,*)'number of patches (averaging), expansion factor'
read(14,*)np,ef
write(*,*)'to subtract the CTR? [0..No,1..Yes]'
read(14,*)jsub
write(*,*)'eps, step, number of steps along z'
read(*,*)eps,nz,nmax
if(nz.ge.nzdim)then
write(*,*)'the number of steps along z is too large!!'
stop
endif
dz=T/float(nz-1)
write(*,*)'x-ray coherence width'
read(14,*)sirka
Size of the patch
eL=-2*xmin*ef
Number of the dislocations in one patch
nd=0
pps=0
do jb=1,nb
nd=nd+int(eL**2*rho(jb))
pps=pps+rho(jb)
enddo
pp(1)=rho(1)/pps
do jb=2,nb
pp(jb)=pp(jb-1)+rho(jb)/pps
enddo
do jy=1,nx
do jx=1,nx
vv(jx,jy)=0
enddo
enddo
write(*,*)'xmin=',xmin,' qxmin=',qxmin write(*,*)'size of the patch=',eL
write(*,*)'total number of dislocations in one patch=',nd
if(nd.gt.ndisl)then
write(*,*)'the total number of dislocations is too large!!'
stop
endif
The loop over the patches
do jp=1,np
write(*,*)'patch no=',jp
Generation of the dislocation positions
call drnun(nd,xd)
call drnun(nd,yd)
do jd=1,nd
ityp(jd)=0
call drnun(1,rtyp)
if(rtyp.le.pp(1))then
ityp(jd)=1
```

```
      else
      do jb=2,nb
      if(rtyp.gt.pp(jb-1).and.rtyp.le.pp(jb))then
      ityp(jd)=jb
      endif
      enddo
      endif
      if(ityp(jd).eq.0)ityp(jd)=nb
      xd(jd)=(xd(jd)-1./2.)*eL
      yd(jd)=(yd(jd)-1./2.)*eL
      enddo
      Generation of the displacement field
      do jx=1,nx
      x=xmin+(jx-1)*dx
      do jy=1,nx
      y=xmin+(jy-1)*dx
      do jz=1,nz
      z=-T+(jz-1)*dz
      hu=0.
      do jd=1,nd
      call displac(x-xd(jd),y-yd(jd),z,bvx(ityp(jd)),
     & bvy(ityp(jd)),bvz(ityp(jd)),poiss,ux,uy,uz)
      hu=hu+ux*dsqrt(hh)
      enddo
      if(jsub.eq.0)then
      cv(jz)=cdexp(-cj*hu)*dexp(-dabs(dimag(cqz)*z))
      else
      cv(jz)=(cdexp(-cj*hu)-1.)*dexp(-dabs(dimag(cqz)*z))
      endif
      enddo
      Calculation of the scattered wave amplitude along q_z with Filon's method. The
subroutine computes the integral \int_a^b cf(x)\exp^{itx}dx.
      call efilonm(-T,0d0,-dreal(cqz),cv,-T,0d0,dz,nz,nzdim,eps,nmax,cvv,err,nskut)
      c(jx,jy)=cvv**cdexp(cj*pi*((nx-1)/float(nx)*(jx-1)+
     & (nx-1)/float(nx)*(jy-1)))*dx**2*
     & dexp(-(x**2+y**2)/2/sirka**2)
      enddo
      enddo
      Two-dimensional fast Fourier transform
      call dfft2d(nx,nx,c,nxdim,c,nxdim)
      do jqy=1,nx
      do jqx=1,nx
      vv(jqx,jqy)=vv(jqx,jqy)+cdabs(c(jqx,jqy))**2
      enddo
      enddo
      enddo
      Saving of the calculated result
      do jqy=1,nx
```

```
qy=qxmin+(jqy-1)*dqx
do jqx=1,nx
qx=qxmin+(jqx-1)*dqx
write(11,100)qx,qy,vv(jqx,jqy)/float(np)*titf
enddo
enddo
100 format(3(1x,e12.6))
stop
end
```

The subroutine with Filon's method of integration

```
subroutine efilonm(a,b,t,cf,zmin,zmax,dz,nz,ndim,eps,nmax,cv,err,n)
implicit complex*16 (c)
implicit real*8 (a,b)
implicit real*8 (d-h)
implicit real*8 (o-z)
dimension cff(nmax),cffs(nmax),cf(ndim)
cj=(0.,1.)
n=1
1 continue
if(n.gt.nmax/2)then
write(*,*)n,nmax
write(*,*)'the size of the arrays is not sufficient'
return
endif
h=(b-a)/float(2*n)
jz=int((a-zmin)/dz)+1
ddz=a-(zmin+(jz-1)*dz)
if(jz.le.1)ca=cf(1)
if(jz.ge.nz)ca=cf(nz)
if(jz.gt.1.and.jz.lt.nz)ca=cf(jz)+(cf(jz+1)-cf(jz))*ddz/dz
jz=int((b-zmin)/dz)+1
ddz=b-(zmin+(jz-1)*dz)
if(jz.le.1)cb=cf(1)
if(jz.ge.nz)cb=cf(nz)
if(jz.gt.1.and.jz.lt.nz)cb=cf(jz)+(cf(jz+1)-cf(jz))*ddz/dz
th=t*h
ce0=ca*cdexp(cj*t*a)-cb*cdexp(cj*t*b)
if(th.ne.0.)then
al=1./th+dsin(2.*th)/(2.*th**2)-2.*dsin(th)**2/th**3
be=2.*((1.+dcos(th)**2)/th**2-dsin(2.*th)/th**3)
ga=4.*(dsin(th)/th**3-dcos(th)/th**2)
else
al=0.
be=2./3.
ga=4./3.
endif
do j=1,2*n-1
if(n.eq.1.or.(n.gt.1.and.mod(j,2).eq.1))then
```

```
zz=a+j*h
jz=int((zz-zmin)/dz)+1
ddz=zz-(zmin+(jz-1)*dz)
if(jz.le.1)cff(j)=cf(1)
if(jz.ge.nz)cff(j)=cf(nz)
if(jz.gt.1.and.jz.lt.nz)cff(j)=cf(jz)+(cf(jz+1)-cf(jz))*ddz/dz
endif
if(n.gt.1.and.mod(j,2).eq.0)then
cff(j)=cffs(j/2)
endif
enddo
cff(2*n)=cb
ce1=ce0/2.
ce2=0.
do j=1,n
ce1=ce1+cff(2*j)*cdexp(cj*t*(a+2*j*h))
ce2=ce2+cff(2*j-1)*cdexp(cj*t*(a+(2*j-1)*h))
cffs(2*j-1)=cff(2*j-1)
cffs(2*j)=cff(2*j)
enddo
cv=h*(cj*al*ce0+be*ce1+ga*ce2)
if(n.lt.8)then
n=n*2
cvs=cv
goto 1
endif
if(cdabs(cvs).ne.0)then
err=cdabs((cv-cvs)/cvs)
else
err=1
endif
if(err.gt.eps)then
n=2*n
cvs=cv
goto 1
endif
return
end
```

The subroutine for displacement field calculation. The code used for in this subroutine see in Appendix A

```
subroutine displac(xx,yy,z,bx,by,bz,nu,ux,uy,uz)
...
```

C. Appendix

The program for diffraction profiles simulation from I_1 and I_2 SFs in a-plane GaN is written in MATLAB programming language. It enables to determine the density of SFs mentioned above. The program is called by the command w=aGaNSFv3(hkl4,q,Mave,sigma,eps,N,Np,L,shape). Here, such input parameters are used:

- hkl4 - diffraction vector in four-indexes notation;
- q - vector of the $\boldsymbol{q}$ values in the reciprocal space along [0001];
- Mave - mean distance between the fault planes;
- sigma - rms deviation of the fault distances (sigma=0 means geometric distribution);
- eps - relative change in the distance of the [0001] planes at the defect;
- N - number of the (0001) planes in the coherent patch;
- Np - number of coherent patches;
- L - coherence width in the monolayer thicknesses (L=0 means ideally coherent primary beam);
- shape - shape factor of the coherence function in direct space.

The output of the program is w structure with the following components:

- w.q - vector of the q values in the reciprocal space along [0001];
- w.int - vector of the intensities along [0001];
- w.M - vector with the positions of the fault planes in the first patch
- w.d - vector of the d-values in the first patch.

The comments referring subsequent parts of code are emphasized as *italic* text.

```
function w=aGaNSFv3(hkl4,q,Mave,sigma,eps,N,Np,L,shape)
Parameters of the Gamma distribution
if sigma>0;
em=(Mave/sigma)^2;
else
em=0;
end;
Position of the N atom in the molecule in the crystallographic system in three-indexes notation
dN=[0 0 3/8];
Lateral shift of the B plane from the A position in three-indexes notation
p=[2/3 1/3 0];
hkl indexes in the three-indexes notation
```

```
hkl(1)=hkl4(1);hkl(2)=hkl4(2);hkl(3)=hkl4(4);
GaN lattice parameters
a=3.187;c=5.186;
Thomson coefficients
fTGa=[15.235400 3.066900 6.700600 0.241200 4.35910 10.780500 2.962300 61.413500
1.718900];
fTN=[12.212600 0.005700 3.132200 9.893300 2.01250 28.997500 1.166300 0.582600
-11.529000];
Coordinates of the basis vectors of the direct lattice in the laboratory system
A=[a 0 0;-a/2 a*sqrt(3)/2 0;0 0 c];
Position of the N atom in the molecule in the laboratory system
DN=dN(1)*A(1,:)+dN(2)*A(2,:)+dN(3)*A(3,:);
Lateral shift of the B plane from the A position in the laboratory system
P=p(1)*A(1,:)+p(2)*A(2,:)+p(3)*A(3,:);
Coordinates of the basis vectors of the reciprocal lattice in the laboratory
system
B=2*pi*(inv(A))';
Coordinates of the scattering vector in the laboratory system
nq=length(q);Q=zeros(nq,3);
Q(:,1)=hkl(1)*B(1,1)+hkl(2)*B(2,1)+(hkl(3)+q)*B(3,1);
Q(:,2)=hkl(1)*B(1,2)+hkl(2)*B(2,2)+(hkl(3)+q)*B(3,2);
Q(:,3)=hkl(1)*B(1,3)+hkl(2)*B(2,3)+(hkl(3)+q)*B(3,3);
QQ=sqrt(Q(:,1).^2+Q(:,2).^2+Q(:,3).^2);
sthL2=QQ.^2/16/pi^2;
lambda=1.5405;K=2*pi/lambda;
Q0=hkl*B;
Theta=asin(norm(Q0)/2/K)*180/pi;
disp(['Theta=',num2str(Theta),'deg']);
Formfactors of Ga and N atoms (without dispersion correction)
fGa=fTGa(1)*exp(-sthL2*fTGa(2))+fTGa(3)*exp(-sthL2*fTGa(4))+
fTGa(5)*exp(-sthL2*fTGa(6))+fTGa(7)*exp(-sthL2*fTGa(8))+fTGa(9);
fN=fTN(1)*exp(-sthL2*fTN(2))+fTN(3)*exp(-sthL2*fTN(4))+
fTN(5)*exp(-sthL2*fTN(6))+fTN(7)*exp(-sthL2*fTN(8))+fTN(9);
Structure factor of a GaN molecule
phi=fGa+fN.*exp(-1i*(Q(:,1)*DN(1)+Q(:,2)*DN(2)+Q(:,3)*DN(3)));
kappa=exp(-1i*(Q(:,1)*P(1)+Q(:,2)*P(2)+Q(:,3)*P(3)));
ksi=exp(-1i*(Q(:,1)*A(3,1)+Q(:,2)*A(3,2)+Q(:,3)*A(3,3))/2);
ksieps=ksi.^eps;
Coherence function
if L>0;
sig=mujpearsonVII(linspace(-N/2,N/2,N),0,L,shape);
else
sig=ones(1,N);
end;
vysl=zeros(nq,1);
loop over the patches
for jp=1:Np;
disp(['patch no. ',num2str(jp),' from ',num2str(Np),' patches']);
```

Generation of the positions of the fault planes, geometric distribution of the distances

```
Ms=0;
k=1;
while Ms<N;
if em==0;
dist=randraw('geom',1/(1+Mave),1);
else
dist=randraw('gamma',[0 Mave/em em],1);
end;
if dist>2;
Ms=Ms+dist;
M(k)=Ms;
k=k+1;
end;
end;
nM=k-1;
if jp==1;
Mvys=M;
end;
```

Generation of the sequence of lateral positions, calculation of the amplitude

```
d=ones(1,N);
d(2)=0;
k=1;
ampl=kappa*sig(1)+ksi*sig(2);
disp(['calculating the amplitude, patch no. ',num2str(jp)]);
for j=3:N;
if k<=nM;
MM=M(k);
else
MM=N+1;
end
if j<MM;
d(j)=d(j-2);
else
d(j)=2*d(j-1)-d(j-2);
k=k+1;
end;
ampl=ampl+ksi.^(j-1).*ksieps.^(k-1).*kappa.^d(j)*sig(j);
end;
vysl=vysl+abs(phi.*ampl).^2;
if jp==1;
dvys=d;
end;
end;
w.q=q;w.M=Mvys;w.int=vysl/Np;w.d=dvys;
end
```